TECHNISCHE UNIVERSITÄT MÜNCHEN

Zentralinstitut für Medizintechnik (IMETUM)
und Klinikum rechts der Isar, Abteilung für Neuroradiologie

BOLD-based Magnetic Resonance Imaging of Hypoxia in the Human Brain

Adaptation of Measurement and Data Analysis Strategies for Clinical Requirements

Nuria Hildegard Maria Hirsch

Vollständiger Abdruck der von der Fakultät für Physik der Technischen Universität München zur Erlangung des akademischen Grades eines

Doktors der Naturwissenschaften (Dr. rer. nat.)

genehmigten Dissertation.

Vorsitzender:	Univ.-Prof. Dr. M. Zacharias
Prüfer der Dissertation:	
	1. Univ.-Prof. Dr. A. Haase
	2. Univ.-Prof. Dr. F. Pfeiffer

Die Dissertation wurde am 25.07.2013 bei der Technischen Universität München eingereicht und durch die Fakultät für Physik am 31.10.2013 angenommen.

BOLD-based Magnetic Resonance Imaging of Hypoxia in the Human Brain

Adaptation of Measurement and Data Analysis Strategies for Clinical Requirements

Nuria Hirsch

Abstract

Hypoxia is a pathological state where a shortage of oxygen in the tissue prevents normal metabolic function. Such a state can occur for example in brain tumors. Hypoxic niches that emerge either spontaneously or are caused by anti-angiogenic treatment promote the proliferation of tumor cells. Knowledge about the existence and location of hypoxic spots is useful for tumor surgery planning in order to remove preferably the most aggressive tumor parts. Hypoxia as a biomarker is also of use in stroke for the differentiation between affected but viable and irreparably damaged tissue where such information could be very helpful for further treatment decisions.

Methods in clinical use for the detection of hypoxia rely on immunohistochemical methods or positron emission tomography where the former includes resection of biopsy samples during surgery and the latter requires injection of a radioactive tracer. It would be desirable to have at hand a more patient-friendly method for application in routine patient examinations. Here, magnetic resonance imaging offers an option: The tissue tries to compensate the shortage of oxygen by locally increasing the oxygen extraction from blood into tissue. Since deoxyhemoglobin is paramagnetic, the magnetic susceptibility of venous blood is altered by this process. The resulting changes in the local magnetic field can be detected. In this work, existing preclinical MR methods for imaging of the brain tissue oxygenation based on magnetic field perturbations that are caused by the presence of deoxyhemoglobin in venous vessels have been assessed, adapted and optimized for the use in a clinical environment.

An imaging protocol has been developed in phantom, volunteer and patient studies where all required parameters – the transverse relaxation times $T2$ and $T2^*$ as well as the cerebral blood volume – are measured independently. The measurements can be appended to a routine clinical patient examination with an additional acquisition time of a few minutes, thus minimizing the extra strain on patients. Major confounding factors like magnetic field inhomogeneities due to local susceptibility differences, patient motion and effects arising from the pathological state of tissue are addressed in the protocol as well as in the post-processing of the acquired data.

Whole-brain maps of diagnostic quality showing relative differences in the oxygen extraction were obtained for brain tumor and stroke patients. Identification of hypoxic spots in tumorous tissue was possible with the combined information from the maps and from structural images. Application in stroke and stenosis patients revealed extensive tissue areas around the focal ischemic core that are inadequately supplied with oxygen. Although a clinically applicable protocol currently cannot provide absolute quantification, relative oxygen extraction fraction maps obtained with the presented protocol add valuable diagnostic information to routine patient examinations.

Contents

1 Introduction

Hypoxia is defined as a pathological state of tissue, where the respective tissue area is insufficiently supplied with oxygen. An imbalance between oxygen delivery and utilization in the brain is an important component in the understanding of various brain pathologies like stroke [1], Alzheimer's [2–4], Huntington's [5] and Parkinson's diseases [6] or brain tumors [7, 8].

About 50% of all primary brain tumors in adults are gliomas. They are divided into low-grade or benign (grade I and II) and high-grade or malignant (grade III and IV) gliomas [9]. Malignant gliomas are characterized by cellular heterogeneity and an infiltrating growth [10] which is promoted by tumor stem cells [11]. A hypoxic micro-environment probably stimulates the development of tumor stem cells in malignant gliomas [12]. Anti-angiogenic medication reduces the formation of new blood vessels but might also induce hypoxia and thus lead to increased infiltration and tumor growth [13–15]. The migration and invasion of tumor cells was shown to happen as a response to a hypoxic state in gliomas [16]. Furthermore, hypoxia is an important factor regarding tumor aggressiveness and prognosis as well as recurrence, metastases and resistance to radio- and chemotherapy [17–19]. Hypoxic niches are probably the hot spots of carcinogenesis and indicators of a more malignant tumor phenotype [20], which is why they should be resected during surgery as completely as possible.

The amount of oxygen that is extracted in the brain is a reliable predictor for stroke occurrence in cerebrovascular disease patients [21, 22]. It also serves to identify the ischemic penumbra [23], i. e. tissue at risk whose functional state is compromised by hypoperfusion but which still possesses morphological integrity [24]. Apart from positron emission tomography (PET) methods which are not always available, comparison of diffusion-weighted and perfusion-weighted images, the DWI/PWI mismatch method [25–28], is a common but controversial means to image the the penumbra. Another possibility is to visualize the oxygen extraction:

In order to maintain oxygen metabolism despite a reduced cerebral blood flow, a larger amount of oxygen is extracted from the blood [29]. Penumbra tissue might still be responsive to therapeutic reperfusion methods, even after the current time window for intervention of 3 to 6 hours after the onset of initial symptoms [30]. An imaging method for distinguishing tissue that is at risk of progressing to infarction but still salvageable from irreparably damaged tissue would be very helpful for therapy decisions in stroke patients.

All present methods that have been used in clinical studies for whole-brain measurement of hypoxia are based on PET [31], with the downsides of radiation exposure, spatial resolution and restricted availability. The most common marker for intracellular hypoxia imaging is fluorine-18 misonidazole (18F-FMISO). PET is also able to actually quantify the oxygen extraction with oxygen-15 tracers [32].

Immunohistochemistry provides another method to detect hypoxic tissue. Tumor cells in hypoxic niches express the hypoxia-inducible transcription factor HIF1α whose presence can be proven by the staining of biopsied tissue samples [33].

This work's focus is on the transfer, modification and optimization of to date only preclinical MR methods for hypoxia imaging with the objective of applicability in a clinical setting, where specific requirements regarding acquisition time and brain volume coverage need to be satisfied. An approach allowing for whole-brain mapping of the oxygen extraction fraction is explored which includes independent measurements of the transverse relaxation times $T2$ and $T2^*$ as well as of the cerebral blood volume. Results for $T2$ obtained with fast multiple gradient echo-spin echo measurements are tested for influences of stimulated echoes and diffusion. $T2^*$ obtained with a multiple gradient echo sequence is corrected for subject motion and susceptibility gradients caused by interfaces between different brain tissues. Contrast agent leakage frequently occurring in high-grade brain tumors is addressed in the quantification of the cerebral blood volume with dynamic and static methods. Error sources that might confound the interpretation of oxygen extraction fraction maps are evaluated in detail by comparison to anatomical images and validation with immunohistochemical methods.

The next chapter explains present MR methods for hypoxia imaging that have been performed on animals and healthy volunteers, as well as the underlying theoretical models. Furthermore, basic MR imaging methods needed in the context of the hypoxia protocol are described.
The third chapter focuses on the optimization of methods and on the de-

velopment of a clinically applicable MR protocol. Solutions to problems such as inhomogeneities of the main magnetic field, patient motion and contrast agent leakage in pathological tissue are suggested.
Results of several studies on phantoms, healthy volunteers, brain tumor and stroke patients are described in the fourth chapter. The extent of validity of the corrections is explored and an optimal selection among various available methods is made.
Error sources of all parameter measurements are discussed in Chapter 5. The preliminary validation of the method with other modalities (histopathology and PET) is described.
Concluding remarks in the last chapter review and evaluate the developed MR protocol for hypoxia imaging.

2 Methods

2.1 BOLD-based Hypoxia Imaging

2.1.1 Magnetic Properties of Blood and Blood Oxygenation

Magnetic susceptibility. The magnetic susceptibility χ describes the degree of magnetization $\boldsymbol{M}$ of a material induced by an external magnetic field $\boldsymbol{B}$,

$$\boldsymbol{M} = \chi \cdot \frac{1}{\mu}\boldsymbol{B} \tag{2.1.1}$$

with the permeability μ of the material for a magnetic field.
The internal magnetic field in biological tissue $\boldsymbol{B}_{\text{int}}$ is weakened by the presence of diamagnetic materials with $\chi < 0$ (such as water, proteins or lipids) and enhanced by paramagnetic inclusions with $\chi > 0$,

$$\boldsymbol{B}_{\text{int}} = \boldsymbol{B}_0(1 + \chi) \tag{2.1.2}$$

Diamagnetism originates from orbiting electrons producing current loops that oppose any changes in the magnetic flux (Lenz's law). However, if uncompensated magnetic moments exist (e.g. an uncompensated spin of an unpaired electron), these magnetic moments align with the field and result in additional (paramagnetic) susceptibility. Biological examples for paramagnetic materials are heme and non-heme iron or dissolved oxygen [34–36].

The balance of oxygen delivery and consumption can be detected with magnetic resonance methods thanks to the different magnetic properties of oxygenated and deoxygenated blood [37]. Hemoglobin (Hb) which is responsible for oxygen transport in the blood system contains iron ions. The paramagnetic properties of heme iron Fe^{2+} are shielded in the case of oxyhemoglobin (oxyHb), where the hemoglobin protein is saturated with

four oxygen molecules. The oxygenation process changes the electronic configuration of the heme complex, yielding a molecule with zero total spin. This is the reason for oxyHb being diamagnetic despite the presence of iron, with a similar magnetic susceptibility as gray matter.
Oxygen is extracted during the passage of the blood across the capillary network, unshielding the iron ions. Desaturated Hb without any oxygen molecules (deoxyHb) shows paramagnetic behavior. The response to a magnetic field expressed by the magnetic susceptibility χ is therefore different for deoxyHb compared to oxyHb, providing a biomarker of the blood oxygenation level in the form of the hemoglobin state [38]. The susceptibility difference between fully deoxygenated and fully oxygenated red blood cells was measured to be $\Delta\chi_0 = 0.264 \cdot 10^{-6}$ [39, 40].

The BOLD effect. The difference in blood oxygenation affects the local magnetic field homogeneity around venous vessels up to a distance of five times the vessel radius and shortens the transverse relaxation time $T2^*$. This so-called blood oxygenation level dependent (BOLD) effect based on $T2^*$ contrast was discovered in 1990 by Ogawa et al. [41] and is used in functional MRI studies to localize signal changes during brain activation [42, 43]. The BOLD signal is the volume-weighted average of the contributions of intravascular water (in blood) and extravascular water (in tissue). The extravascular contribution is by far the greater one as the volume fraction of blood in an average brain voxel is only $\sim 4\%$.

Changes in the magnetic field extend over various distances. Fluctuating microscopic field inhomogeneities over atomic and molecular lengths cause irreversible dephasing which is the cause of $T2$ relaxation. Inhomogeneities due to iron deposits occur over similarly small distances. The susceptibility differences between blood and tissue described above result in mesoscopic field changes of the size of blood cells and vessels. Imperfections of the magnet, poor shimming and boundaries between different tissues or air cavities typically lead to large-scale, macroscopic inhomogeneities extending over one or several imaging voxels. Macroscopic effects are unwelcome as they can lead to signal loss or image distortions.

The BOLD effect is also noticeable on $T2$-weighted images because water molecules diffuse around the blood vessels, which reduces the relaxation time in spin echo imaging [44].

The information in $T2^*$- and $T2$-weighted images can be combined to monitor the changes due to a varying balance of delivery and utilization of oxygen. If the actual fraction of oxygen extracted from the blood into the tissue is of interest, the cerebral blood volume (CBV) needs to be taken into account in addition to $T2^*$ and $T2$ because a larger amount of deoxyHb in

a voxel might not only originate from an increased oxygen consumption but also from an increased blood supply, i.e. from an increased CBV.

Hemodynamic parameters. Another relevant parameter in this context is the hematocrit, i.e. the volume percentage of red blood cells in blood, which is needed to convert the susceptiblity difference between oxyHb and deoxyHb into a susceptibility difference between oxygenated and deoxygenated whole blood.
The oxygen saturation fraction Y describes the amount of Hb molecules that carry oxygen compared to those without oxygen. The arterial oxygen saturation Y_a can be measured with pulse oximetry and is close to 1 while the venous saturation Y_v is about 0.6 [45].
The susceptibility difference between whole blood and tissue $\Delta\chi$ is given by

$$\Delta\chi = \chi_{\text{blood}} - \chi_{\text{tissue}} = \Delta\chi_0 \cdot \text{Hct} \cdot (1 - Y) \tag{2.1.3}$$

Eq. 2.1.3 neglects small differences between the magnetic susceptibilities of tissue, water and plasma [46]. This can become a problem in areas with iron deposition which significantly influences the local tissue susceptibility.
The oxygen extraction fraction (OEF) is defined as the ratio of oxygen consumption to oxygen delivery [47],

$$\text{OEF} = \frac{Y_a - Y_v}{Y_a} \approx 1 - Y_v \tag{2.1.4}$$

An increased physiological oxygen extraction means that the blood is depleted of a larger amount of oxygen than usual. Since the tissue mostly tries to compensate a shortage of oxygen supply by increasing the oxygen extraction, OEF can be used as an indicator for potential hypoxia.
For a summary of parameters, see Table 2.1.1.

2.1.2 Quantitative BOLD (qBOLD) Approaches

Two recent review articles summarize the development of BOLD-based techniques for the quantification of the cerebral hemodynamic and metabolic properties described below [46, 48].

Oxygenation-related effects can be examined with free induction decay (FID) experiments where the signal is given by

$$S(t) = S(0) \cdot \exp\Big(-\Gamma(t)\Big) \tag{2.1.5}$$

Symbol	Name	Definition/Description	Approx. value
BOLD	blood oxygenation level dependent	signal change due to different levels of oxygenation in the blood	n/a
CBV	cerebral blood volume	the volume fraction of a brain voxel that is taken up by blood	3-5%
$\Delta\chi$	blood-tissue susceptibility difference	susceptibility difference between whole blood and surrounding tissue	0.0924 ppm
(oxy/deoxy)Hb	(oxy-/deoxy-) hemoglobin	iron-containing metalloprotein in red blood cells for oxygen transportation	n/a
Hct	hematocrit	volume percentage of red blood cells in blood	0.42
OEF	oxygen extraction fraction	arterio-venous difference in the Hb oxygen saturation	0.4
$Y_{(a/v)}$	oxygen saturation/ oxygenation level	(arterial/venous) fraction of Hb molecules in an oxygenated state	1 / 0.6

Table 2.1.1 Overview of parameter definitions in BOLD-based measurements.

with the signal attenuation function $\Gamma(t)$. The mono-exponential signal decay governed by transverse relaxation is disturbed by a multi-compartmental tissue structure and an inhomogeneous magnetic field.
An analytical expression for the signal attenuation accounting for inhomogeneities induced by the blood vessel network was derived in Ref. [49],

$$\Gamma(t) = \mathrm{dCBV} \cdot f(t/t_c) + R2 \cdot t \tag{2.1.6}$$

on the condition of vessels being considered as randomly oriented cylinders in the magnetic field. dCBV is the deoxygenated CBV, i.e. the part of the CBV that contains deoxyHb. It is represented by prevenous capillaries and veins. Only the dCBV fraction contributes to susceptibility differences and resulting field inhomogeneities around the vessels. $R2 = 1/T2$ is the transverse relaxation rate.
Apart from spin-spin relaxation characterized by $R2$, the signal decay is also influenced by diffusion of the spins. Two time regimes need to be distinguished according to the relative impact of each effect on the signal decay: The time regime where dephasing due to molecular diffusion of water protons happens on a short time scale and cannot be neglected (the

characteristic diffusion time t_d is smaller than the characteristic dephasing time t_c) is different from the static dephasing regime (where $t_c < t_d$). t_c is given by

$$t_c = \left(\frac{4\pi}{3} \cdot \gamma \cdot B_0 \cdot \Delta\chi\right)^{-1} \tag{2.1.7}$$

and is about 7 ms at 3T. It was shown in Ref. [49] that at 3T the static dephasing regime is valid for blood vessels with a radius larger than 6 μm, corresponding to the post-capillary network.
The function $f(t/t_c)$ in Eq. 2.1.6 has a different time dependence in the short compared to the long time regime:

$$f(t/t_c) = \begin{cases} 0.3 \cdot (t/t_c)^2, & t/t_c \ll 1 \\ t/t_c - 1, & t/t_c \gg 1 \end{cases} \tag{2.1.8}$$

Two general approaches exist to obtain information about $\Delta\chi$ (and therefore about Y and OEF, with Eqs. 2.1.3 and 2.1.4) from the signal attenuation function $\Gamma(t)$ defined in Eq. 2.1.6. The first one is to perform gradient echo sampling of a spin echo (GESSE), where the sampling time interval in the short time regime is doubled by acquiring the signal around the spin echo [45]. A fit of GESSE data yields values for the fitting parameters dCBV and $\Delta\chi$. Another approach is restricted to the long time regime, when dCBV$\cdot\Delta\chi$ appears as a product in the equations. In this case, independent measurements for dCBV and the parameters related to $\Delta\chi$ need to be performed [50]. Both alternatives are described in the following.

The GESSE approach. The GESSE sequence features multiple gradient echoes placed around a single spin echo. The signal is read out for gradients of the same polarity to avoid distortions in the images due to macroscopic field inhomogeneities that can occur if alternating gradients are used. The signal attenuation function for the GESSE sequence is

$$\Gamma_{\mathrm{GESSE}} = \mathrm{dCBV} \cdot f\Big(t/t_c + R2 \cdot (t + TE)\Big) \tag{2.1.9}$$

where t is the time interval between acquisition and the spin echo at TE, starting at $-TE/2$. This acquisition technique extends the short time regime with a quadratic dependence of f on t/t_c, which is important for the decoupling of dCBV and $\Delta\chi$, over a wider time range and thus provides a longer sampling time [51].

The GESSE approach has been validated for a phantom of polyethylene tubes [51] and in animals by manipulating the venous oxygen saturation

with various anesthesia methods and inhalation of air with different oxygen saturation levels, combined with the analysis of blood samples from the sagittal sinus [52].
The first test of GESSE on healthy humans was performed by An and Lin in the year 2000 [53]. Their result in eight subjects was $Y = 58 \pm 2\%$, however with an unrealistically high CBV of $16 \pm 7\%$. The problem was recognized later by He and Yablonskiy as the result from neglecting the multi-compartmental structure of tissue. Consequently, they modeled the qBOLD signal acquired with GESSE as a sum of contributions from an extravascular tissue compartment with intermediate $T2$, from an interstitial/cerebrospinal fluid (ISF/CSF) compartment with long $T2$ and from an intravascular compartment, with the signal amplitudes from CSF/ISF and from blood being a lot smaller than the extravascular contribution. Their study on 9 healthy humans covering multiple 6 mm slices with an acquisition time of 8 min 30 sec revealed a rather homogeneous OEF over the whole brain of $38.3 \pm 5.3\%$ [45]. PET measurements of OEF produced values between 35% and 43% [54–57]. However, when using the multi-compartment GESSE method a very high signal to noise ratio of SNR$>$ 500 is required for a reliable estimation of parameters from the multi-parameter fit. This approach is therefore not useful for patient examinations where images often exhibit a much poorer quality.

Determination of parameters by independent measurements. A study by Sedlacik and Reichenbach validated the Yablonskiy model of blood vessels in the brain as a network of randomly oriented cylinders in the case of negligible diffusion with a polypropylene strings/silicone phantom [58]. However, they found that a strong interdependency between deoxygenated blood volume and OEF exists for the single-compartment GESSE approach, and different pairs of parameters can be found that will result in the same fitted signal. This behavior was confirmed by measurements of healthy volunteers. Consequently they suggested independent measurements of the model parameters whenever SNR < 200.

An equation for OEF containing independently measurable parameters can be derived for the long time static dephasing regime. According to Eqs. 2.1.5, 2.1.6, 2.1.7 and 2.1.8, the signal equation in this regime is

$$\begin{aligned} S(t) &= S(0) \cdot \exp\Big(- \big(\mathrm{dCBV} \cdot t/t_\mathrm{c} - \mathrm{dCBV} + R2 \cdot t\big)\Big) \\ &= S(0) \cdot \exp\Big(- \big(- \mathrm{dCBV} + (R2 + \mathrm{dCBV}/t_\mathrm{c}) \cdot t\big)\Big) \end{aligned} \tag{2.1.10}$$

The transverse relaxation is influenced by $R2$ and $\mathrm{dCBV}/t_\mathrm{c}$ to yield $R2^* = R2 + R2'$, where $R2$ characterizes irreversible transverse relaxation and

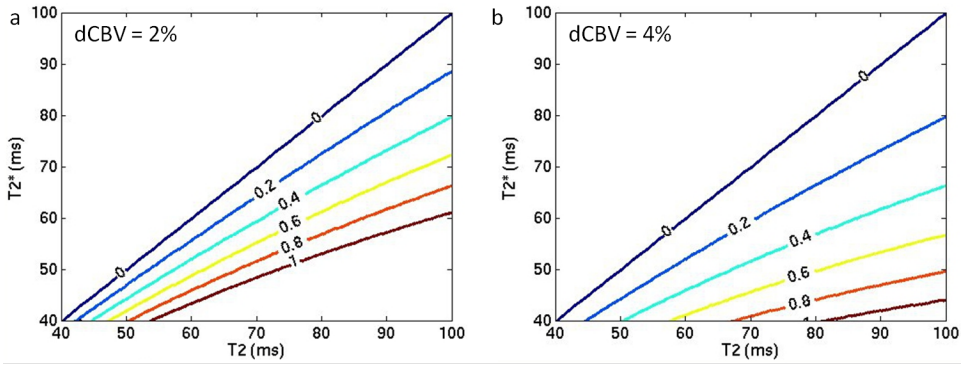

Figure 2.1.1 Dependence of the oxygen extraction fraction on the values for transverse relaxation times $T2$ and $T2^*$ and the deoxygenated blood volume dCBV as determined by Eq. 2.1.13 at 3T. dCBV is set to 2% (a) and 4% (b). The labels in the figures denote OEF values.

$R2'$ characterizes the dephasing due to mesoscopic field inhomogeneities caused by deoxyHb. Considering Eq. 2.1.7, $R2'$ is given by

$$R2' = \mathrm{dCBV}/t_c = \frac{4\pi}{3} \cdot \gamma \cdot B_0 \cdot \Delta\chi \cdot \mathrm{dCBV} \tag{2.1.11}$$

Hence, $\Delta\chi$ can be determined by independent measurements of

$$R2' = 1/T2^* - 1/T2 \tag{2.1.12}$$

and the deoxygenated blood volume, accompanied by an increase in the robustness compared to qBOLD with GESSE. Assuming fully oxygenated arterial blood, OEF is calculated with Eqs. 2.1.3, 2.1.4 and 2.1.11 as

$$\begin{aligned} \mathrm{OEF} \approx 1 - Y &= \frac{\Delta\chi}{\Delta\chi_0} \cdot \frac{1}{\mathrm{Hct}} \\ &= \frac{R2'}{4\pi/3 \cdot \gamma \cdot B_0 \cdot \Delta\chi_0 \cdot \mathrm{Hct} \cdot \mathrm{dCBV}} \end{aligned} \tag{2.1.13}$$

The behavior of OEF according to Eq. 2.1.13 is illustrated in Fig. 2.1.1. The figure shows that all three input parameters need to be determined with high accuracy because small changes in each parameter have a strong impact on the actual value obtained for OEF. Also, the difference between $T2$ and $T2^*$ is expected to be not too large at 3T in order to yield a physiological OEF of about 0.4.

The multi-parametric, single-compartment approach was first implemented by Christen et al. in 2011 and tested in simulations, on animals and

on 12 healthy volunteers ($Y = 60 \pm 6\%$) [50, 59, 60]. Christen et al. used ultrasmall superparamagnetic iron oxide (USPIO) particles to quantify total CBV in rats. USPIO remains intravascular and does not leak into the tissue but is only available for animal studies. In humans, they used a combined arterial spin labeling/perfusion-weighted imaging (ASL/PWI) method for CBV quantification, which is rather time-consuming and not suited for patient application. Also, whole-brain coverage was not achieved: Data from multiple axial slices in a slab of 12 mm thickness were acquired in 15 minutes.
The aim of this thesis was to establish a similar method for OEF mapping that is robust enough for patient measurements and facilitates whole-brain coverage in a few minutes in order to be applicable for examinations of extended pathological tissue in the human brain.

In the following chapters independent quantification methods for $T2^*$ using gradient echo imaging, for $T2$ using spin echo imaging and for CBV using various approaches are described, as well as the protocol optimization for application on patients in a clinical environment where fast and robust data acquisition is an absolute necessity.

2.2 Gradient Echo Imaging

Gradient echoes. The generation of gradient echoes with a pair of gradients of opposite polarity is illustrated in Fig. 2.2.1. An excitation pulse first tilts the magnetization by a flip angle α from being parallel to the main magnetic field towards the transverse plane. If the whole process is to be repeated, smaller angles than 90° and a reduced repetition time TR can be used to speed up the measurement. A gradient is switched on that causes the spins to dephase more rapidly than they would normally do. After some time the dephasing gradient is switched off and a rephasing gradient is applied in the opposite direction. The formerly more slowly precessing spins now have higher precession frequencies according to their position in the changed total magnetic field, and vice versa, until all spins are in phase and precess with the same frequency once more. The first gradient thus dephases the spins; the second gradient rephases them. The time between the excitation pulse at the beginning and the time point when a gradient echo is created is called the echo time TE. The signal weakens with increasing echo time because the rephasing gradient only compensates the effect of the dephasing gradient. Dephasing due to inhomogeneities in the main magnetic field or due to spin-spin relaxation processes is not reversed. Consequently, the gradient echo signal depends

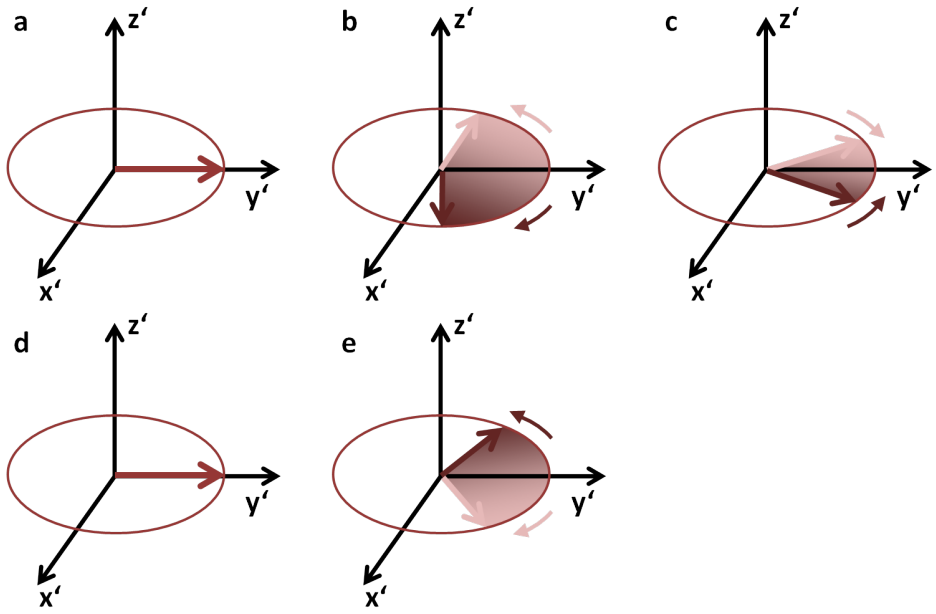

Figure 2.2.1 Creation of a gradient echo in the rotating frame (see Section A.1.1 for an explanation of the rotating frame). a) All spins are in phase right after being flipped onto the transverse plane. b) The natural dephasing of the spins is accelerated by a dephasing gradient. The spins are fanning out. c) A rephasing gradient of the same strength but opposite polarity inverts the motion direction of the spins so that they draw near each other again. d) A gradient echo is produced when the spins are in phase again. e) The spins keep on moving and dephase.

on $T2^*$,

$$S_{\mathrm{GE}}(TE) = S_0 \cdot \exp\left(-\frac{TE}{T2^*}\right) \tag{2.2.1}$$

S_0 is the amplitude of the signal right after the excitation pulse.

Data are sampled during the echo inducing a signal in a coil that represents the inductance of a circuit tuned to the Larmor frequency of protons.

Fast Low Angle Shot (FLASH). In order to accelerate gradient echo imaging for example for anatomical acquisitions, very low flip angles and a short TR are used. The echo time is chosen as short as possible to suppress artifacts from susceptibility gradients.
High resolution $T2^*$-weighted Fast Field Echo[1] (FFE) images are useful for the detection of small bleeding areas in the brain. If $T1$ contrast is desired, a spoiler gradient is applied after each echo to destroy any remaining transverse magnetization. The longitudinal magnetization is not destroyed but preserved for the next echo.

[1] Field echo is the Philips acronym for gradient echo.

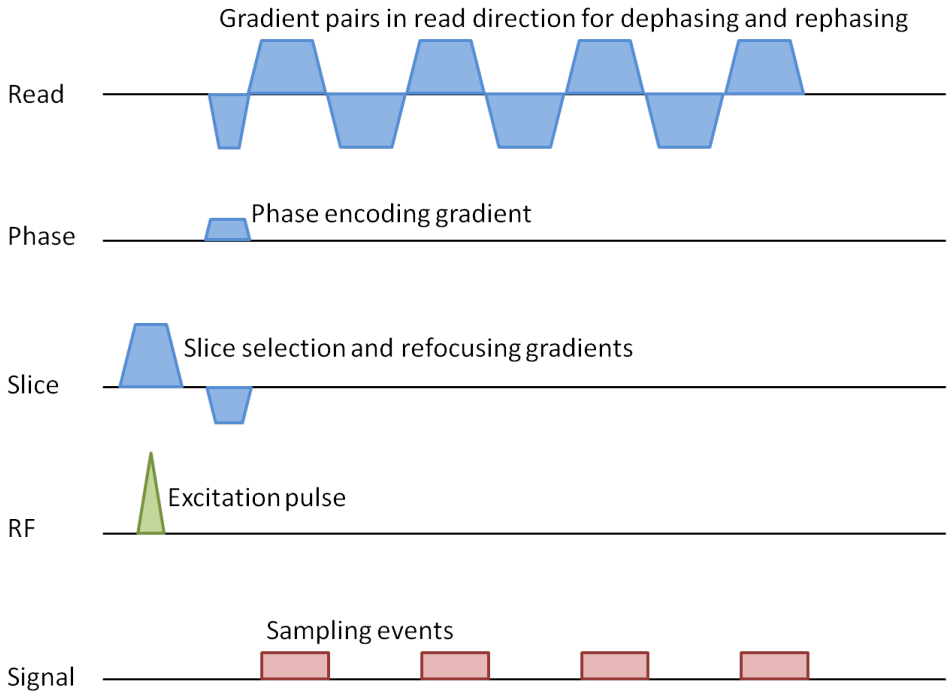

Figure 2.2.2 Exemplary multi-gradient echo sequence with 4 echoes. Read, Phase and Slice denote the three imaging gradient directions, RF shows the position of RF pulses. Signal acquisition events are shown at the bottom.

Multi-gradient echo imaging. $T2^*$ can be determined if multiple pairs of bipolar gradients are used after the excitation. Each echo produces a weaker signal than the one before, with $T2^*$ governing the exponential decay. A pulse sequence diagram of a multi-gradient echo sequence with 4 bipolar gradient pairs is shown in Fig. 2.2.2.
Since imperfections of the main magnetic field are in fact additional gradients that are not rewound, the quality of gradient echo images is heavily influenced by macroscopic field inhomogeneities. A correction method for diminishing the susceptibility effects of air cavities and iron-rich structures in the brain which locally disturb the B_0 field is described in Section 3.1.

Magnetization-Prepared Rapid Acquisition by Gradient Echo (MPRAGE) and Turbo Field Echo Imaging (TFE). A very short TR together with a small flip angle produces weak $T1$ contrast which can be enhanced by preparing the magnetization with a 180° inversion pulse (TurboFLASH). The effective inversion time TI is defined as the time interval from the inversion pulse to the acquisition of the k-space center.
MPRAGE is a 3D modification of TurboFLASH suitable for fast, high-resolution anatomical acquisitions. It is called $T1$-weighted TFE on Philips

scanners, with the additional preparation pulse distinguishing it from FFE.

Echo Planar Imaging (EPI). EPI is a fast readout technique where a whole slice is acquired after one excitation (single shot). EPI can be $T2^*$-weighted (gradient echo-based, as in Fig. 2.2.3) or $T2$-weighted (spin echo-based, see next Section). A phase encoding gradient that moves the position in k-space to an outer corner is applied after the slice-selective excitation pulse. Repeated inversion of read gradients produces echoes to fill the k-space line by line. A short phase encoding gradient (blip) is applied at each read gradient reversal in order to move on to the next k-space line until the whole k-space is acquired. The echo time increases for each k-space line with the echo spacing ΔTE. TE as defined in the protocol is an effective echo time from the excitation to the acquisition of the central k-space line.
Since the protons in fatty tissue have a slightly different resonance frequency than those in watery tissue, the conversion of frequencies to locations by a Fourier transform leads to spatial shifts of voxels containing mainly lipid protons (chemical shift). EPI is very sensitive to chemical shift artifacts due to the small bandwidth in phase encoding direction because of the short blips and the resulting small changes in frequency used for spatial encoding. An effective suppression of the signal arising from fat by special pulses and gradients is therefore important whenever EPI is used. EPI is also prone to other artifacts due to field inhomogeneities and imperfections of the rapidly switching gradients, resulting in ghosts and distortions. The FID imposes a time limit on the acquisition so that the attainable spatial resolution is restricted.

2.3 Spin Echo Imaging

Spin echoes. The generation of spin echoes is illustrated in Fig. 2.3.1. The spins dephase after being flipped by the excitation pulse because of slight differences and local perturbations by neighboring spins in the magnetic field. A 180° pulse is applied at $t = TE/2$ that flips the spins around one transverse axis. The precession frequencies and the motion directions in the rotating frame are not changed but the phase difference of a spin compared to another is inverted. If it has accumulated a positive phase difference previously due to faster precession, it has now a negative phase difference. In the time interval until the echo is formed it catches up again due to its still faster precession. The echo is formed at $t = TE$ when most of the spins are in phase again.

The perturbation by neighboring spins cannot be reversed, which is

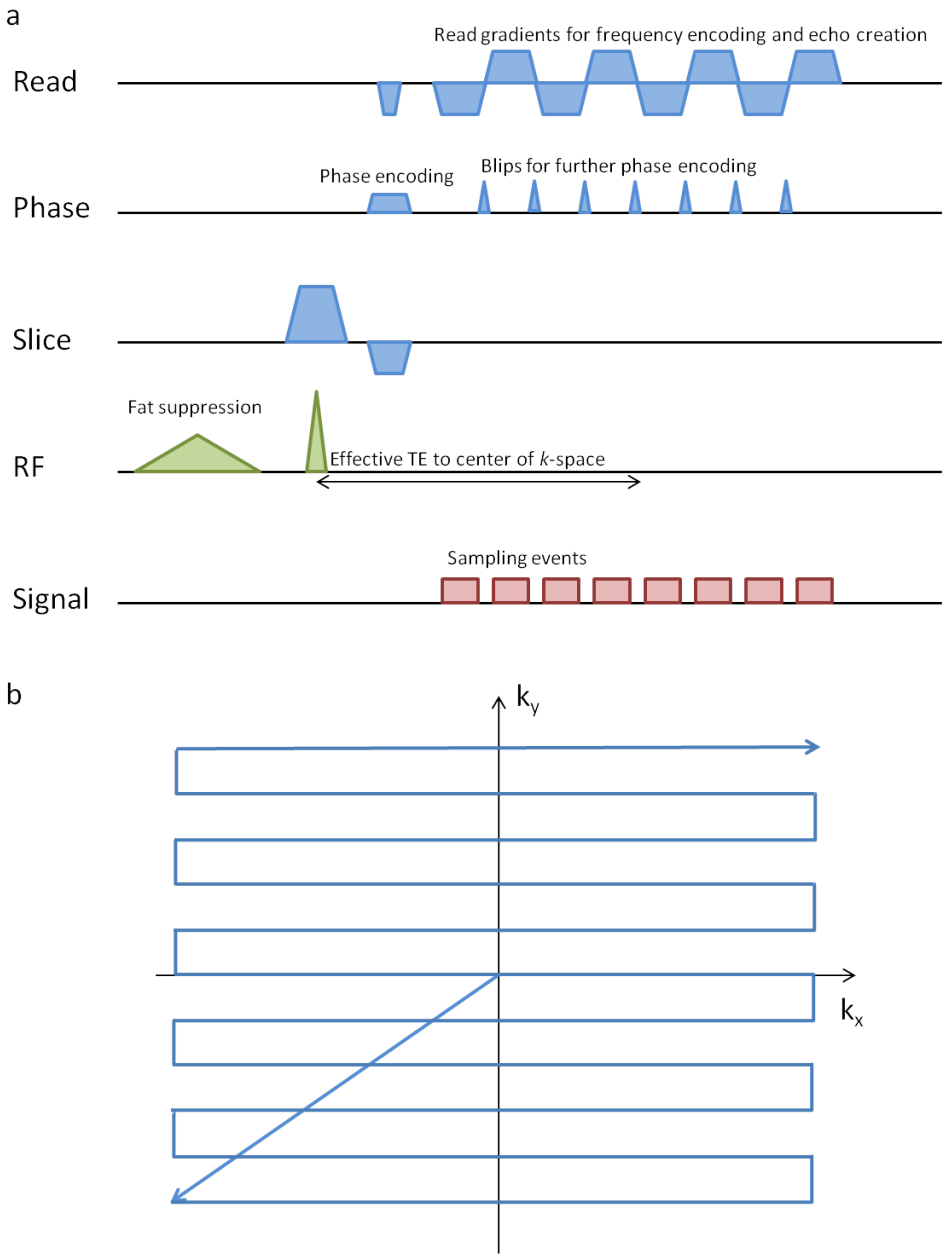

Figure 2.2.3 Gradient echo-based EPI readout. a) Schematic single-shot EPI sequence. b) Path in k-space as defined by the read and phase gradients of the sequence.

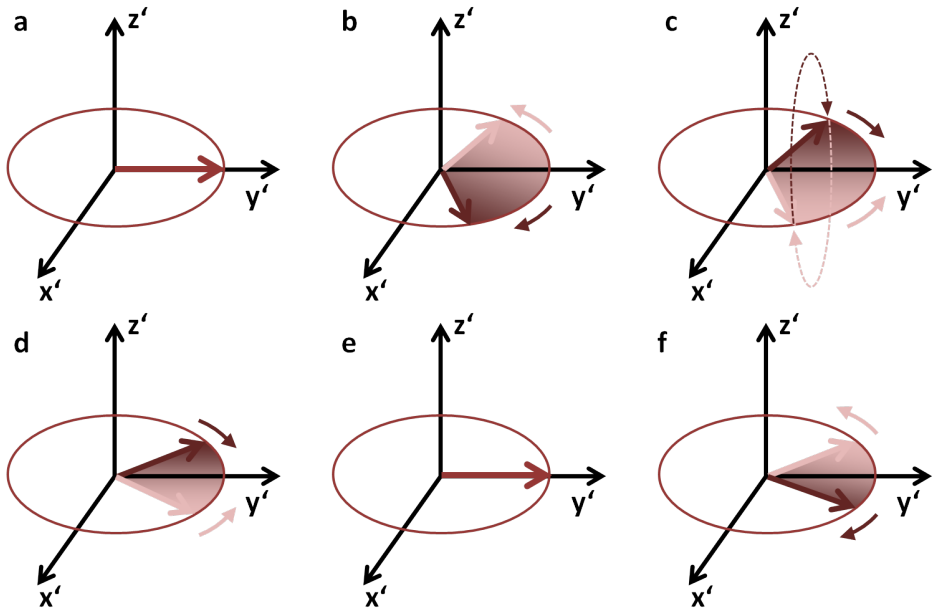

Figure 2.3.1 Creation of a spin echo in the rotating frame. a) Right after being flipped onto the transverse plane, all spins are in phase. b) The spins are dephasing naturally. c) A 180° pulse is applied which flips the spins around the y' axis back onto the transverse plane. The direction of motion is unchanged. d) Spins formerly precessing with a higher frequency are still precessing more rapidly but are now lagging behind the others in terms of phase difference. e) After some time all spins are in phase again and a spin echo is formed. f) The spins dephase again.
Please note: In this illustration the 90° pulse is applied along the x' axis and the refocusing 180° pulse along the y' axis, as in a CPMG sequence (see Section 2.3). Another possibility to generate a spin echo is to apply both the excitation and the refocusing pulses in phase along the same axis. In this case the original transverse magnetization and the echo are out of phase by 180°.

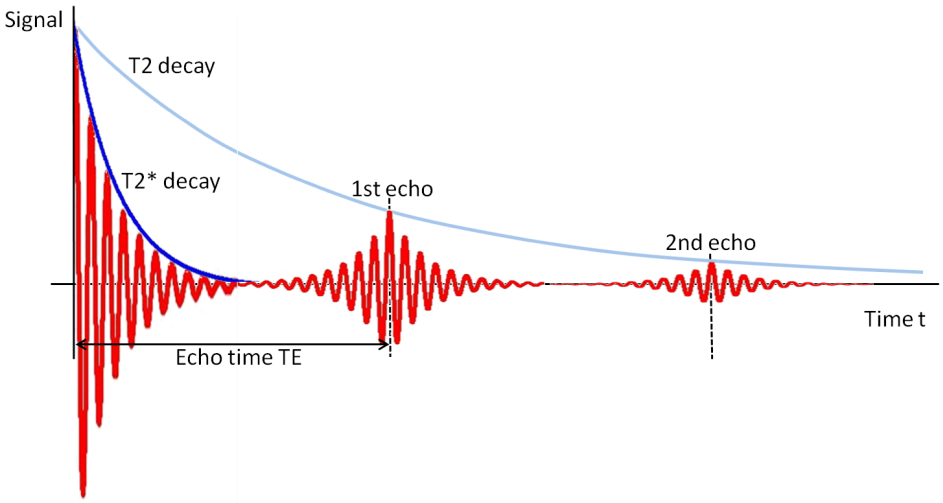

Figure 2.3.2 Signal development during a multi-spin echo acquisition.

why multiple spin echo signals decay in strength. The apparent local field gradients that the spins experience are inverted by the 180° flip. If the spins do not change their positions due to diffusion effects (see the paragraph on DWI below), they experience the same local field inhomogeneities twice but with opposite polarity. The effect of temporally constant field inhomogeneities is therefore cancelled out and the signal decays with $T2$ due to the thermal motion of the spins that leads them randomly into different regions in the magnetic field:

$$S_{\mathrm{SE}}(TE) = S_0 \cdot \exp\left(-\frac{TE}{T2}\right) \tag{2.3.1}$$

It should be noted that any two successive RF pulses (not necessarily $90° - 180°$) lead to the generation of a spin echo because they form a spectral distribution of magnetic moment components in the transverse plane. After freely precessing for some time, they interfere constructively to produce an echo. This effect was discovered in 1950 by Erwin Hahn [61]. 180° pulses just maximize the transverse part of the magnetization.

$T2$ is quantified by sampling the signal decay with a series of spin echo images at increasing echo times. The measured signal intensities of subsequent echoes follow an exponential decay governed by $T2$ whereas the decay within single echoes is governed by $T2^*$ (Fig. 2.3.2).

Carr-Purcell-Meiboom-Gill (CPMG) sequence. A CPMG sequence consists of a 90° excitation pulse along the x' axis and a train of equally spaced 180° pulses along the y' axis [62, 63]. While odd echoes are formed

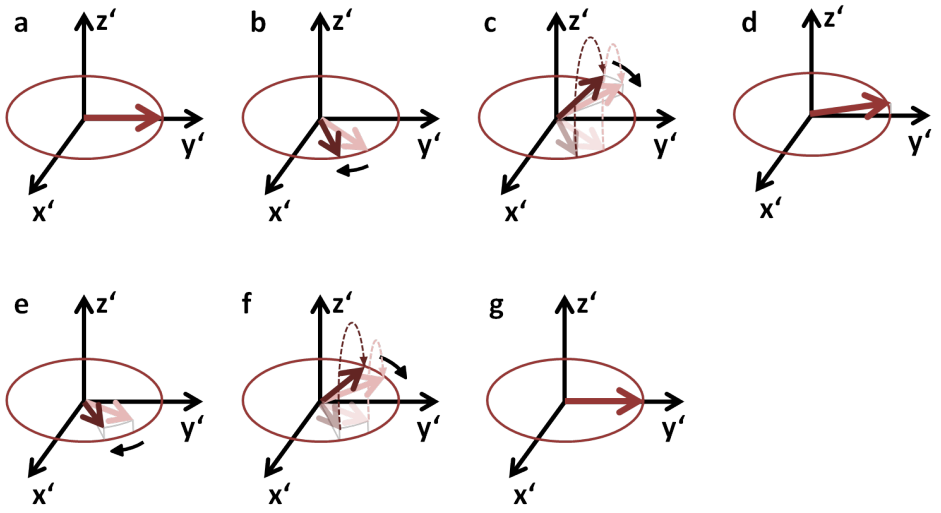

Figure 2.3.3 CPMG sequence. a) Transverse magnetization is formed along the y' axis right after the 90° excitation pulse along the x' axis. b) Two exemplary spins are shown, both precessing in the same direction but with slightly different frequencies. c) An imperfect (180°-ε) pulse is applied along the y' direction. The spins are now slightly tilted against the $x'y'$ plane. d) The first echo is formed in a plane which is slanted against the transverse plane. e) The spins are again dephasing. f) The second imperfect refocusing pulse flips the spins back onto the transverse plane. g) The second echo is formed in the transverse plane.

in a plane that is slanted against the transverse plane if the spins are not flipped by exactly 180° and thus produce weaker signals, effects from imperfections of the refocusing pulses cancel out in even echoes and do not accumulate over the length of the echo train. A detailed explanation of the response of the spins towards imperfect pulses during the course of a CPMG sequence is given in Fig. 2.3.3.
Multi-spin echo sequences on commercial MR scanners usually include a CPMG excitation and refocusing scheme with the excitation and refocusing pulses being 90° out of phase. Only the signal from even echoes is used for $T2$ quantification to avoid accumulated effects from imperfect refocusing pulses.

Turbo Spin Echo Imaging (TSE). Additional echoes generated by multiple 180° pulses might not only be used for acquiring a time series to sample $T2$ decay but also to speed up the acquisition of a single $T2$-weighted image (Turbo or Fast Spin Echo Imaging), provided the echoes are equipped with different phase encodings, similar to EPI. The phase encoding gradient needs to be rewound before the next echo. The number of spin echoes is called the Turbo factor. Each echo is used to fill one line

of k-space; different lines have different $T2$ weighting. The effective echo time TE is the time until the center of k-space is acquired.

Gradient Echo–Spin Echo Imaging (GRASE). The TSE and EPI concepts to accelerate the acquisition by using multiple spin and gradient echoes to fill the k-space lines can be combined into a hybrid sequence called GRASE: Multiple k-space lines are acquired during each spin echo with the help of gradient echoes i.e. an EPI readout. Each gradient echo possesses different phase encoding (see phase encoding blips in Fig. 2.3.4). Since adjacent lines in k-space are not filled by successive echoes, the $T2$ decay between lines makes GRASE prone to ringing artifacts. However, the acquisition time of TSE imaging can be reduced even further with GRASE by a factor corresponding to the number of gradient echoes (the EPI factor).
For $T2$ quantification with GRASE, where a time series of spin echoes needs to be acquired, each spin echo is used to encode one complete image of the time series.
Closely related to GRASE is spin echo EPI (SE-EPI) where only one refocusing pulse is used and all of k-space is filled during a single spin echo.

Diffusion-Weighted Imaging (DWI). The spin echo signal is not only weakened by spin-spin interactions characterized by $T2$ but also by the random molecular motion or self-diffusion of water protons. As diffusing water molecules change their positions, they experience different local fields if field inhomogeneities are present. This modifies their resonance frequencies and adds to the loss in phase coherence.
Carr and Purcell modeled diffusion as a random walk of discrete steps [62]. In the limit of infinitesimal steps they derived the following equation for a spin echo sequence consisting of a 90° excitation pulse and multiple 180° refocusing pulses:

$$S(t) = S_0 \cdot \exp\Big(-\frac{t}{T2}\Big) \cdot \exp\Big(-\frac{\gamma^2 G^2 D t^3}{12 n^2}\Big) \tag{2.3.2}$$

S_0 is the signal at equilibrium, G is the gradient strength, D is the molecular self-diffusion constant of the sample, and n is the number of applied 180° pulses.
Provided large enough gradients are used, diffusion-weighted images are produced: Usually, a 90° - 180° radiofrequency pulse pair is used for creating a spin echo. Additionally two large, equal gradients are placed before and after the 180° pulse. For protons moving along the direction of the gradients, the gradient pair leads to loss in phase coherence that cannot be reversed by the refocusing pulse. The degree of diffusion weighting

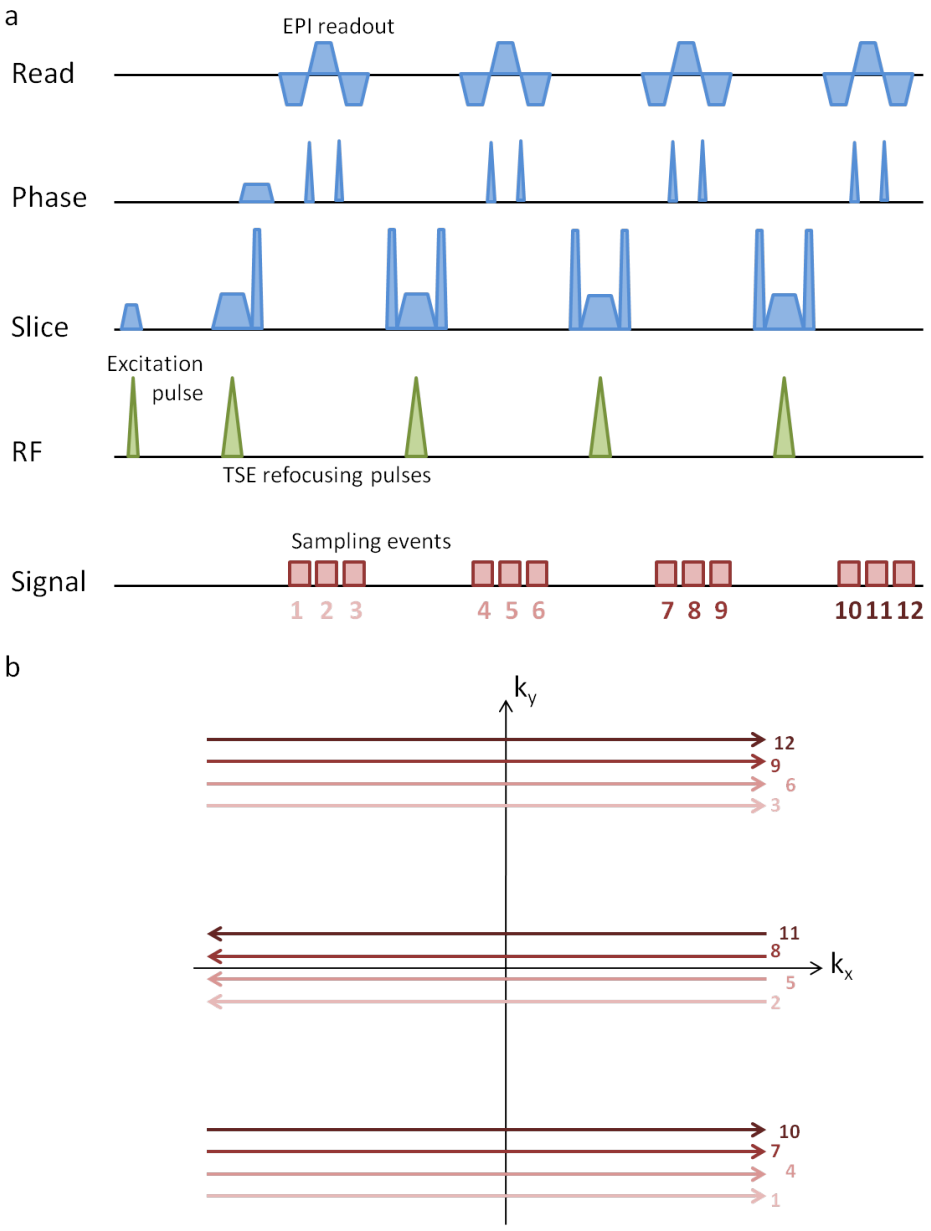

Figure 2.3.4 GRASE is a combination of TSE and EPI. a) Schematic GRASE sequence. The number of refocusing pulses for the generation of spin echoes (as in TSE imaging) is called the Turbo factor while the number of gradients for EPI readout is the EPI factor. Small colored numbers denote echo acquisitions. b) Each echo is used to fill a line of k-space. The colored numbers show the filling scheme corresponding to the acquisition of echo signals.

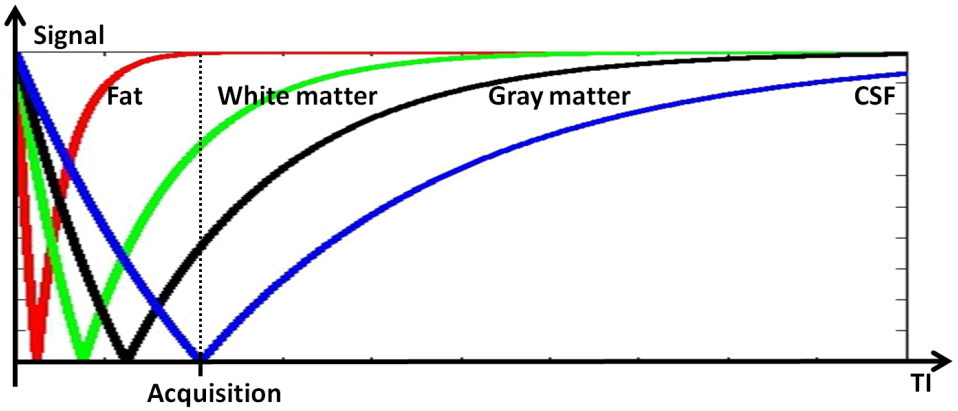

Figure 2.3.5 FLAIR is an inversion recovery sequence where the image is acquired when the CSF signal has its zero crossing. $T2$ weighting is achieved by a series of spin echoes. A long TR is chosen to eliminate $T1$ contrast.

is determined by the direction, strength, duration and separation of the gradient pair.

Protons in watery tissues exhibit a larger mobility resulting in a lower signal, while more solid tissues appear brighter in DWI images. A single gradient pair introduces diffusion weighting only along the gradient direction. If gradient pairs are applied in multiple directions and the signal in a voxel is weakened by the same amount in all gradient directions, the diffusion in this voxel is isotropic. On the other hand, if differences are observed, the diffusion is restricted in some directions, for example by physical barriers like cell membranes in white matter fiber tracts. This provides a possibility to image fiber directions in the brain. The fractional anisotropy (FA) is therefore a parameter of interest in DWI, FA $= 0$ representing isotropic and FA $= 1$ indicating highly directional diffusion.

SE-EPI is commonly used for diffusion imaging, where the RF pulse pair and the diffusion gradient pair are placed as preparations at the beginning of the sequence.

DWI is an established method for early detection of ischemic stroke because infarcted tissue with decreased apparent diffusion appears bright. The reason for this are changes of the energy metabolism in cells resulting in a net transfer of water from the extracellular to the intracellular space. Since intracellular water is more immobile, the overall diffusion is lowered.

Diffusion tensor imaging (DTI) is a more sophisticated, quantitative form of DWI, where the diffusion properties of the tissue are characterized in terms of gradient and voxel orientations.

Fluid Attenuated Inversion Recovery (FLAIR). FLAIR is a $T2$-weighted inversion recovery sequence with TSE readout. The longitudinal magnetization is inverted by a 180° pulse. The time until slice excitation called inversion time TI is adjusted to the $T1$ relaxation of cerebrospinal fluid (CSF) such that the signal from CSF has its zero crossing at the time of acquisition ($T1_{\mathrm{CSF}} \approx 2990$ ms at 3T, Fig. 2.3.5). The effective echo time TE defines the time between the excitation and the center of k-space acquisition.
FLAIR is usually performed to screen for lesions close to cerebrospinal fluid areas that would otherwise be covered by the bright fluid signal.

2.4 Mapping of the Cerebral Blood Volume

An overview on methods for measuring the fractional cerebral blood volume (CBV) can be found in several review papers on the subject [64, 65].
Most MR methods for CBV quantification are based on altering the relaxation behavior by injection of a paramagnetic contrast agent (e.g. Gd-DTPA) into the blood vessel system.
In dynamic methods, the passage of the contrast agent bolus is monitored with $T2^*$- or $T1$-weighted sequences. The short bolus transit time of only a few seconds necessitates the use of fast imaging methods to provide sufficient temporal resolution of the bolus passage.
The high magnetic susceptibility of the contrast agent molecules leads to a signal drop in gradient echo images caused by small variations in the local magnetic field, similar to the BOLD effect. The decrease in signal intensity is not only an intravascular effect but is also visible around the vessels because tissue water protons can diffuse into areas affected by contrast agent induced gradients ($T2^*$ effect). The signal increase in $T1$-weighted methods occurs because the contrast agent possesses unpaired electrons which are likely to interact with nearby water molecules, speeding up spin-lattice relaxation of the water protons ($T1$ effect). CBV is calculated from the signal drop (in the case of $T2^*$) or increase (for $T1$) relative to the baseline before the contrast agent has entered the imaging voxel.
In steady-state methods, images before and after the application of contrast agent are compared to find the distribution volume of the contrast agent.
Due to its molecular size and low lipophilicity the contrast agent is assumed to remain intravascular for the duration of the scan. However, this is not entirely true especially in pathologies that locally disrupt the blood brain barrier (see Section 3.3 for a more detailed description of leakage

correction).

2.4.1 Steady-State Methods

Vascular Space Occupancy (VASO)

Vascular space occupancy is a steady-state method where the first image is acquired before contrast agent administration at a time TI after inverting the magnetization [66]. TI is selected such that the signal arising from blood is nulled (Fig. 2.4.1 a). The second image is acquired after contrast agent administration with the same parameters as the first acquisition. With suitable TR, full relaxation of the contrast agent-enriched blood is achieved in the second acquisition, and blood contributes the maximum possible signal (Fig. 2.4.1 b). The blood signal is isolated by subtracting both images.
CBV is easily calculated from the difference signal: With A being the signal per unit volume of water protons at equilibrium, C_{par} and C_{blood} being the water proton densities of parenchyma and blood in mL of water per mL of parenchyma or blood, and $T1_{\text{tissue}}$ and $T1_{\text{blood}}$ being the longitudinal relaxation times of tissue and blood, the pre-contrast signal S_{pre} is

$$\begin{aligned} S_{\text{pre}} &= S_{\text{tissue}} + S_{\text{blood}} \\ &= A \cdot \left(\left(C_{\text{par}} - \text{CBV} \cdot C_{\text{blood}} \right) \cdot \left(1 - 2 \cdot \exp\left(- \frac{TI}{T1_{\text{tissue}}} \right) \right) + 0 \right) \end{aligned} \tag{2.4.1}$$

while the post-contrast signal S_{post} is

$$\begin{aligned} S_{\text{post}} &= S_{\text{tissue}} + S_{\text{blood}} \\ &= A \cdot \left(\left(C_{\text{par}} - \text{CBV} \cdot C_{\text{blood}} \right) \cdot \left(1 - 2 \cdot \exp\left(- \frac{TI}{T1_{\text{tissue}}} \right) \right) \right. \\ &\qquad \left. + \text{CBV} \cdot C_{\text{blood}} \cdot \left(1 - 2 \cdot \exp\left(- \frac{TI}{T1_{\text{blood, post}}} \right) \right) \right) \end{aligned} \tag{2.4.2}$$

Since $T1$ of blood is shortened considerably by the contrast agent so that the assumption $T1_{\text{blood, post}} \ll TI$ holds, the exponential term with $T1_{\text{blood, post}}$ in Eq. 2.4.2 can be neglected, and CBV is given by

$$\text{CBV} = \frac{S_{\text{diff}}}{A \cdot C_{\text{blood}}} \tag{2.4.3}$$

where S_{diff} is the difference signal $S_{\text{post}} - S_{\text{pre}}$.
The normalization factor can be determined in two ways: Either the prod-

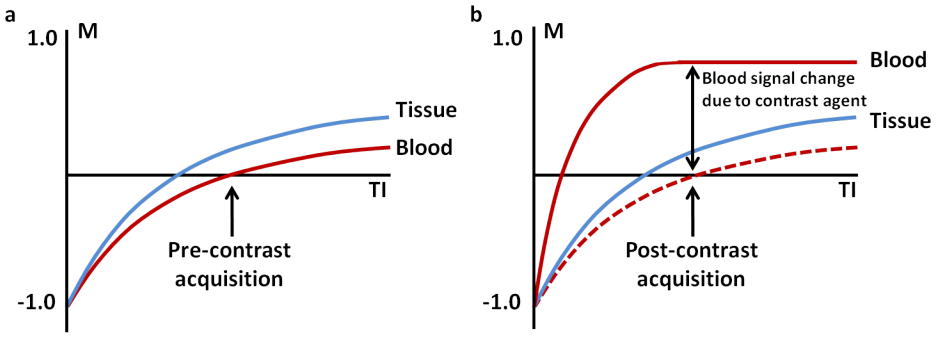

Figure 2.4.1 Illustration of the VASO sequence timing. a) Pre-contrast agent acquisition. The blood signal is nulled. Only the tissue signal is measured. b) Post-contrast acquisition. The image is acquired after the same inversion time as the pre-contrast image. The contribution from tissue to the image signal is the same but the signal from blood is maximized since the relaxation of blood spins was accelerated by the contrast agent. The tissue signal is eliminated by subtracting both images.

uct $A \cdot C_{\text{blood}}$ is determined by measuring the signal of a pure blood voxel in the post-contrast acquisition, or C_{blood} is taken from literature and A is determined in a separate reference scan from the fully relaxed signal of a CSF voxel.

VASO can be performed in a short time with high resolution (about 35 sec for each of the two acquisitions and about 20 sec for the reference scan for whole-brain coverage with $2 \times 2 \times 3$ mm^3). It is an absolute quantification method for CBV that does not rely on a linear dependence of change in the relaxation rate and contrast agent concentration which is assumed in dynamic methods. Neither does it require knowledge about the arterial input function. However, the long single volume acquisition time of VASO make it very prone to patient motion artifacts.

Accounting for Contrast Agent Leakage in VASO

The original VASO model [66] assumes the existence of two compartments, a vessel compartment where the relaxation behavior is influenced by the presence of the contrast agent, and a tissue compartment which remains free of contrast agent for the whole measurement time. Leakage of contrast agent into the tissue can be accounted for if the tissue compartment is split up into an intracellular compartment where contrast agent does not leak into, and extravascular extracellular space (EES) which the contrast agent

can enter. Eq. 2.4.2 is substituted in leakage areas by

$$\begin{aligned} S_{\text{post, leak}} &= S_{\text{tissue-CA}} + S_{\text{tissue+CA}} + S_{\text{blood}} \\ &= A \cdot \Bigg(\Big(C_{\text{par}} - v_{\text{e}} \cdot C_{\text{par}} - \text{CBV} \cdot C_{\text{blood}} \Big) \\ &\qquad \cdot \Big(1 - 2 \cdot \exp\Big(- \frac{TI}{T1_{\text{tissue}}} \Big) \Big) \\ &\qquad + v_{\text{e}} \cdot C_{\text{par}} \cdot \Big(1 - 2 \cdot \exp\Big(- \frac{TI}{T1_{\text{tissue, post}}} \Big) \Big) \\ &\qquad + \text{CBV} \cdot C_{\text{blood}} \cdot \Big(1 - 2 \cdot \exp\Big(- \frac{TI}{T1_{\text{blood, post}}} \Big) \Big) \Bigg) \end{aligned} \tag{2.4.4}$$

$S_{\text{tissue-CA}}$ and $S_{\text{tissue+CA}}$ are signal contributions from the tissue compartments without contrast agent (corresponding to intracellular space) and with contrast agent (corresponding to EES with a volume fraction v_{e}). The relaxation time of tissue with contrast agent, $T1_{\text{tissue, post}}$, now enters the equation. However, since $T1_{\text{tissue, post}}, T1_{\text{blood, post}} \ll TI$, the exponential terms with contrast agent-influenced relaxation times can again be neglected.
A corrected CBV_{corr} is obtained from $S_{\text{diff, leak}} = S_{\text{post, leak}} - S_{\text{pre}}$ (with S_{pre} from Eq. 2.4.1), and results in

$$\text{CBV}_{\text{corr}} = \text{CBV} - 2 \cdot v_{\text{e}} \cdot \frac{C_{\text{par}}}{C_{\text{blood}}} \cdot \exp\Big(- \frac{TI}{T1_{\text{tissue}}} \Big) \tag{2.4.5}$$

Eq. 2.4.5 is used for calculation of CBV in leakage areas, while Eq. 2.4.3 is valid outside leakage areas.

2.4.2 Tracer Kinetic Modeling

Dynamic Susceptibility Contrast Imaging (DSC)

Dynamic susceptibility contrast imaging is a $T2^*$-weighted method where the contrast agent bolus is being tracked while it is passing through the vascular system [37, 67, 68]. A paramagnetic contrast agent induces susceptibility differences between intra- and extravascular space, which decreases $T2^*$ in gradient-affected regions around the blood vessels. CBV is calculated from the resulting signal loss and recovery during the passage. The dependence of the change in the transverse relaxation rate $\Delta R2^*$ on the contrast agent concentration is commonly assumed to be linear to

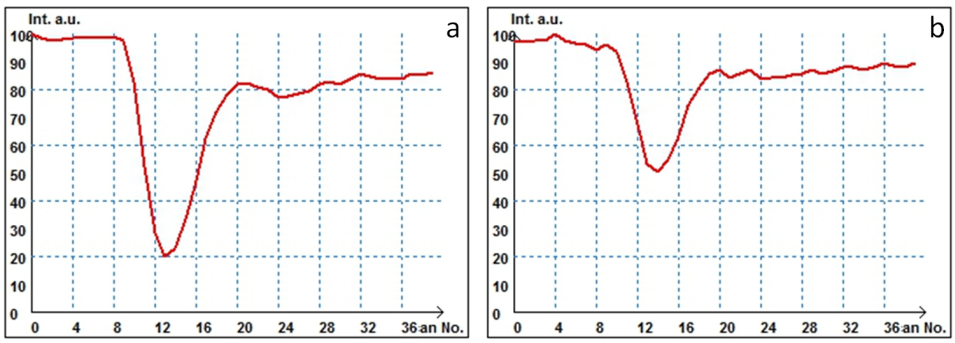

Figure 2.4.2 a) Exemplary AIF obtained from 10 arterial voxels in a DSC series. The second pass is visible at image numbers 24/25. Even after the second pass the baseline of the first images is not reached again because some amount of contrast agent remains in the tissue. b) Signal development in a tissue VOI of the same subject. The signal drop is less prominent and sometimes dispersed compared to a pure blood VOI.

simplify further calculations,

$$\Delta R2^*(t) = r2^* \cdot C(t) \tag{2.4.6}$$

where $r2^*$ is the transverse relaxivity of the contrast agent. The contrast agent concentration $C(t)$ can thus be derived from the signal development during the dynamic series,

$$S(t) = S_0 \cdot \exp\Big(- TE \cdot \big(R2^* + r2^* \cdot C(t)\big)\Big) \tag{2.4.7}$$

CBV is given by

$$\mathrm{CBV} = \frac{H_\mathrm{f}}{\rho} \cdot \frac{\int_0^{\tau_{\text{first pass}}} C_\mathrm{tissue}(\tau)\mathrm{d}\tau}{\int_0^{\tau_{\text{first pass}}} C_\mathrm{art}(\tau)\mathrm{d}\tau} \tag{2.4.8}$$

$H_\mathrm{f} = (1 - \mathrm{Hct_{art}})/(1 - \mathrm{Hct_{cap}})$ is a hematocrit correction factor taking into account the different hematocrits in larger arteries and capillaries. ρ is the density of brain tissue. C_tissue is the concentration time curve of a tissue voxel (Fig. 2.4.2 b); C_art is the concentration time curve of a pure blood voxel supplying the tissue voxel, also called the arterial input function AIF (Fig. 2.4.2 a) [69].
The determination of the AIF usually introduces errors because of partial volume effects [70] and saturation effects in the case of high arterial contrast agent concentrations [71]. An inaccurately or insufficiently sampled AIF prevents the DSC analysis from yielding absolute values for the blood volume, so usually only a relative CBV (rCBV) is reported.

To exclude recirculation effects, a gamma variate function is fitted to the measured C_{tissue} where the measured, incomplete return to baseline after the signal drop is replaced by an assumed full return. rCBV is obtained from the area under the fitted function.

Dynamic Contrast Enhanced Imaging (DCE)

Methods exploiting contrast agent-induced changes of the longitudinal relaxation are termed dynamic contrast-enhanced imaging. Tofts and Kermode provided the foundation for most future work with a two-compartment model allowing for permeability between blood plasma and extravascular extracellular space (EES) [72],

$$C_{\text{tissue}}(t) = v_{\text{plasma}} \cdot C_{\text{plasma}}(t) + K^{\text{trans}} \int_0^t C_{\text{plasma}}(\tau) \exp\Big(- k_{\text{ep}}(t-\tau)\Big) \mathrm{d}\tau \tag{2.4.9}$$

where C_{tissue} and C_{plasma} are contrast agent concentrations in tissue and blood plasma. v_{plasma} is the fractional volumes of plasma in the voxel. The volume transfer constant K^{trans} between plasma and EES and the rate constant k_{ep} between EES and plasma are measures for the permeability of the blood brain barrier.

Assuming low permeability and negligible back-diffusion of contrast agent ($k_{\text{ep}} \rightarrow 0$), the generalized kinetic model in Eq. 2.4.9 can be linearized with the Patlak method [73, 74]. The Patlak plot is a graphical evaluation where the contrast agent concentration in tissue divided by the concentration in plasma is plotted against time (Fig. 2.4.3 a). The intercept represents the plasma volume v_{plasma}:

$$\frac{C_{\text{tissue}}(t)}{C_{\text{plasma}}(t)} = v_{\text{plasma}} + K^{\text{trans}} \cdot \frac{\int_0^t C_{\text{plasma}}(\tau)\mathrm{d}\tau}{C_{\text{plasma}}(t)} \tag{2.4.10}$$

If backflow into plasma cannot be neglected and influx as well as efflux need to be taken into account, the Tofts model can be simplified to yield [75]

$$\begin{aligned} C_{\text{tissue}}(t) = {} & v_{\text{plasma}} \cdot C_{\text{plasma}}(t) \\ & + K^{\text{trans}} \cdot \exp\Big(- \frac{K^{\text{trans}}}{v_{\text{e}}} \cdot t\Big) \cdot \int_0^t C_{\text{plasma}}(\tau) \cdot \exp\Big(\frac{K^{\text{trans}}}{v_{\text{e}}} \cdot \tau\Big) \mathrm{d}\tau \end{aligned} \tag{2.4.11}$$

k_{ep} has been substituted in Eq. 2.4.11 by $K^{\text{trans}}/v_{\text{e}}$, v_{e} being the fractional

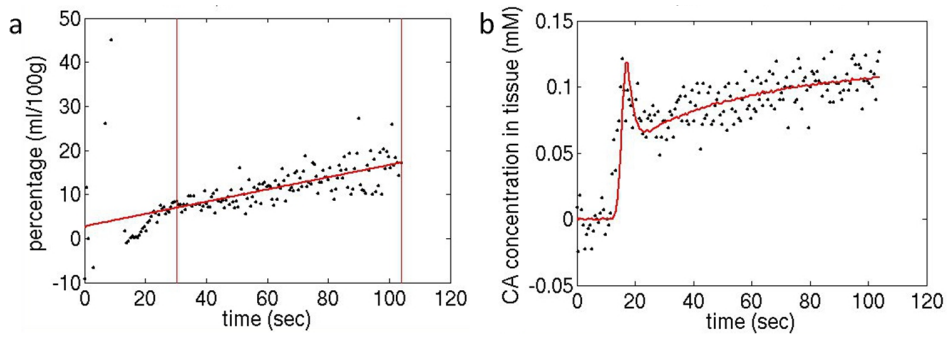

Figure 2.4.3 a) Patlak plot of a single voxel. A straight line is fitted to the data in the range marked by the vertical lines. While the intercept of the fitted line represents the plasma volume, the slope represents K^{trans} ($v_{\text{plasma}} = 2.76\%$, $K^{\text{trans}} = 0.08$ min^{-1} for the shown voxel). b) The modified Tofts model fitted to single-voxel data. Besides v_{plasma} and K^{trans}, v_e is an additional fitting parameter ($v_{\text{plasma}} = 2.79\%$, $v_e = 56.6\%$ and $K^{\text{trans}} = 0.17$ min^{-1}).

volume of EES [76].

While the Patlak model in Eq. 2.4.10 is only valid in areas with low permeability, the modified Tofts model (Fig. 2.4.3 b) in Eq. 2.4.11 is not subject to this restriction.

CBV is obtained from the plasma volume and the hematocrit via CBV $= v_{\text{plasma}}/(1 - \text{Hct})$.

Analogous to the evaluation in DSC, the tracer concentration time curve $C(t)$ is obtained from the measured signal by assuming a linear dependence between the change in the longitudinal relaxation rate $\Delta R1 = 1/\Delta T1$ and the concentration, $r1$ being the relaxivity of the contrast agent,

$$\Delta R1(t) = r1 \cdot C(t) \tag{2.4.12}$$

and by considering the signal development during longitudinal relaxation after magnetization saturation,

$$S(t) = S_0 \cdot \left(1 - \exp\left(-TD \cdot \left(R1 + \Delta R1(t)\right)\right)\right) \tag{2.4.13}$$

where TD is the delay time after saturation. S_0 represents the signal at equilibrium. Solving for the tracer concentration yields

$$C(t) = -\frac{1}{r1 \cdot TD} \ln\left(1 - \frac{S(t)}{S_0}\right) - \frac{1}{r1 \cdot T1} \tag{2.4.14}$$

3 Experimental Details

3.1 Quantification of T2*

3.1.1 Correction of Susceptibility Effects

Local macroscopic magnetic susceptibility differences occur in the brain especially on interfaces of different tissues. They are most noticeable near air filled cavities close to the basal frontal and temporal lobes where they lead to signal loss in $T2^*$-weighted images and a resulting underestimation of $T2^*$.
A correction method has been suggested in literature which uses exponential excitation pulses to maintain a mono-exponential signal decay also in background gradient-affected areas [77]. Correction factors are calculated from the time profile of the excitation pulse $A(t)$, the local background gradient strength G_{susc} and the imaging gradient strength G_{s}. The susceptibility gradient mapG_{susc} in through-plane direction can be calculated from the phase difference $\Delta\phi$ of the first two echo images with a spatial distance Δx between two voxels as

$$G_{\text{susc}} = \frac{\Delta\phi}{\gamma \cdot \Delta x \cdot (TE_2 - TE_1)} \tag{3.1.1}$$

If either phase or real and imaginary data are collected together with the magnitude data, a phase map can be generated easily.
The signal intensity in $T2^*$-weighted multi-gradient echo images is given by

$$S(TE) \propto A\Big(\frac{G_{\text{susc}}}{G_{\text{s}}} \cdot TE\Big) \cdot \exp\Big(-\frac{TE}{T2^*}\Big) \tag{3.1.2}$$

where A is the excitation pulse time profile, G_{s} is the slice-selection gradient strength and G_{susc} is the background gradient which is assumed to be linear and perpendicular to the selected slice [77, 78]. The signal decay is

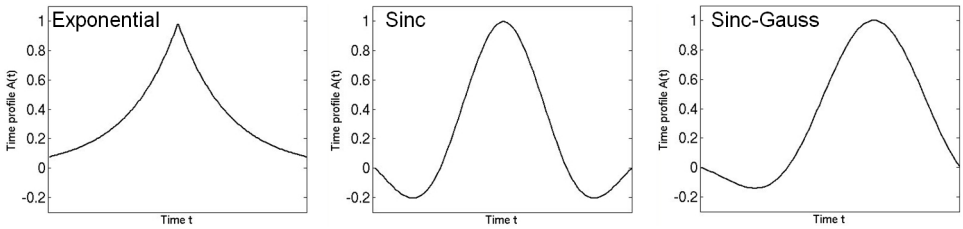

Figure 3.1.1 Graphical representations of the three compared pulse time profiles.

therefore dependent on the pulse shape and can deviate from exponential decay. For known pulse shapes, correction factors $1/A$ can be calculated to account for this deviation. The maximum correctable gradient strength was found with phantom experiments performed in the context of developing a clinical hypoxia imaging protocol [79, 80] and is described in the following.

Three different pulse shapes were explored for their suitability to reconstruct the signal intensity, namely an exponential pulse, a sinc-shaped pulse, and the default pulse on the scanner, which had an optimized sinc-Gauss shape. They were implemented in the sequence code according to Ref. [78] as

$$A_{\text{expo}}(t) = \exp\left(-4\,\frac{|G_{\text{susc}}|}{G_{\text{s}}}\cdot\frac{t}{p/2}\right) \tag{3.1.3}$$

and

$$A_{\text{sinc}}(t) = \text{sinc}\left(2\pi\,\frac{|G_{\text{susc}}|}{G_{\text{s}}}\cdot\frac{t}{p/2}\right)\cdot\cos\left(\frac{\pi}{2}\,\frac{|G_{\text{susc}}|}{G_{\text{s}}}\cdot\frac{t}{p/2}\right) \tag{3.1.4}$$

p is the duration of the pulse. The cosine term is used as a filter to smooth the excitation spectrum. The sinc-Gauss pulse was approximated numerically. A graphical representation of the pulses is given in Fig. 3.1.1.

Magnitude, real and imaginary images of a phantom and four volunteers (3 males, 32.5 ± 15.2 years) were acquired with a 3T Philips Achieva Scanner (Philips, Hamburg, Germany). An 8-channel receive-only head coil and a whole-body transmit coil were used. Multi-gradient echo images with 10 echoes and 40 slices were acquired with TE_1 = 3 ms, ΔTE = 5 ms, TR = 2055 ms, rapid flyback, FOV = 184×132 mm^2, voxel size $2 \times 3 \times 3$ mm^3, a reconstructed matrix of 112×112, and a flip angle of 60°. The total accquisition time was 3 min 5 sec.
The duration of the exponential and sinc pulses was 2.78 ms and 2.11 ms for the sinc-Gauss pulse. The respective slice selection gradient strengths

G_s were 11.274 mT/m (exponential, sinc) and 11.289 mT/m (sinc-Gauss). The phantom was a sphere filled with a gel of 1.75% agar dissolved in a 0.9% sodium chloride solution which had been doped with 0.11 mmol/mL of gadolinium diethylene triamine pentaacetic acid. Susceptibility gradients of a similar strength as in vivo were created by firmly attaching a small metal piece at the bottom of the phantom.
The weighting of the exponentially decaying signal with the time profile of the excitation pulse was removed by correction factors $1/A$ that were calculated according to Eqs. 3.1.3 and 3.1.4 and with the numerical approximation of the sinc-Gauss pulse. Corrected data were then fitted mono-exponentially in Matlab [136]. Results of the phantom and volunteer studies are presented in Section 4.1. Relevant conclusions for the hypoxia study regarding the limits of the susceptibility gradient correction are drawn in Section 5.1.

3.1.2 Motion Correction

Since a large fraction of the patients included in the hypoxia study were elderly and often critically ill (suspected brain tumors or suspected stroke), subject motion influenced most of the data to varying extent. Without any measures to take care of motion effects, several data sets containing valuable information would have had to be discarded.
If the subject moves between single scans, the images can be coregistered retrospectively. Coregistration was performed by default for each subject with the respective routine of SPM8 [137]. Intrascan motion leading to artifacts in single volumes is more difficult to handle. In the following, a motion correction method suitable for sparse motion expressing itself as wavelike intensity variations in $T2^*$ maps is explained [81]. Since such artifacts severely degrade the quality of oxygenation-related maps up to the point of making them useless, the correction method was included in the hypoxia data evaluation program.

The correction method is based on repeating the multi-gradient echo acquisition for $T2^*$ mapping with lower spatial resolution in phase encoding direction. Since images are most affected by motion if central lines of k-space are corrupted, it is sufficient to resample the central half of k-space.
Imagine a combined data set F_C in k-space where each k-space line is represented as a weighted average of the lines in the original data sets F and

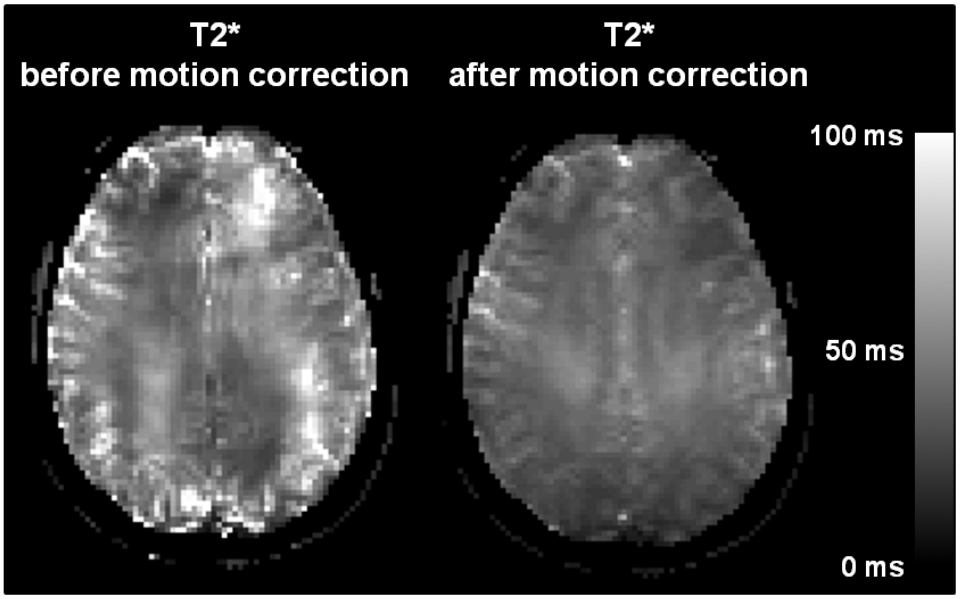

Figure 3.1.2 Example of a healthy volunteer with motion artifacts. *Left:* Gradient corrected but not motion corrected $T2^*$ map. Typical wavelike intensity variations are visible. *Right:* Gradient and motion corrected $T2^*$ map. Intensity variations have been eliminated almost completely by the correction routine and the map is much more homogeneous.

F_L (F_L being the low resolution data set),

$$F_\mathrm{C}(k_x, k_y, TE) = w(k_y) \cdot F(k_x, k_y, TE) + \big(1 - w(k_y)\big) \cdot F_\mathrm{L}(k_x, k_y, TE) \quad (3.1.5)$$

In the case of sparse motion affecting single k-space lines in one of the two acquisitions, corrupted k-space lines in either data set can be suppressed with suitable weighting factors $w(k_y)$. Continuous motion or strong motion artifacts affecting the same k-space lines in both acquisitions cannot be corrected.

The challenge is now to find the correct weighting factors. If a multi-gradient echo sequence with a long repetition time is used ($TR \sim 3$ sec), sparse subject motion affects only the lines in k-space that are acquired during motion. The image is then the sum of the Fourier transforms of the unaffected data $F(k_x, k_y, TE)$ and an error signal $\Delta F(k_y, TE)$. As a result, local constructive or destructive interferences depending on TE occur in image space. The signal does not decay exponentially anymore, and an exponential fit will lead to bad correlation and locally incorrect $T2^*$ values. The effect is therefore similar to that of susceptibility gradients that also produce a deviation from exponential decay (except when exponential excitation pulses are used). However, background gradients do not

interfere with the motion correction because they are present in both data sets and do not lead to correlation differences between the two sets. Also, they reduce the correlation coefficients much less than motion.
The correlation behavior of acquired and fitted signal intensity decay can be used to find image voxels whose echo signal intensities are influenced by motion, and to determine the correct weighting factor $w(k_y)$ for each k-space line: If an exponential fit is performed voxelwise and fitted intensities are calculated from the results of the fit, the correlation of acquired and fitted intensities can be determined for each voxel. Voxels influenced by motion can be identified by their lower correlation coefficient values.
To create a second, full resolution data set from the half resolution acquisition, the central part of the full resolution k-space data set is replaced with data from the half resolution acquisition. Out of these two image data sets, a hybrid target data set is constructed which for each voxel uses the value from the data set with the greater correlation coefficient. The target data set is converted into a k-space data set F_{target} by performing an inverse Fourier transform. F_{target} approximates the combined data set $F_{\text{C}}(k_x, k_y, TE)$ in Eq. 3.1.5 via minimizing

$$\sum_{k_x,TE} \Big(F_{\text{target}} - F_{\text{C}} \Big)^2 = \sum_{k_x,TE} \Big(F_{\text{target}} - w(k_y) \cdot F - \big(1 - w(k_y)\big) \cdot F_{\text{L}} \Big)^2 \quad (3.1.6)$$

The weighting factors can therefore be calculated as

$$w(k_y) = \frac{-\sum \text{Re}\big((F_{\text{L}} - F) \cdot (F_{\text{target}} - F_{\text{L}})^*\big)}{\sum (F_{\text{L}} - F)^2} \quad (3.1.7)$$

where the asterisk denotes the complex conjugate. Eq. 3.1.7 is used to determine the weighting factors for each line in k-space which are then used in Eq. 3.1.5 to calculate the combined data set F_{C} in k-space where corrupted lines are suppressed. A Fourier transform of F_{C} yields a combined data set in image space which can be fitted exponentially to produce the $T2^*$ map.
It is advisable to always perform the correction on availability of half resolution data, even if motion artifacts are not visible. In this case the weighting factors are approximately 0.5 for all central k-space lines, and both data sets are simply averaged, with a resulting increase of SNR.
An example of the correction is shown in Fig. 3.1.2. Motion artifacts have vanished almost completely in the corrected $T2^*$ map.

3.1.3 Optimized Imaging Protocol and Post-Processing

To enable both susceptibility gradient and motion correction, a multi-gradient echo acquisition was used for $T2^*$ mapping on the 3T Philips Achieva whole-body scanner using an 8-channel phased-array head coil (receive-only) and a whole-body transmit coil (Philips, Hamburg, Germany). 30 slices with a spatial resolution of $2 \times 2 \times 3$ mm^3 and a slice gap of 0.3 mm were acquired for tumor patients and healthy controls. 20 slices were acquired for the stroke patients to reduce acquisition time. The acquisition matrix size was 112×92. 12 echoes (TE_1 = 6 ms, ΔTE = 5 ms) were sampled under the same gradient polarity to prevent spatial misregistrations in areas with field inhomogeneities [82] with TR = 1950 ms and a flip angle of 30° (although being suboptimal for SNR, smaller flip angles improve the gradient correction [78]). Acquisition time was 3 min 2 sec (2 min 3 sec for the stroke patients). An excitation pulse with an exponential time profile was used. Complex data were exported. The sequence was repeated with half spatial resolution (matrix size 112×46, acquisition time 1 min 32 sec, 64 sec for the stroke patients).
Differing imaging parameters on the 3T Siemens mMR Biograph scanner with a 32-channel head coil for reception and a whole-body coil for transmission (Siemens, Erlangen, Germany) were TE_1 = 5 ms, matrix size 128×128 (full resolution scan), 128×64 (half resolution scan), acquisition time 4 min 11 sec (full resolution scan), 2 min 6 sec (half resolution scan).

To avoid artifacts due to interscan motion between full and half resolution scans, both data sets were coregistered before performing motion correction in k-space. Motion correction was performed before background gradient correction. Calculations were done with custom programs in Matlab [136].

3.2 Quantification of T2

3.2.1 Assessment of Errors in Fast T2 Quantification

The wide range of published values from 55.8 ms in frontal white matter [83] to 120 ms in gray matter [84] hints at the difficulties in accurate $T2$ quantification and the existence of several confounding factors. The $T2$ mapping sequence for the hypoxia study protocol needs to be fast while at the same time providing acquisition of high resolution images that enable an accurate determination of $T2$. Although GRASE is the natural choice to meet these demands since a CPMG excitation and refocusing scheme is easily implemented and the EPI readout guarantees fast sam-

pling of k-space, a number of smaller simulations and validation tests were performed to verify the superiority of $T2$ mapping with GRASE over the available alternatives of TSE and single spin echo imaging. TSE, also featuring a CPMG scheme, is expected to perform equally well in terms of $T2$ accuracy but in a longer execution time as it does not include an EPI readout. Effects from RF pulse imperfections cannot accumulate when single spin echoes are used but then on the other hand the advantage of suppressing diffusion effects by means of multiple refocusing pulses after each excitation does not apply either. Consequently, shorter apparent $T2$ values are expected. Apart from that, single spin echo imaging is also too time-consuming to be a real alternative for GRASE.

Imperfect refocusing pulses and stimulated echoes. One possible error source in multi-spin echo imaging are stimulated echoes which occur if imperfect 180° refocusing pulses are used for $T2$ quantification, resulting in artificially increased echo signals. Imperfect slice profiles have the same effect as they cause a variation of the flip angle over the slice and thus over each voxel. This happens because longitudinal magnetization is created if the transverse magnetization is not flipped back completely onto the transverse plane by an 180° pulse. At a later point this longitudinal magnetization is converted into transverse magnetization by an RF pulse and can contribute to echo signals.
A formal description of this phenomenon, the extended phase graph (EPG) algorithm, has been introduced in Ref. [85] where the phase state configuration of the magnetization is represented by a vector

$$\boldsymbol{F}_k(n) = (F_0 Z_0 F_1 F_{-1} Z_1 F_2 F_{-2} Z_2 \dots F_k F_{-k} Z_k)^{\mathrm{T}}(n)$$

with F corresponding to transverse magnetization configurations and Z to longitudinal magnetization configurations. n is the number of preceding RF pulses, k is the configuration order and T denotes the transpose. Application of RF pulses with an angle α, time evolution and relaxation are described by the transition matrices $\boldsymbol{T}(k, \alpha_n)$, $\boldsymbol{S}(\Delta TE/2)$ and $\boldsymbol{R}(\Delta TE/2)$, enabling the calculation of magnetization configurations and echo signal intensities after any number of RF pulses. $\boldsymbol{T}(k, \alpha_n)$ mixes states with the same k, $\boldsymbol{S}(\Delta TE/2)$ shifts F_k to F_{k+1} but does not shift Z_k (corresponding to the dephasing and rephasing of transverse magnetization but no change in the phase state of longitudinal magnetization) and $\boldsymbol{R}(\Delta TE/2)$ results in an exponential decay of the magnetization governed by $T2$ and $T1$. Only coherent transverse magnetization denoted by F_0 is responsible for the echo signal. The calculation of flip angles to produce specific signal intensities

is likewise possible [86].

GRASE is especially designed to avoid the accumulation of stimulated echo effects over an acquired time series by introducing a phase difference of 90° between excitation and refocusing pulses (see Section 2.3). Simulations were performed to estimate the accuracy of $T2$ quantification with GRASE as used in the hypoxia protocol. Signal intensities of a CPMG sequence with 8 echoes, $\Delta TE = 16$ ms, and a fixed $T1 = 1200$ ms, were calculated using the EPG formalism for $T2 = 70$ ms and assumed deviations from perfect 180° refocusing pulses of 30% and 5%. Since odd echoes are formed in a plane that is tilted against the transverse plane and thus produce lower signals, only the four even echoes intensities calculated with the EPG algorithm were fitted mono-exponentially to test if stimulated echoes are successfully suppressed and the set $T2$ of 70 ms can be reproduced.
To find out the deviation from 180° in the GRASE sequence, two experiments with a homogeneous phantom were performed. The first experiment was done with the unchanged sequence, where all RF pulses have a nominal angle of 180°. In the second experiment, refocusing control was switched off in the protocol, resulting in the use of a single 180° pulse and subsequent 150° pulses. Signal intensities calculated with the EPG formalism were fitted to all echo signal intensities of the measured data, with $T2$ and the refocusing angle as fitting parameters.

Diffusion. As described in the paragraph on DWI in Section 2.3, the signal development including diffusion is given by

$$S(t) = S_0 \cdot \exp\Big(-\frac{t}{T2}\Big) \cdot \exp\Big(-\frac{\gamma^2 G^2 D t^3}{12 n^2}\Big) \tag{3.2.1}$$

The more 180° pulses are applied (denoted by n), the more the mean square phase dispersion is reduced [62]. The influence on the signal of the factor accounting for diffusion in Eq. 3.2.1 decreases very fast with an increasing number of pulses due to the exponential dependence on $1/n^2$. It increases even faster for increasing echo times (exponential dependence on t^3) but the maximum TE cannot be chosen too small in order to sample a sufficiently large part of the $T2$ decay curve. The influence of diffusion on $T2$ quantification was tested by comparing the results from single spin echo measurements to those from GRASE measurements.

A single spin echo $T2$ mapping protocol was assembled containing 9 separate acquisitions where excitation and 180° refocusing precede each acquisition ($TE_1 = 40$ ms, $\Delta TE = 20$ ms, $TR = 2000$ ms). The $T2$ decay was sampled up to a maximum echo time of 200 ms. Since this is a very

time-consuming process to quantify $T2$, a reduced resolution of $3.5 \times 4 \times 3$ mm^3 was chosen, resulting in a total acquisition time of 16 min 40 sec for 5 slices. A GRASE sequence with the hypoxia study parameters ($TE_1 = 16$ ms, $\Delta TE = 16$ ms) samples the $T2$ decay up to 128 ms ($TR = 8547$ ms, resolution $2 \times 2 \times 3$ mm^3, 30 slices in 2 min 17 sec). Additionally, a TSE sequence was tested with the same parameters as in GRASE (acquisition time 13 min 49 sec).
Measurements were performed on a homogeneous phantom and on an agar gel phantom containing several flasks with different gel compositions as well as a flask filled with vegetable oil. Thus, homogeneous areas with 9 different $T2$ values in the range between $\sim$ 30 ms and $\sim$ 110 ms could be analyzed. Additionally, 8 volunteers were measured (5 males, 24.9 ± 6.3 years). All echoes from the single spin echo measurements were fitted mono-exponentially, disregarding the diffusion factor in Eq. 3.2.1. Four even echoes were fitted for the GRASE and TSE data. Only the five corresponding slices were evaluated for the comparison of single spin echo with the other methods.

3.2.2 Imaging Protocol and Post-Processing

For the hypoxia study protocol, a GRASE sequence with CPMG excitation and refocusing was used for $T2$ mapping on the 3T Philips Achieva scanner with a TSE factor of 8 and an EPI factor of 7. Spin echoes encoded the echo images, gradient echoes were used to encode the k-space lines in each spin echo image. 30 slices with a spatial resolution of $2 \times 2 \times 3$ mm^3 and a slice gap of 0.3 mm were acquired for tumor patients and healthy controls. 20 slices were acquired for the stroke patients. The matrix size was 112×91. 8 echoes (TE_1 = 16 ms, ΔTE = 16 ms) were sampled with TR = 8547 ms and a flip angle of 90°. Acquisition time was 2 min 17 sec (1 min 31 sec for the stroke patients).
Since the source code of GRASE was not available for the 3T Siemens mMR Biograph scanner, the TSE sequence code (CPMG, Turbo factor 1, GRAPPA factor 2) was modified to enable the acquisition of 8 echoes with $TR = 4040$ ms, matrix size 128×128 in an acquisition time of 5 min 13 sec.
Only the four even echoes were fitted to reduce effects from imperfect RF pulses.

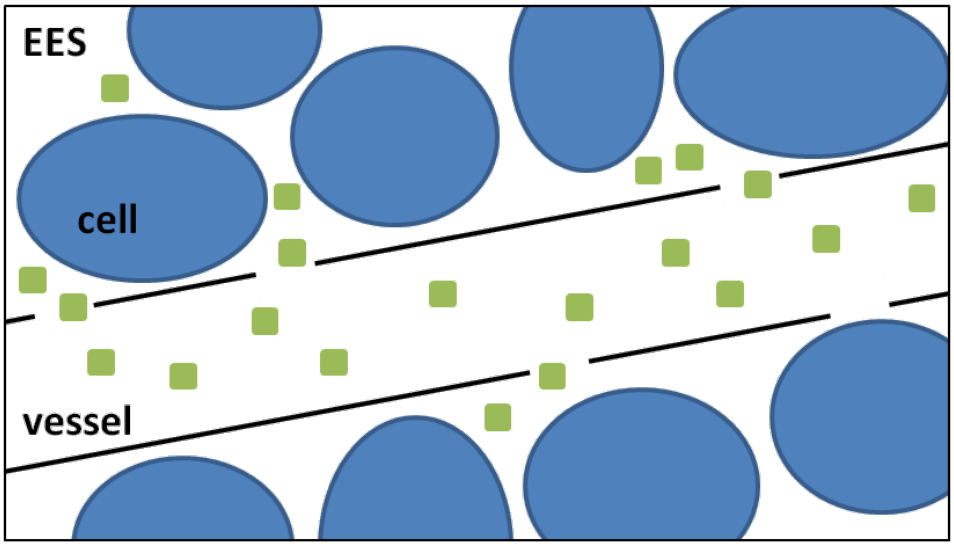

Figure 3.3.1 Schematic 2D voxel containing a leaky vessel. Contrast agent molecules (green) are passing through the blood vessel. Because of a pathologically permeable blood brain barrier they do not remain intravascular but can enter the extravascular extracellular space (EES) where they accumulate. Cell membranes remain impermeable for contrast agent molecules.

3.3 Addressing Contrast Agent Leakage in the Quantification of the Cerebral Blood Volume

Contrast agents with low molecular weight like Gadolinium-DTPA diffuse from the bloodstream into extravascular space between the brain cells if the natural barrier between the blood vessel system and the brain parenchyma becomes leaky. The amount of diffusing molecules depends on the blood flow, the permeability and the surface area of the blood vessels. Some diseases like high-grade brain tumors or inflammation disorders destroy the blood brain barrier. Neoplastic processes in high-grade gliomas for example frequently destroy capillaries or cause the formation of new but pathological vessels [87]. Contrast agent molecules can leave the vasculature in those areas and enter the extravascular extracellular space (EES) where their presence alters the local relaxation behavior (Fig. 3.3.1).

The blood brain barrier can be expected to be dysfunctional in high-grade gliomas and metastases. Patients with suspected brain tumors and metastases are therefore a suitable population to explore the influence of contrast agent leakage and the quality of correction methods. In order to select the best method for the hypoxia study, 56 patients (32 males, 59 ± 16

years) were examined with three different methods for CBV quantification, VASO, DSC and DCE.
Since VASO and DCE measurements had to be performed in addition to the normal clinical examination protocol (whereas a DSC scan is routinely included in the clinical protocol), time restrictions made it impossible to perform all three methods in all patients. Patients were therefore split up into two separate groups. The first group ($n = 35$, 20 males, 47 ± 14 years, 54% with high-grade gliomas, i. e. grade III astrocytomas or grade IV glioblastomas) received VASO and DSC measurements. The pre-contrast VASO image was acquired before contrast agent application, during and after which the DSC and post-contrast VASO images were acquired.
The second group ($n = 21$, 12 males, 63 ± 18 years, high-grade glioma fraction of 43%) received DCE and DSC measurements after contrast agent application. The reduced contrast agent dose for DCE served as a prebolus in the DSC measurement.

3.3.1 Identification of Leakage Areas

Since leakage areas need to be determined for both the VASO and DCE methods, the post-contrast MPRAGE image was used as an independent source to find enhancing voxels. To this end gray and white matter probability maps were created by segmentation of the MPRAGE images with SPM8 [137]. Gray and white matter masks were produced by thresholding the probability maps at $P_{\mathrm{WM/GM}} < 0.75$. An intensity histogram of the white matter part of the MPRAGE image was generated, to which a Gaussian distribution was fitted. The intensity value in the histogram corresponding to the mean$+2.576\sigma$ of the normal distribution was selected to threshold the MPRRAGE data. Areas with a lower signal intensity (99.5% of all white matter intensity values) were assumed to belong to healthy tissue while higher signal intensities in the MPRAGE were assumed to represent pathological, contrast agent enhancing areas (see Fig. 3.3.2). The selection process was implemented in Matlab [136] and performed for each patient individually.

3.3.2 Extended Vascular Space Occupancy Imaging

Imaging protocol. VASO was performed on the Achieva scanner using a multi-slice TFE-EPI sequence with an EPI factor of 7, a TFE factor of 1, $TE = 4.7$ ms, $TR = 10$ ms and a flip angle of $\alpha = 25°$. The voxel size was $2 \times 2 \times 3$ mm^3, the matrix size was 112×108. 30 slices were acquired. To null the blood signal at a defined time, a shared non-selective inversion

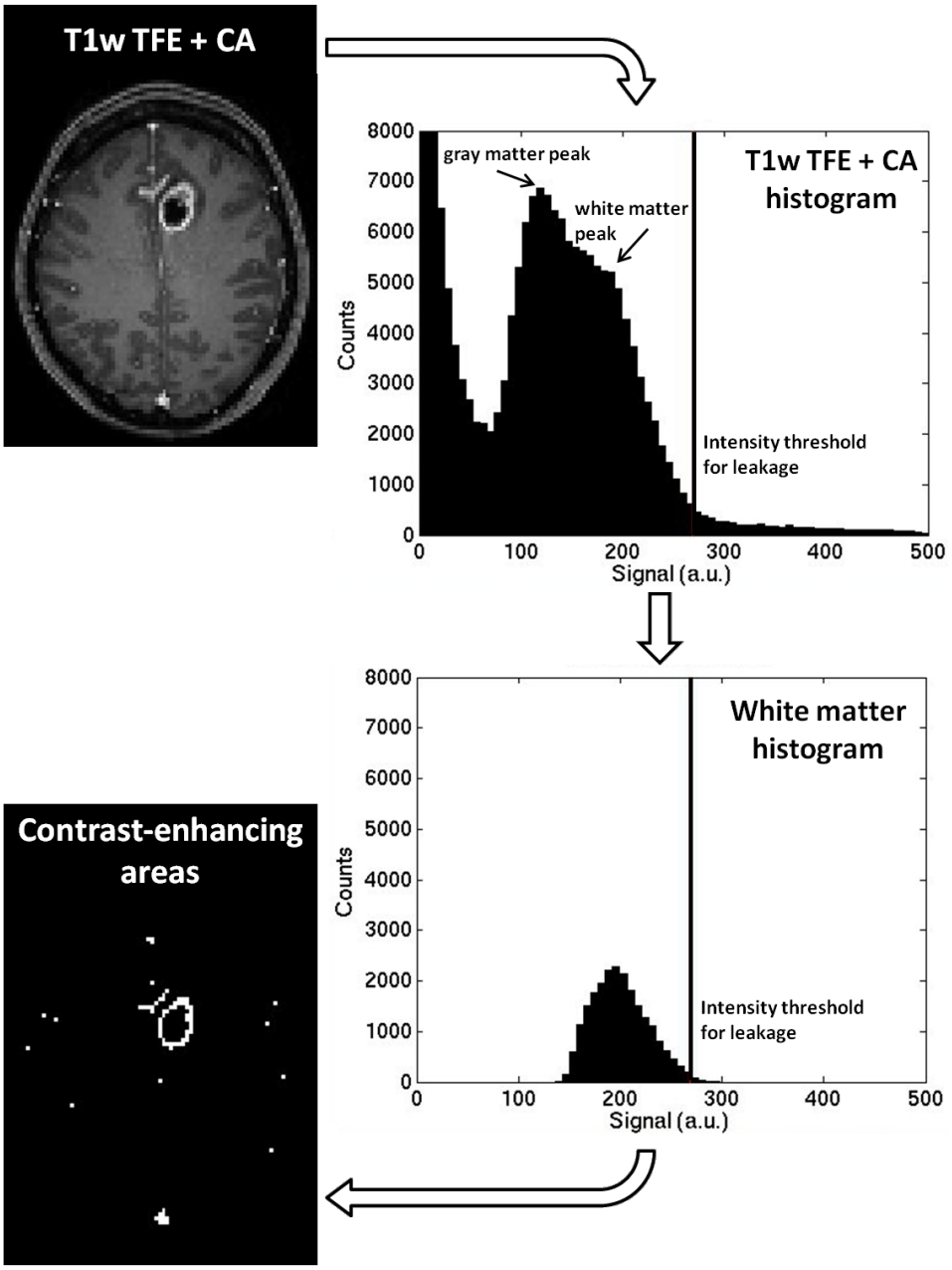

Figure 3.3.2 Determination of leakage areas. The MPRAGE histogram possesses two more or less pronounced peaks, one at lower signal intensities representing healthy gray matter and one at higher intensities representing healthy white matter, as well as a tail at high intensities representing the enhancing areas. The threshold to isolate the enhancing areas was determined for each patient individually with the help of the white matter histogram. Also shown is a single slice of the post-contrast MPRAGE volume and the corresponding mask of enhancing areas.

prepulse was used with an inversion time $TI = 1085$ ms. The acquisition time was 35 sec for each of the two volumes.

Post-processing. Spatial coregistration was performed for the pre- and post-contrast volumes. The water proton density of blood C_{blood} was set to 0.87, the density of tissue C_{par} was set to 0.75 [88]. $T1_{\text{tissue}}$ was set to 1300 ms for the whole brain. CBV maps were calculated according to Eq. 2.4.3. Contrast agent leakage was accounted for by using Eq. 2.4.5 in leakage areas defined as described in Section 3.3.1, assuming a leakage volume fraction of 0.22 which is a literature value for EES in glioma [89]. CBV maps were smoothed.

3.3.3 Dynamic Susceptibility Contrast Imaging with Prebolus

DSC evaluation models normally assume negligible $T1$ effects in tissue compared to $T2^*$ effects, which is violated in the case of contrast agent leakage when $T1$ is shortened in the tissue around blood vessels. The signal drop in $T2^*$-weighted images is diminshed by this effect, resulting in an underestimation of CBV. There are different methods to account for $T1$ effects in DSC: in image acquisition (e.g. double echo acquisition [90]), by the use of a prebolus [91], or in the post-processing (e.g. leakage models [92] or gamma variate fitting [93]). A pre-dose of contrast agent minimizes changes of $T1$ caused by extravasation during the second, main bolus [94] by pre-saturating the surrounding tissue with contrast agent and thus adjusting the baseline during the DSC acquisition. Since the prebolus method does not affect the standard clinical perfusion protocol that patients need to undergo anyway, and because it is also compatible with the commercial program used to evaluate the data, the prebolus technique was chosen for the CBV study. Besides $T1$ effects, $T2^*$ effects can also occur if the contrast agent produces susceptibility gradients in the tissue part of the voxel. A combination of both effects is likewise possible depending on the extravascular tissue structure within the tumor [95]. The prebolus technique accounts only for $T1$ effects.

Imaging protocol. The standard clinical perfusion sequence on the 3T Philips Achieva scanner uses a single-shot gradient echo EPI readout for 40 dynamics with a SENSE factor of 2, TE = 40 ms, TR = 1.7 sec and a flip angle α of 75°. The resolution was $2.33 \times 2.33 \times 4$ mm^3 with a matrix size of 96×95. 25 slices were acquired using a 15 mL bolus of Gd-DTPA. The prebolus consisted of 7.5 mL Gd-DTPA (applied during the DCE acquisition).
Deviating parameters on the 3T Siemens mMR Biograph were: Matrix

128×128, GRAPPA with acceleration factor 2, TE = 30 ms, TR = 1.5 sec, $\alpha = 90°$, resolution $1.8 \times 1.8 \times 4$ mm^3, 20 slices.

Post-processing. The commercial program Stroketool [138] was used for evaluation of DSC data. The program includes a motion correction routine that was applied if displacements between volumes acquired at different time steps were noticeable. Since Stroketool output maps of different patients are not uniform in scale, for each patient patient a small volume of interest with rather low CBV in healthy appearing white matter contralateral to the tumor or the stroke-affected area was set to 1.5%. CBV maps were then scaled accordingly, yielding relative CBV (rCBV) maps. The normalization value was chosen to generate a typical CBV value of approximately 3% in white matter in all patients. Since white matter differences between patients are equalized in this way, normalization to an anatomical structure would in principle be preferable but is infeasible because a tumor can occur anywhere in a large patient population.
Apart from rCBV maps, time to peak (TTP) maps were calculated for stroke patients. TTP is defined as the time from the beginning of the signal drop to the time when the signal in the respective voxel assumes its lowest value. It is a measure of how fast the contrast agent bolus passes through the voxel and allows for a diagnostic evaluation of delayed perfusion in ischemic diseases.

3.3.4 Dynamic Contrast Enhanced Imaging with Model Selection

T1 Mapping

Imaging protocol. Since $T1$ enters Eq. 2.4.14, $T1$ mapping needs to be performed for evaluating DCE data. On the Achieva scanner, a TFE-EPI sequence with EPI factor 5, TFE factor 1 and SENSE factor 2 was used for this purpose. TE (the time from excitation to center of k-space acquisition during the EPI readout) was 2.9 ms, TR was 6.4 ms (defined by Philips as the time between two subsequent excitation pulses for different slices), the flip angle α was 30°. 15 slices with a scan duration of 514 ms per slice (without TD) were acquired with a voxel size of $3 \times 3 \times 8$ mm^3 and a matrix size of 76×54. A shared TFE prepulse was used for saturation. Native images were acquired at 13 time points with delay times TD between 100 ms and 7100 ms after saturation. The delay is the interval between the saturation and the beginning of the EPI readout. The total acquisition time was several minutes.
A TFE sequence without EPI was available on the mMR Biograph. Devi-

ating parameters were a GRAPPA acceleration factor of 2 with 21 reference lines, $TE = 1.2$ ms, $TR = 149$ ms for the shortest delay (defined by Siemens as the acquisition time for one slice including TD, i.e. the time between two saturation pulses). The repetition time between two subsequent RF pulses for the same slice was 2.9 ms. The voxel size was $3.1 \times 3.1 \times 8$ mm^3 and the matrix was 64×64 with phase partial Fourier of 6/8. 8 time points between 100 ms and 3000 ms after saturation were selected for acquisition with a duration of 2 min 35 sec. The delay is counted from the saturation to the center of k-space acquisition.

Post-processing. Since the time interval TD between saturation and image acquisition in Eq. 2.4.14 is different for each slice on the Achieva scanner (because the inner loop is the slice loop and the outer loop is the phase loop, resulting in a time shift of 6.4 ms between all voxels of two adjacent slices), the actual TD needs to be calculated for each slice separately considering the interleaved slice scan order (slice 1, 3, 5, ..., 2, 4, 6). This is equally true for the DCE evaluation. An effective TD defined as the time between saturation and center of k-space acquisition was used for the Biograph data where the loop order is the other way around.
A saturation recovery curve was fitted to the time series to obtain the $T1$ map.

DCE Acquisition

Imaging protocol. A Gd-DTPA bolus of 7.5 mL was used for DCE imaging. The $T1$ mapping protocol with a fixed TD of 120 ms after saturation for each of the 180 images was used for acquisition. A temporal resolution of 0.577 sec was achieved. The acquisition time was 1 min 44 sec.
Deviating parameters on the mMR Biograph were $TD = 100$ ms, 90 images with a temporal resolution of 2.2 sec. The acquisition time was 3 min 21 sec.

Post-processing. If necessary, the coregistration and realignment routine of SPM8 [137] were used to spatially coregister $T1$ and DCE data. The signal in equilibrium S_0 in Eq. 2.4.14 was obtained from the baseline signal in the DCE data before contrast agent administration. 4 arterial voxels were selected for each patient to generate the AIF. $1/T1 = 4$ sec^{-1} was assumed for Gd-DTPA [96], corresponding to a 0.5 mmol/mL concentration of Gd-DTPA. The hematocrit was set to Hct = 0.41 [97]. The Patlak model in Eq. 2.4.10 was used to calculate CBV maps. The MPRAGE image was coregistered to the $T1$ map and leakage areas were determined. CBV was recalculated in leakage voxels with the modified Tofts model in Eq. 2.4.11.

CBV maps were smoothed in-plane only, due to the large slice thickness of 8 mm.

A volume of interest (VOI) analysis was performed with VINCI [139] for all created CBV maps from VASO, DSC and DCE acquisitions. Gray and white matter VOIs were selected within the respective gray and white matter segments where $P_{\mathrm{GM/WM}} > 0.75$. Pathological tissue in the FLAIR or MPRAGE images was excluded. Contrast-enhancing tissue VOIs within tumorous tissue were defined in the MPRAGE volumes.

3.4 Calculation of the Oxygen Extraction Fraction

The complete hypoxia imaging protocol consisting of the described protocols for $T2^*$, $T2$ and CBV mapping took 7.5 min on the 3T Philips Achieva for patients with suspected brain tumors ($n = 55$, 28 males, 57.7 ± 16.7 years) and 4.5 min for patients with stroke or severe carotid artery stenosis ($n = 13$, 7 males, 71.5 ± 11.9 years). Patients additionally received routine clinical imaging (FLAIR, T2*w FFE, MPRAGE after contrast agent application (tumor patients only), DWI (stroke patients only)).
$T2$ and $T2^*$ measurements as well as FLAIR and MPRAGE without contrast agent were performed also on eight healthy volunteers (5 males, 24.9 ± 6.3 years) for comparison.
All patients and volunteers gave written informed consent.

$T2^*$ and $T2$ maps were calculated and corrected as described in Sections 3.1 and 3.2. $R2'$ was calculated from $T2^*$ and $T2$ according to Eq. 2.1.12. Since only DSC was found to be robust enough for patient measurements of CBV (see Section 5.3 for reasons), and since DSC is able to quantify CBV only relatively (see Section 4.3), relative CBV (rCBV) maps were used to yield relative OEF (rOEF) maps using Eq. 2.1.13. This implies a constant ratio of deoxygenated CBV and total CBV across the brain, which is justified by the lack of contrary evidence in a study that yielded a ROI-based ratio of venous CBV/total CBV $= 0.77$ in healthy humans [98].
Other parameter values were the gyromagnetic ratio $\gamma = 2.675 \cdot 10^8$ 1/(sec·T), the main magnetic field $B_0 = 3$ T, the susceptibility difference between fully deoxygenated and fully oxygenated red blood cells $\Delta\chi_0 = 0.264 \cdot 10^{-6}$ [39, 40], and a small-vessel hematocrit Hct $= 0.35$ [97].

Coregistration of all data to the first echo image of the GRASE series as well as gray and white matter segmentation based on MPRAGE data were performed with SPM8 [137]. Voxelwise calculation of all maps was performed with custom programs written in Matlab [136]. VOIs in different tissues were selected and evaluated with VINCI [139]. VOI values were

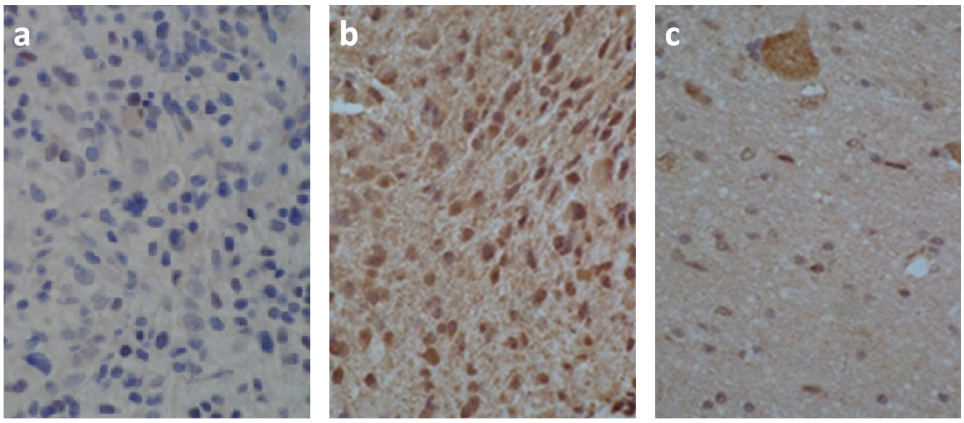

Figure 3.5.1 HIF1α staining examples. a) Sample from solid tumor tissue where closely packed tumor cells showing blue color. HIF1α is not expressed in these cells. b) Sample from solid tumor tissue where expressed HIF1α results in a brown color of the staining substance. This sample is hypoxic. c) Biopsy sample from the outer tumor region just outside the enhancing area. Cells are less dense; some express the hypoxia marker (brown), some do not (blue).

averaged separately over each population (healthy volunteers, tumor patients, stroke patients) and respective standard deviations were calculated.

3.5 Immunohistochemical Methods for Independent Validation

A small validation study was performed in selected patients of the tumor population where 25 targeted biopsy samples in MR-normoxic and MR-hypoxic areas were obtained during tumor resection surgery of six glioma patients [99]. The samples were tested with immunohistochemical methods for expression of the hypoxia-inducible factor HIF1α in the cells (Fig. 3.5.1).
A tumor VOI was assumed to be hypoxic if rOEF in this VOI was greater than $\text{rOEF}_{\text{mean}}+$ standard deviation (rOEF). $\text{rOEF}_{\text{mean}}$ is the mean rOEF of the whole tumor VOI including contrast-enhancing tissue, non-enhancing tumor-like tissue and edema.
The biopsy targets for histological analysis were defined with the cranial planning software of BRAINLAB [140] within the resectable tumor in MR-normoxic and MR-hypoxic VOIs. Cylindrical tissue samples of $1-4$ mm diameter were biopsied with the stereotactic cranial navigation application of BRAINLAB [141] and paraffin-embedded $2-6$ hours later. Immunohistochemical staining of HIF1α was performed, yielding information about

the presence of tumor cells, necrosis, vascularity and a score of HIF1α positivity reflecting a combination of staining intensity and fraction of stained cells in the field of view.

4 Results

4.1 Susceptibility Correction in T2* Maps

The following results have been published in similar form in Ref. [79]. Some preliminary results have been presented in Ref. [80].

The scope of $T2^*$ susceptibility correction. Fig. 4.1.1 shows how $T2^*$ values in a cuboid volume of interest in a homogeneous gel phantom drop with increasing background gradient strength. The shown VOI was selected close to a small metal piece such that a large range of gradient strengths occurred across several slices. Uncorrected $T2^*$ values are decreased to 80% of their original values at 75 μT/m for sinc excitation pulses, at 63 μT/m for sinc-Gauss pulses, and at 34 μT/m for exponential pulses. When the susceptibility gradient correction is used, the respective gradient strengths are extended to 175 μT/m (sinc), 100 μT/m (sinc-Gauss), and even up to 220 μT/m for exponential pulses. For larger gradients corrected values are scattered too widely and are thus unreliable.

The performances of the three tested excitation pulse shapes are compared in Fig. 4.1.2. The exponential pulse amplifies susceptibility effects in the uncorrected $T2^*$ map of the phantom compared to the other two pulses. However, when corrected for background gradients, the map belonging to the exponential pulse appears quite homogeneous even at gradient strengths when the corrections using sinc or sinc-Gauss pulses do not work anymore. On the other hand, sinc-shaped pulses produce a more rectangular slice profile, whereas the slice profile of exponential pulses is Lorentzian. Therefore, if only weak background gradients are present and the correction still works for all pulses, sinc-shaped pulses are the better choice. If exponential pulses are used to handle stronger gradients, it is important to choose a sufficient slice gap. Additionally, the interleaved acquisition mode should be chosen in the measurement protocol.

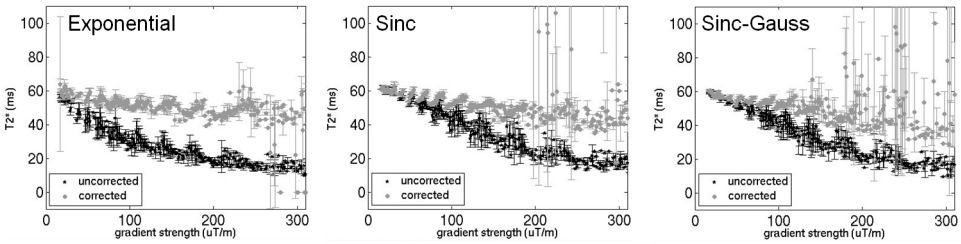

Figure 4.1.1 $T2^*$ dependence on the susceptibility gradient strength in a homogeneous phantom for each tested pulse profile. The error bars represent the standard deviation of $T2^*$ measured in voxels with the same gradient strength.

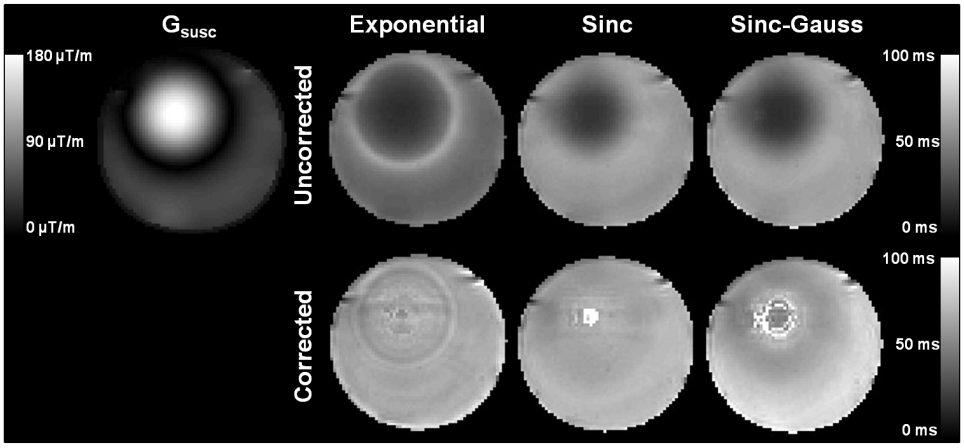

Figure 4.1.2 Susceptibility gradient map of a homogeneous phantom with a small metal piece attached to it, together with uncorrected and corrected $T2^*$ maps of a single slice. The correction results are shown for an exponential, a sinc and a sinc-Gauss shaped excitation pulse.

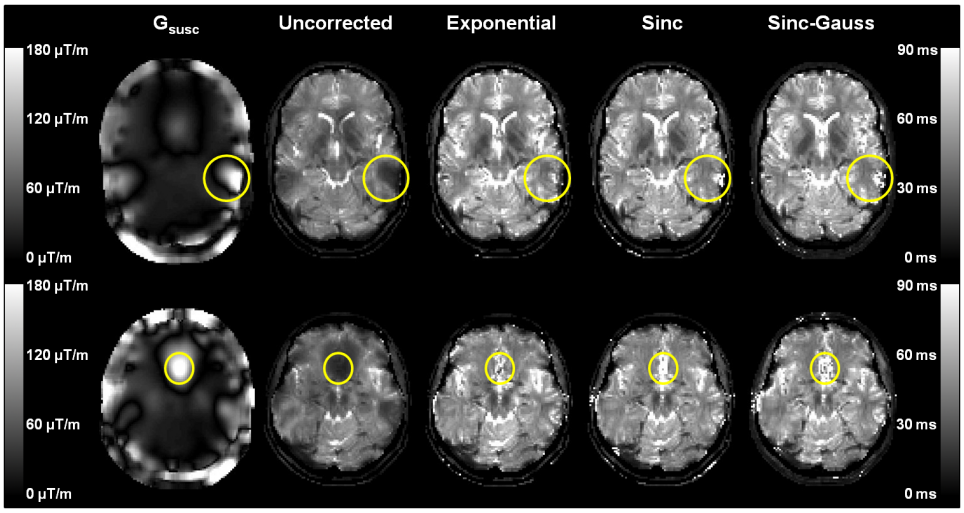

Figure 4.1.3 In vivo examples of the background gradient map, the uncorrected $T2^*$ map and the corrected $T2^*$ maps for various pulse shapes. The circled areas highlight the correction results in regions strongly affected by gradients. *Top:* Single slice of volunteer 1, *Bottom:* Single slice of volunteer 2.

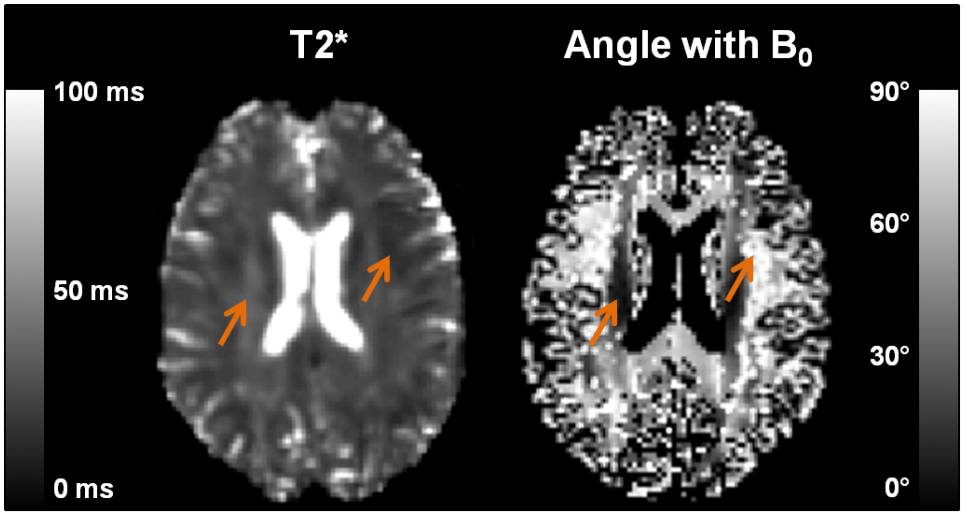

Figure 4.1.4 Example of a slice where the dependence of $T2^*$ on the fiber orientation is visible. The left arrow points towards white matter tracts parallel to the main magnetic field where $T2^*$ appears higher; the right arrow points towards perpendicular fibers with lower apparent $T2^*$.

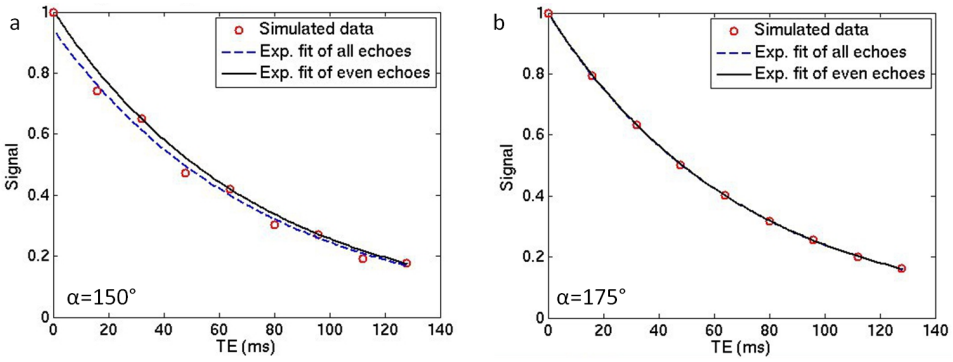

Figure 4.2.1 EPG simulation of the signal development for imperfect refocusing pulses. a) Refocusing pulses with angles of 150° were assumed to simulate the signal at different echo times from $TE = 16$ ms to $TE = 128$ ms with $\Delta TE = 16$ ms. Odd echoes are lowered because they are not formed in the transverse plane. A mono-exponential fit of even echoes reproduces the set $T2$ better than an all echoes fit. b) If the deviation from 180° is only 5°, the influence of imperfect pulses is no longer substantial.

Characteristics of in vivo $T2^*$ maps. The same observations are made in brain maps. Examples of two healthy volunteers are shown in Fig. 4.1.3. The signal-destroying effects of susceptibility gradients in the frontal and temporal lobes are best corrected if exponential excitation pulses are used. In vivo $T2^*$ maps exhibit noticeable structural variations also in areas with very weak background gradients most likely due to their sensitivity on the orientation of blood vessels with respect to the main magnetic field (Fig. 4.1.4). This effect is explained in more detail in Section 5.1.

4.2 Validity of Fast T2 Mapping

Imperfect refocusing pulses and stimulated echoes. In a mono-exponential fit of the signal development simulated with the EPG algorithm, a set $T2 = 70$ ms was estimated in the case of a 30° deviation from a perfect 180° refocusing pulse as 74.47 ms (all echoes fitted). If only even echoes were fitted, $T2$ was estimated as 73.49 ms (Fig. 4.2.1 a). When the deviation from 180° was reduced to 5° in the simulation, the estimated $T2$ values were 70.07 ms for both the all echoes and even echoes fits (Fig. 4.2.1 b).
The EPG fit of echo signal intensities obtained with GRASE acquisitions in a homogeneous gel phantom with the refocusing angle as a fitting parameter reproduced the nominal angles specified in the protocol with high accuracy, both in the case of only 180° RF pulses and also in the case of one 180° RF pulse and subsequent 150° pulses. The actual deviation of the GRASE refocusing pulses from 180° is therefore expected to be negligible.

Phantom VOI	1	2	3	4	5	6	7 (Oil)
$T2_{\text{GRASE}}$ (ms)	38.4 (±1.6)	52.5 (±1.1)	62.1 (±1.4)	67.0 (±1.8)	67.7 (±1.4)	108.2 (±3.4)	73.2 (±1.0)
$T2_{\text{SE}}$ (ms)	34.0 (±1.5)	48.8 (±1.0)	58.0 (±1.1)	62.2 (±1.6)	63.0 (±1.1)	102.9 (±3.6)	53.7 (±1.0)
Volunteers	**WM**	**GM**					
$T2_{\text{GRASE}}$ (ms)	76.5 (±1.7)	84.9 (±3.5)					
$T2_{\text{SE}}$ (ms)	68.2 (±2.2)	73.5 (±2.4)					

Table 4.2.1 Comparison of $T2$ values obtained with GRASE and single spin echoes (SE) in a phantom containing several flasks with different agar and Gd-DTPA concentrations as well as an oil flask (VOIs) and in eight healthy volunteers (white (WM) and gray matter (GM) VOIs).

Diffusion. The $T2$ value of 64 ms in the homogeneous phantom obtained with GRASE was reproduced very accurately with TSE (data not shown). A comparison of single spin echo (SE) measurements with GRASE revealed $\sim$ 5% lower T2 values for single SE data in the flasks with different physiological $T2$ values (Table 4.2.1). All single SE values for $T2$ are only slightly lower than the GRASE values except for the flask containing vegetable oil where $T2_{\text{single SE}}$ is distinctly lower. The difference between GRASE and single SE results for $T2$ was considerably greater in vivo, $\sim$ 12%.

4.3 Leakage Correction in Maps of the Cerebral Blood Volume

Comparison of VASO and DSC in patient group I. The automated thresholding method based on MPRAGE data for identifying individual contrast agent leakage areas is able to select the respective voxels very cleanly, as can be seen from the orange overlays in Figs. 4.3.1 and 4.3.3. Table 4.3.1 supports this finding by demonstrating that the VASO correction hardly affects values in healthy appearing tissue.

Contrast-enhancing tumor voxels with a leaky barrier appear generally very bright in CBV_{VASO} maps. Although they are distinctly less pronounced in the corrected maps compared to the uncorrected maps (Fig. 4.3.1), they tend to be more unobtrusive in CBV_{DSC} maps, with intensities similar to those in gray matter.

The degree of accordance of the VASO and DSC results is shown in the correlation plot in Fig. 4.3.2. While WM and GM values cluster closely around a straight line, both methods yield different, uncorrelated results in tumor VOIs. Corrected CBV_{VASO} values are still much higher than CBV_{DSC} values and are probably severely overestimated. These findings are supported by the group averages in Table 4.3.1. Values found in healthy-appearing tissue with either method are within the respective ranges reported in literature. CBV studies on tumors are hardly available for comparison. While the standard deviations of CBV values in healthy appearing tissue are reasonably low, CBV values in tumors are widely spread between methods but also between patients.

Comparison of DCE and DSC in patient group II. Maps comparing the DCE and DSC methods are shown in Fig. 4.3.3. The lower spatial resolution of CBV_{DCE} maps is noticeable. Contrast enhancing tissue has comparable intensity to gray matter in the CBV_{DSC} map and also in the CBV_{DCE} map where leakage areas have been refitted with the modified Tofts model. The correlation plot in Fig. 4.3.4 confirms that CBV_{DCE} does not exceed CBV_{DSC} in general in tumorous tissue. However, two metastasis values of around 30% marked by arrows raise the group average for CBV_{DCE} to $9.5 \pm 11.2\%$. The results of DCE and DSC are not correlated in contrast enhancing tissue. The accordance is better in healthy appearing tissue but not as good as for VASO and DSC. One reason for this is the smaller size of group II ($n = 18$) compared to group I ($n = 34$). The lower SNR of DCE also contributes to this effect.

All values in healthy appearing brain tissue in patient group II are within literature range (which is rather wide for DCE). DSC values with and without prebolus cannot be compared due to the different composition of the groups. Group I comprises a larger fraction of high-grade gliomas, while five metastasis patients are included in group II but not in group I. Still, the standard deviations of DSC results in both groups are similar, hinting at the robustness of DSC (Table 4.3.1).

Some of these results are presented in Refs. [103] and [104].

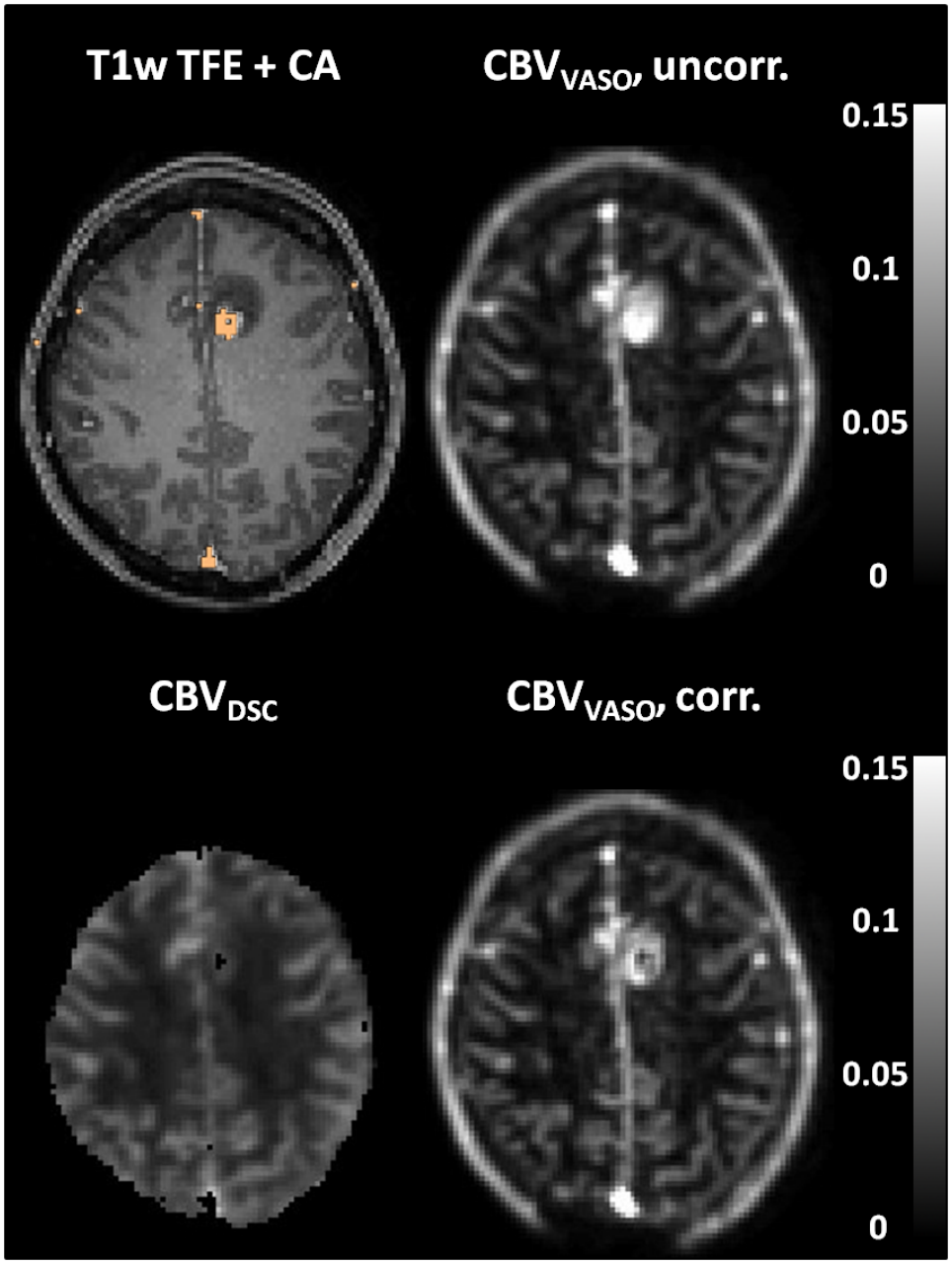

Figure 4.3.1 Comparison of VASO and DSC in a single slice of an exemplary glioma patient. The orange overlay in the T1w TFE image reflects the leakage areas. An uncorrected and a leakage-corrected CBV_{VASO} map are shown together with a CBV_{DSC} map. All maps are windowed from 0 to 15%.

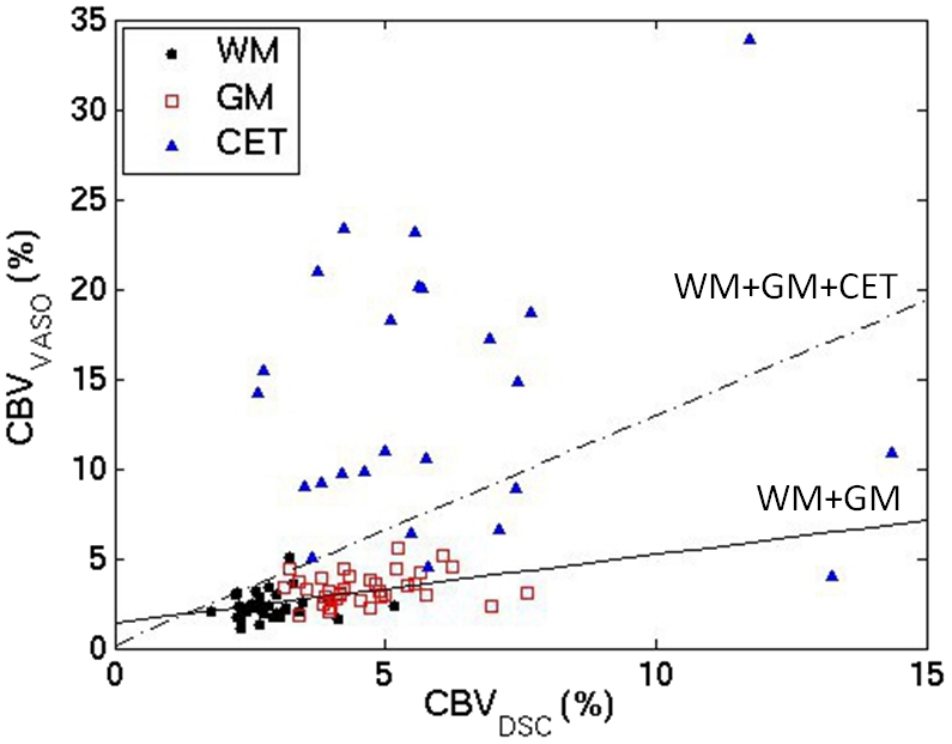

Figure 4.3.2 Correlation plot of CBV values acquired with corrected VASO and DSC in patient group I, separately for white matter (WM), gray matter (GM) and contrast enhancing (CET) tissue VOIs. The solid line represents the regression of GM and WM values only; the dashed-dotted line represents the regression of all values.

		#	CBV GM (%)	CBV WM (%)	#	CBV CET (%)
Group I	**VASO, uncorr**	35	3.4 ± 0.9	2.4 ± 0.8	26	19.2 ± 10.7
HGG 0.54	**VASO, corr**	35	3.3 ± 0.9	2.3 ± 0.7	26	13.5 ± 7.3
	DSC, no pb	34	4.7 ± 1.0	2.9 ± 0.7 [1)]	25	6.1 ± 3.0
Group II	**DSC, pb**	18	3.9 ± 0.8	2.5 ± 0.5	15	4.5 ± 2.2
HGG 0.43	**DCE**	21	5.4 ± 3.0	3.0 ± 2.1	17	9.5 ± 11.2
Literature	**VASO** [66]	13	5.5 ± 0.2	1.4 ± 0.1	n/a	n/a
	DSC [95, 100]	101	3.5 ± 0.8	2.0 ± 0.5	101	3.9 ± 1.7 [2)]
	DCE [74, 101, 102]	10-15	2.6 ± 0.8 to 6 ± 2	1.3 ± 0.4 to 4 ± 1	15	7 ± 6 [3)]

Table 4.3.1 CBV values (group average $\pm$ standard deviation) in two patient groups with different high-grade glioma (HGG) fractions. # denotes the number of individuals included in the averages. VOIs were selected in healthy appearing gray (GM) and white matter (WM) as well as in contrast enhancing tumor tissue (CET). DSC was performed without prebolus (pb) in the first group and with prebolus in the second group. DCE values were calculated using the Patlak model in unaffected voxels and the modified Tofts model in leakage areas.

[1)] Please note that average CBV_{DSC} is not equal to the normalization value of 1.5% because a VOI with *low* white matter CBV was chosen for normalization.
[2)] value reported for high-grade glioma
[3)] value reported for brain tumor

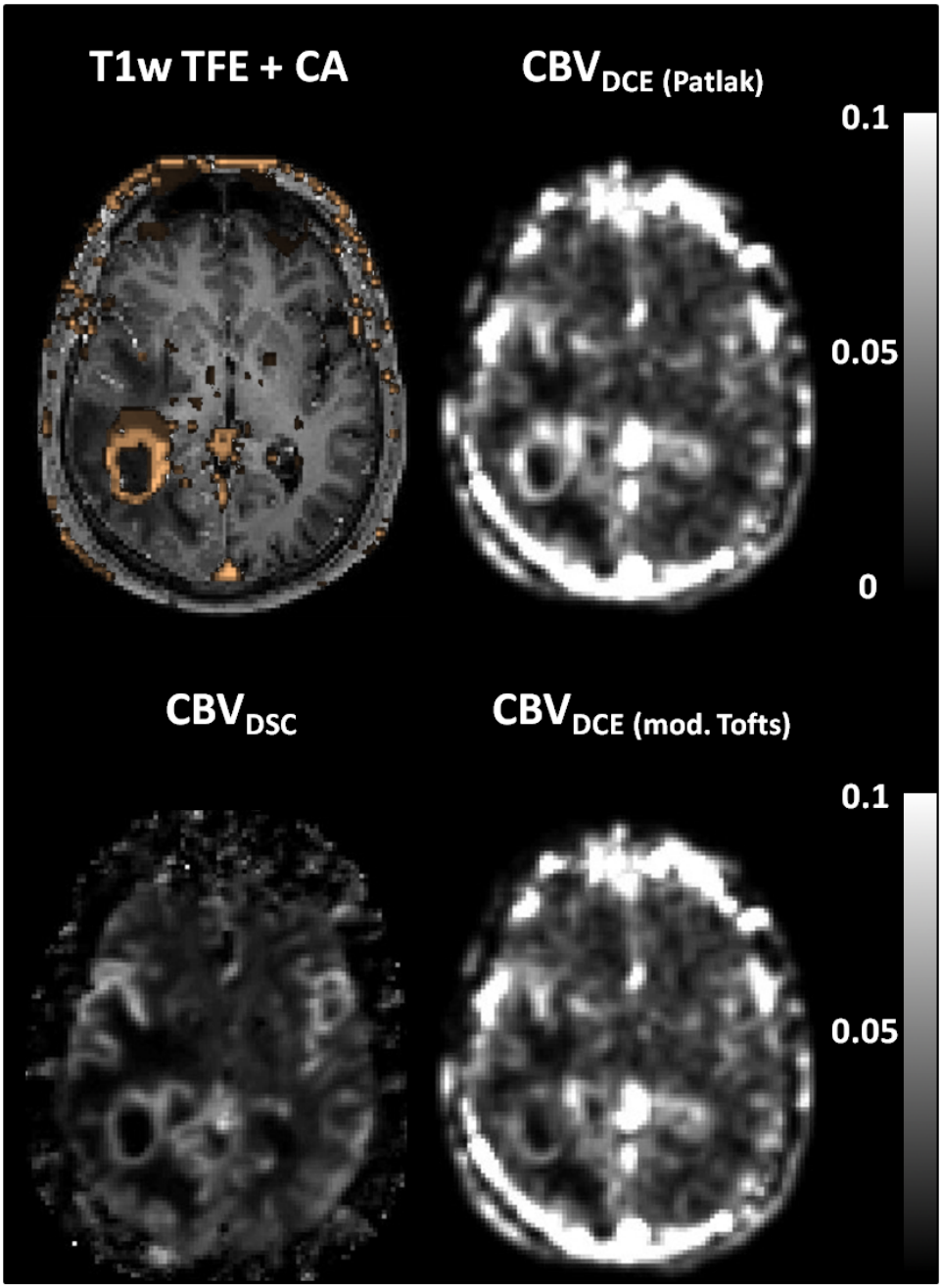

Figure 4.3.3 Comparison of DCE and DSC in a single slice of an exemplary glioma patient. The orange overlay on the T1w TFE image reflects the leakage areas. An uncorrected and a leakage-corrected CBV_{DCE} map are shown together with a CBV_{DSC} map. All maps are windowed from 0 to 10%.

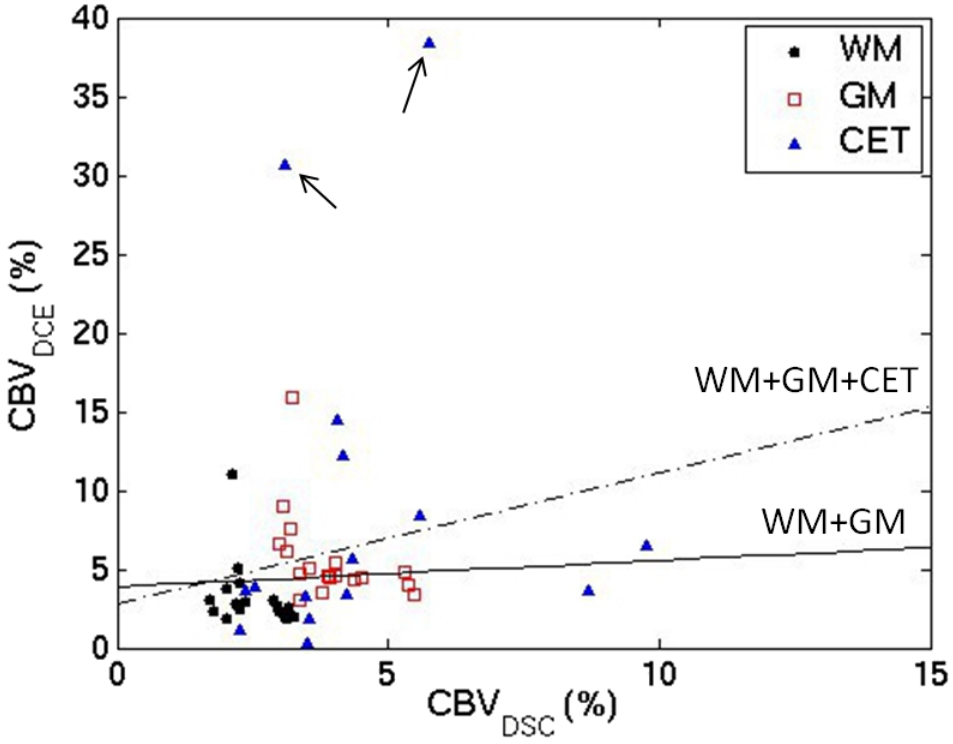

Figure 4.3.4 Correlation plot of CBV values acquired with DCE and DSC in patient group II, separately for white matter (WM), gray matter (GM) and contrast enhancing (CET) tissue VOIs. The solid line represents the regression of GM and WM values only; the dashed-dotted line represents the regression of all values. Two outliers can be explained by metastases (arrows).

4.4 In Vivo Mapping of the Relative Oxygen Extraction Fraction

4.4.1 Characteristics of MR-based rOEF Maps in Healthy Appearing Tissue

Before analyzing pathological areas, it is instructive to first explore general characteristics of rOEF maps in healthy tissue. To avoid application of contrast agent in healthy individuals, CBV (and rOEF) was not measured in healthy volunteers. Instead, unaffected slices in tumor patients where contrast agent is routinely applied were used for the analysis in healthy tissue. An example is shown in Fig. 4.4.1. Quantitative $T2$, $T2^*$ and $R2'$ maps are shown together with relative maps of CBV (acquired with DSC) and OEF. Additionally, a FLAIR image is shown for better anatomical orientation.
All maps are high-quality images. The $T2^*$ map displays the expected anatomical details in the frontal and temporal parts of the brain. Susceptibility gradients are only visible in a thin border zone around the brain. The related intensity decrease in the $T2^*$ map does not stand out because the background is dark as well but the field inhomogeneities lead to artificially enhanced rims in the $R2'$ and rOEF maps. Another feature in $R2'$ and rOEF maps is the bright appearance of the pallidum where iron deposits result in a locally disturbed magnetic field. Also visible is a difference between white and gray matter in the rOEF map.

Table 4.4.1 summarizes the averaged values of the parameters needed for rOEF calculation in two groups of eight healthy volunteers and 55 patients with suspected brain tumors. VOIs were selected only in healthy appearing tissue. $T2$ and $R2'$ are slightly increased in patients compared to the volunteers whereas no such trend is observed for $T2^*$. It is also interesting that the standard deviations of all reported values in the patient group surpass those in the healthy group in spite of the greater number of subjects. Thus even healthy appearing tissue in patients seems to be more heterogeneous than truly healthy tissue in volunteers. rOEF in healthy appearing gray matter is 0.63 ± 0.16. The white matter value is about 40% higher and amounts to 0.90 ± 0.21.

4.4.2 Application on Brain Tumor Patients and Preliminary Immunohistochemical Validation

The following analysis has been submitted for publication in similar form [99]; some preliminary results have been reported in Refs. [105] and [106].

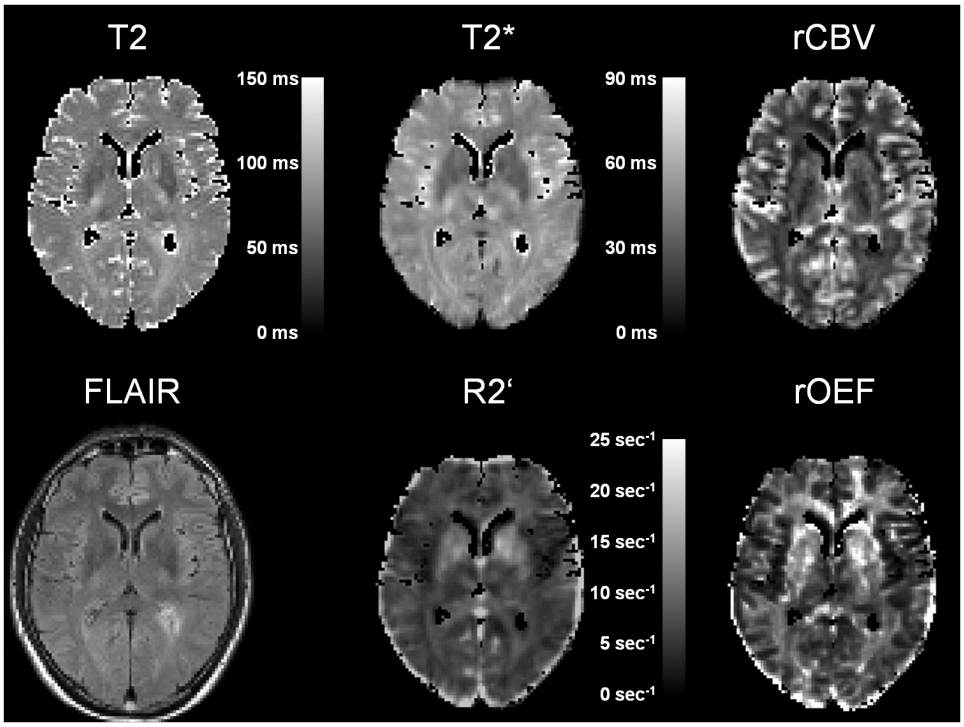

Figure 4.4.1 Single slice in a tumor patient. A small area of tumor related edema at the left dorsal ventricle is visible in the FLAIR image. Else the slice appears unaffected by pathology and can therefore be used to demonstrate characteristics of rOEF maps in healthy tissue. $T2$, $T2^*$ and $R2'$ maps are quantitative, rCBV and rOEF maps show relative values. The FLAIR image serves to show anatomical details. CSF is masked.

VOI	#	Type	T2 (ms)	T2* (ms)	R2' (1/sec)	rCBV	rOEF
GM	8	v	84.9 ± 3.5	53.9 ± 2.1	7.0 ± 2.0	n/a	n/a
GM	55	p	86.9 ± 5.6	51.8 ± 5.7	7.8 ± 1.3	4.5 ± 0.9	0.63 ± 0.16
WM	8	v	76.5 ± 1.7	50.9 ± 1.5	6.6 ± 0.4	n/a	n/a
WM	55	p	79.2 ± 3.6	51.2 ± 4.5	7.2 ± 1.2	2.9 ± 0.5	0.90 ± 0.21

Table 4.4.1 Measured ($T2$, $T2^*$, rCBV) and calculated ($R2'$, rOEF) parameters in healthy volunteers (v) and in healthy appearing gray (GM) and white matter (WM) VOIs of brain tumor patients (p). # denotes the number of subjects included the averaged values. rCBV was not measured in healthy volunteers to avoid the application of contrast agent. rOEF is therefore not available for volunteers.

VOI	Tumor	#	T2 (ms)	T2* (ms)	R2' (1/sec)	rCBV	rOEF
GM		27	96.6 ± 10.5	51.6 ± 8.9	8.3 ± 2.2	4.0 ± 0.7	0.71 ± 0.25
WM		27	80.4 ± 4.7	51.1 ± 5.3	7.4 ± 1.6	2.7 ± 0.5	0.95 ± 0.22
CET	GBM	17	134.9 ± 17.2	81.1 ± 34.4	6.9 ± 2.4	4.7 ± 1.4	0.55 ± 0.32
	°III	7	150.0 ± 99.0	93.7 ± 58.0	5.6 ± 2.8	5.9 ± 2.7	0.33 ± 0.12
T2T	GBM	17	151.3 ± 54.5	76.1 ± 17.6	7.5 ± 2.8	4.4 ± 1.5	0.68 ± 0.38
	°III	7	137.8 ± 56.7	78.3 ± 17.7	6.2 ± 1.4	5.0 ± 2.1	0.52 ± 0.30
	°II	3	149.5 ± 29.9	110.0 ± 43.4	2.1 ± 1.0	2.3 ± 0.4	0.27 ± 0.15
ED	GBM	17	152.2 ± 25.1	98.6 ± 24.8	4.5 ± 2.0	2.8 ± 0.7	0.58 ± 0.26
	°III	7	164.9 ± 77.5	99.7 ± 28.4	4.9 ± 1.7	4.3 ± 1.9	0.48 ± 0.22
	°II	1	130.7	87.3	2.4	2.6	0.28

Table 4.4.2 VOI analysis of 27 tumor patients. VOIs were defined in healthy appearing gray (GM) and white (WM) matter as well as in the tumor (GBM = glioblastoma). CET VOIs were selected in contrast-enhancing tissue, T2T VOIs in non-enhancing tumor-like tissue in FLAIR and T2w FFE images, ED VOIs in edema. # denotes the number of patients. Data from [99].

Fig. 4.4.2 is an example of how rOEF maps of tumor patients can be interpreted in the context of additionally available clinical images. The figure shows five slices of a patient with glioblastoma. The tumor extends over all shown slices, and areas with increased rOEF are also found in all slices. With the help of clinical images which are acquired routinely in MR examinations of glioma patients (MPRAGE with contrast agent, $T2^*$-weighted FFE images and rCBV maps from the DSC acquisition), it is possible to decide when rOEF is artificially increased and when it might indicate truly hypoxic tissue.
Slice (a) demonstrates the effect that strong susceptibility artifacts have on an rOEF map. $T2^*$ is underestimated in such regions, resulting in an overestimation of $R2'$ and rOEF. No sensible conclusion about hypoxia can be drawn in heavily gradient affected areas. Iron deposits in the basal ganglia result in a bright appearance in rOEF maps (slice (b)), which is also an intrinsic artifact of the method. Slice (c) covers a very heterogeneous

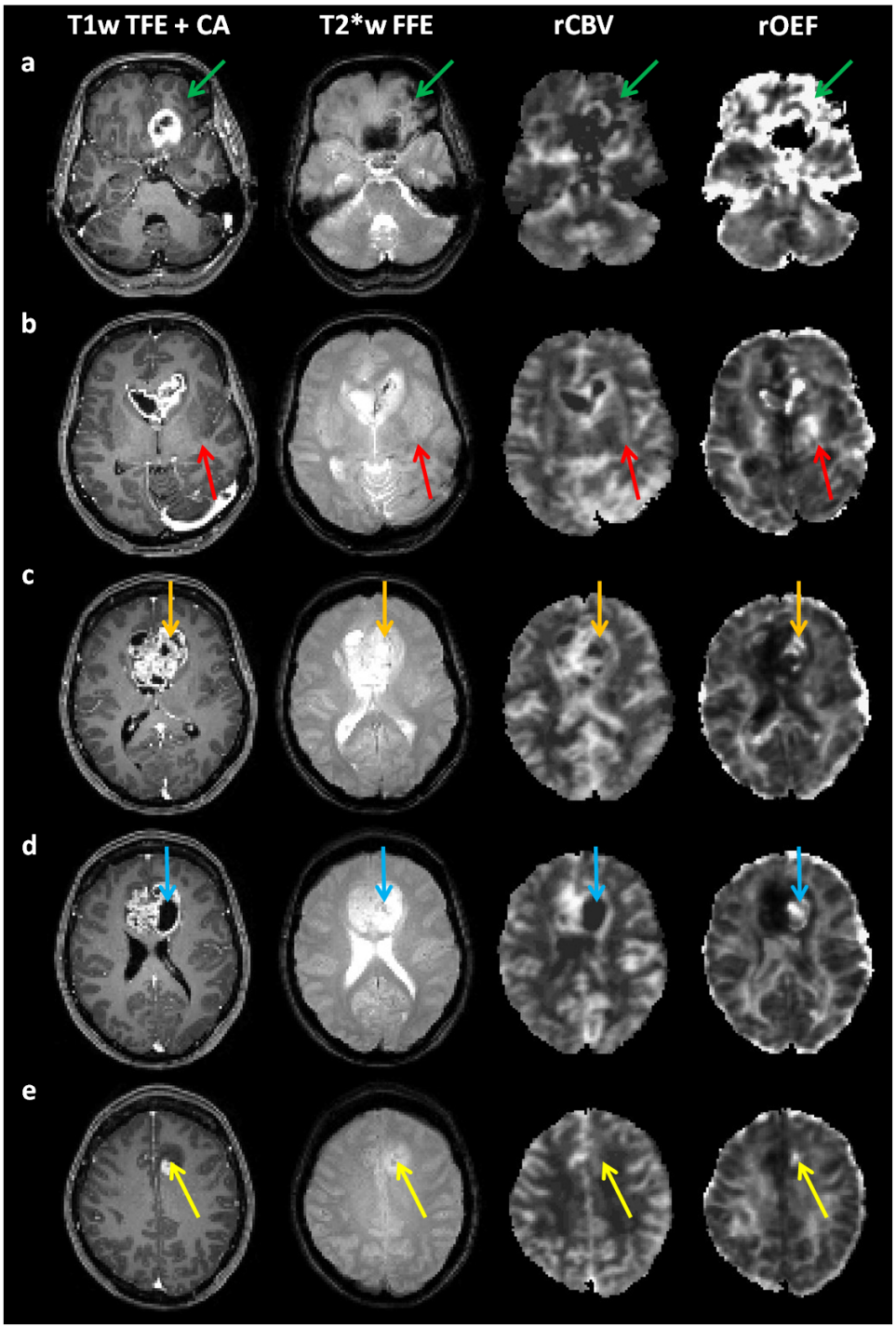

Figure 4.4.2 Several slices of a glioblastoma patient. Spots of increased rOEF values (arrows) are visible in each slice but the causes are different ones. a) rOEF is increased due to susceptibility artifacts also visible in the $T2^*$w FFE image. b) Iron deposition in the basal ganglia causes an rOEF increase. c) The marked area is located in contrast agent enhancing areas with possible necrosis or bleeding, low rCBV and increased rOEF, hinting at perinecrotic, hypoxic tumor tissue. d) rOEF is increased in necrotic tissue in the tumor center due to zero rCBV. e) A small hot spot is visible in the rOEF map. Since it is located in a hyperintense region in the $T2^*$w FFE image outside of edema and has moderate rCBV, it is a potentially hypoxic spot in non-enhancing tumor tissue.

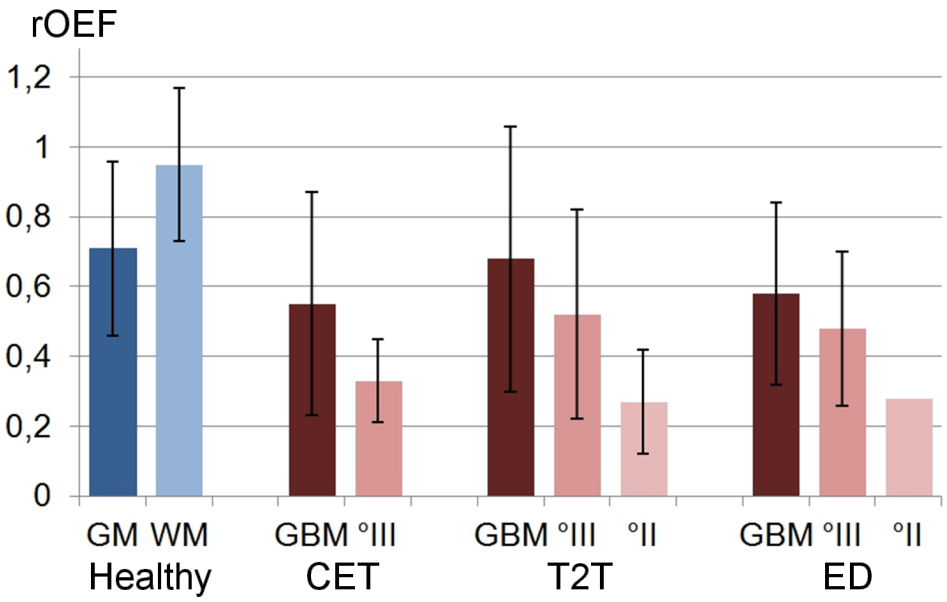

Figure 4.4.3 rOEF values of different tissue VOIs in tumor patients. Data from Table 4.4.2.

tissue part of the tumor. The non-enhancing areas inside the tumor in the MPRAGE+CA image are necrotic tissue. Since those areas are not supplied with blood anymore, rCBV is close to 0 there, resulting in a very high rOEF value that has nothing to do with increased oxygen extraction. However, rOEF is also increased in enhancing tissue close to the central necrosis where it may indeed correspond to hypoxic perinecrosis. Slice (d) shows the central necrosis very distinctly, again with low rCBV and high rOEF. Finally, in slice (e) a small hot spot is displayed in the rOEF map which corresponds to viable, non-enhancing tumor tissue. This might be a truly hypoxic niche.
Summing up, areas with uncorrectably strong background gradients must be excluded from interpretation. Artificially high rOEF values occur in central necrotic tumor tissue and in areas of bleeding and iron deposits due to the sensitivity of the method to susceptibility differences. Artifacts can be identified with the help of clinical images. Apart from that, it was found that most of glioblastomas and °III tumors featured high rOEF in contrast-enhancing tissue and/or non-enhancing tumor-like tissue, in contrast to low-grade tumors. Sometimes those high values must be ascribed to intra-tumoral bleeding but if bleeding can be excluded they suggest the presence of tumor hypoxia.

Table 4.4.2 shows the results of the VOI analysis of 27 patients with

confirmed glioma. Both $T2$ and $T2^*$ are significantly increased in the tumor compared to gray and white matter while $R2'$ is decreased. The blood volume is similar in the averages of healthy gray matter and tumorous tissue. Averaged rOEF is decreased in tumorous tissue despite the frequent presence of hyper-intense niches in high-grade tumors.
Although healthy appearing tissue has the highest rOEF values, in general there is a trend towards increasing rOEF for increasing tumor grade corresponding to malignancy (Fig. 4.4.3. Interestingly, this trend exists although grade II tumors have the lowest rCBV. Considering different tissue types in the tumor, rOEF increases from CET to edema to non-enhancing tumor-like tissue.
A volumetric analysis of the tumors where the volume fraction of hypoxic tumor tissue was determined found an increase of hypoxic tissue in the tumor for increasing tumor grade (data not shown). Among all tumor tissue types, non-enhancing T2T tissue contained the greatest fraction of hypoxic tissue.

Validation with biopsy results. 8 of 25 biopsy samples were taken from MR-hypoxic tissue with high rOEF, 17 from areas with low rOEF. 2 of the MR-hypoxic samples were located in central tumor necrotic tissue and, as expected, showed no or weak HIF1α staining because only living cells are able to express the marker protein. 2 other MR-hypoxic samples showed no or weak staining and thus produced a contradictory result compared to the MR method. The remaining 4 MR-hypoxic samples confirmed the MR result by strong staining. 82% of the MR-normoxic samples showed no or weak staining.

4.4.3 Application on Stroke and Stenosis Patients

A patient example of subacute ischemic stroke is shown in Fig. 4.4.4. Ischemic areas can be identified as signal enhancement in DWI and TTP images, and are reflected as potentially hypoxic areas in the rOEF map. Hyperintense areas in DWI, TTP and rOEF maps are not exactly congruent but part of the ischemic area appears to be truly hypoxic. The ischemic core which consists of irreparably damaged tissue and is bright in the DWI image is surrounded by a larger, diffuse area where TTP is increased. rCBV is visibly decreased (but still $\neq 0$) in the ischemic core and, interestingly, also on the left hand side next to the ventricles (see arrow), where TTP (and $R2'$ – not shown) is increased as well. The rOEF map suggests the presence of hypoxic spots in both areas, in the ischemic core and also on the contralateral side.

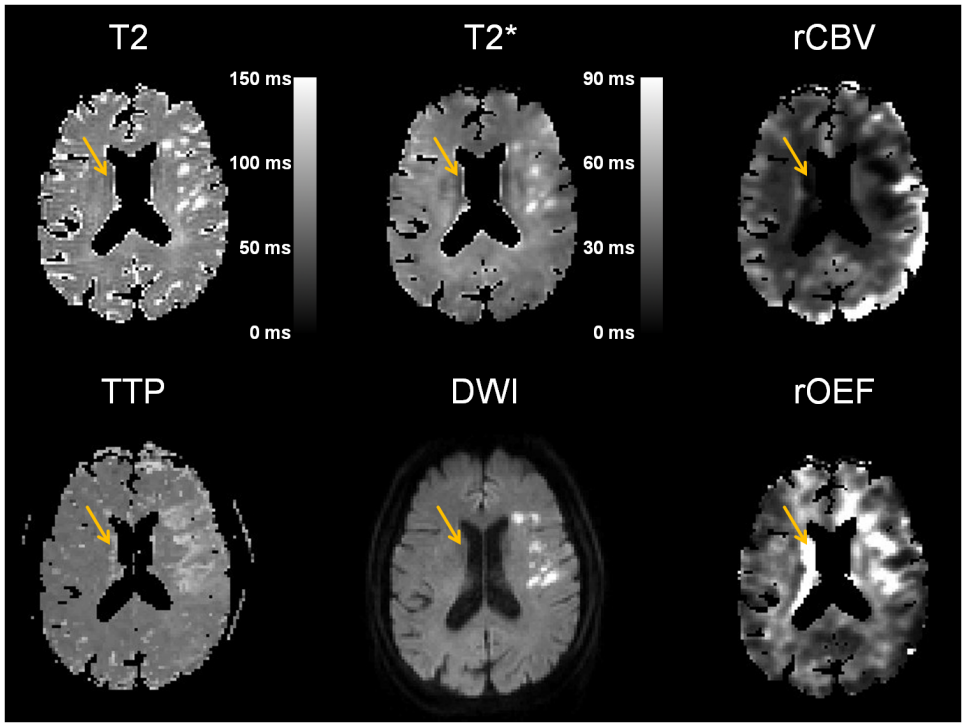

Figure 4.4.4 Single slice in a patient with subacute ischemic stroke. Input maps for rOEF calculation ($T2$, $T2^*$, rCBV) are shown at the top. TTP and DWI images are shown for comparison of visible ischemic areas with potentially hypoxic areas in the rOEF map. The arrow marks a potentially hypoxic area contralateral to the ischemic core.

VOI	# (acute/sub/stenosis)	TTP(sec)	rCBV	rOEF
unaffected	13 (6/3/4)	3.1 ± 0.6	4.2 ± 1.0	0.57 ± 0.18
DWI lesion	7 (3/2/2)	3.6 ± 1.2	2.7 ± 1.1	1.03 ± 0.62
long TTP	5 (2/2/1)	4.7 ± 0.7	2.5 ± 2.2	1.44 ± 0.85

Table 4.4.3 TTP, rCBV and rOEF values in different VOIs (unaffected tissue, DWI lesion and prolonged TTP area around the DWI lesion) in a stroke population. # denotes the number of subjects included the average; numbers in brackets are the number of subjects with acute stroke, subacute stroke and arterial stenosis.

Results of measurements in a stroke patient population are summarized in Table 4.4.3. Tissue VOIs were defined in unaffected brain (in all 13 patients), in the ischemic core visible in the DWI image (which was existent in 7 patients) and in an area where TTP was prolonged (> 4 sec) but which was not affected in terms of diffusion (which was possible for 5 patients). Over the tissue VOIs 'unaffected' (healthy-appearing brain) - 'DWI lesion' (visible lesion in DWI image) - 'long TTP' (prolonged TTP > 4 sec) the parameters TTP, rCBV and rOEF exhibit increasing, decreasing and increasing trends, respectively.

5 Discussion

5.1 Error Sources and Their Influence on Multiple Gradient Echo T2* Quantification

Susceptibility effects. The values obtained for $T2^*$ in healthy volunteers and tumor patients of 50.9 to 53.9 ms in white and gray matter (Table 4.4.1) are in very good agreement with the literature reports of $\sim$ 50 ms [77, 107, 83]. The susceptibility gradient correction with exponential pulses is therefore a valuable tool for increasing the accuracy of in vivo $T2^*$ mapping.
The superior performance of the exponential pulse over other pulse shapes has various reasons: The exponential and the sinc pulses can be represented analytically (Eqs. 3.1.3, 3.1.4), while the sinc-Gauss shape can only be approximated. Also, the sinc and the sinc-Gauss time profiles repeatedly assume the value 0 which leads to signal intensity losses.

$T2^*$ values cannot be corrected completely to their true values for any of the examined shapes as can be seen in the bottom row of Fig. 4.1.1. However, the areas that were too hypo-intense before to allow diagnostic evaluation are smaller when an exponential excitation pulse is used and the correction for susceptibility gradients is performed. Fig. 4.1.3 shows that areas close to air-filled cavities in the orbitofrontal cortex or in the inferior temporal lobes of the brain (marked by circles) typically appear very dark in uncorrected $T2^*$ maps but become considerably brighter when the correction is performed. Corrected $T2^*$ values in those areas are closer to the true values. Again the difference of the three pulses can be observed in the circled regions: Most of the previously lost areas in the shown $T2^*$ maps is recovered when an exponential pulse is used. The correction works worse with the sinc and sinc-Gauss pulses where the amount of scattered, bright values in the circled areas is visibly larger.

We measured susceptibility gradients up to 400 μT/m in vivo. Litera-

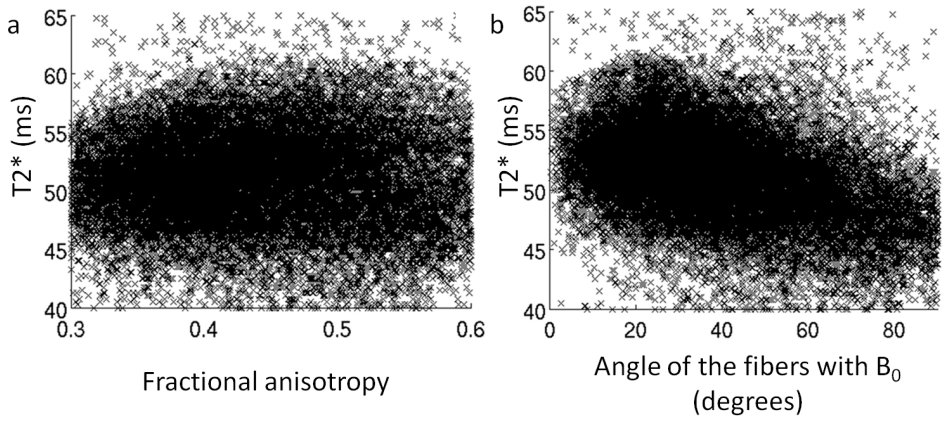

Figure 5.1.1 Dependence of measured $T2^*$ on fractional anisotropy (a) and on the angle that fibers include with the main magnetic field B_0 (b). SE-EPI DTI data (32 gradient directions, $TE = 47$ ms, $TR = 14.3$ sec, resolution $2 \times 2 \times 3$ mm^3, matrix size $112 \times 112 \times 60$) were averaged over four healthy volunteers (3 males, 30.3 ± 6.6 years). Figure adapted from [109].

ture values range from $300 - 500$ μT/m [78, 108]. If exponential excitation pulses are used and the described correction for the modified signal decay is performed, $T2^*$ mapping is more accurate even in areas affected by stronger background gradients. Exponential pulses proved to be superior to sinc and sinc-Gauss pulse shapes in terms of gradient strength and are therefore recommendable in in vivo applications. A sufficient compensation of effects from a Lorentzian-shaped slice profile can be achieved by selecting the interleaved acquisiton mode and by accepting an interslice gap.

Effects of white matter fiber orientation. To explore the generally greater structural variation of $T2^*$ values in the brain (which is not reflected in $T2$ maps), $T2^*$ (acquired as described in Section 3.1) was correlated with fractional anisotropy (FA) and with the fiber angle to the main magnetic field [109]. While FA has no obvious influence on $T2^*$, the fiber direction does play a significant role (Fig. 5.1.1). If the fibers are oriented parallel to the B_0 field ($0^\circ - 5^\circ$), $T2^* = 52.7 \pm 3.1$ ms is noticeably greater than in the case of perpendicular fibers ($85^\circ - 90^\circ$, $T2^* = 47.2 \pm 7.3$ ms). Extensive white matter heterogeneity in $T2^*$ maps has been reported at first for 7T scanners [110] but later also at 3T, where $T2^*$ was measured for different head positions relative to the main field [111, 112]. Myelin content and structure as well as effects associated with fiber and microvessel orientation relative to the B_0 field are held responsible [113–115]. To quantitatively correct for these structural effects in $T2^*$ and rOEF maps,

DTI measurements would have to be included in the protocol and an analytical relationship between $T2^*$ and fiber orientation would have to be derived.

5.2 Error Sources and Their Influence on Fast T2 Quantification

The measured values for $T2$ from 76.5 ms to 79.2 ms in white matter and from 84.9 ms to 86.9 ms in gray matter (Table 4.4.1) are well within literature range [83, 84]. Most previous studies found values between 70 ms and 90 ms [107, 83, 84]. Since the widespread literature range for $T2$ suggests the influence of multiple effects on the apparent value for $T2$, the GRASE sequence as used in the hypoxia study protocol was tested for reliability of the results by means of simulations as well as phantom and volunteer studies.

Imperfect refocusing pulses and stimulated echoes. The results of the extended phase graph simulations, where the signal intensities at different echo times were calculated for imperfect refocusing pulses, suggest a negligible influence of stimulated echoes on the signal intensity at least for deviations from 180° of around 5°. Even if all (and not only the even) echoes are fitted mono-exponentially, the given $T2$ is reproduced very well. For larger deviations, it is advisable to fit only the even echoes because then the signal-lowering effect in odd echoes becomes visible (see Fig. 4.2.1). A small contribution from stimulated echoes manifests itself in a slight overestimation of $T2$.
The nominal refocusing pulse angles of 180° as specified in the GRASE protocol were confirmed by homogeneous phantom measurements and an EPG fit of the measured data. Although an effective angle instead of a slice profile was assumed in the EPG calculations, the influence of imperfect refocusing pulses and stimulated echoes in the GRASE sequence in combination with an even echoes fit is negligible in the light of these findings – in accordance to the expectation: The phase shift of 90° between excitation and refocusing pulses in the GRASE sequence is selected precisely to reduce accumulating contributions from stimulated echoes.

Diffusion. The accordance of GRASE and TSE results for $T2$ in the homogeneous phantom is expected, as influences from imperfect pulses and diffusion are equal in both sequences, when the same imaging parameters are selected.
The situation is different when single spin echo imaging and GRASE are

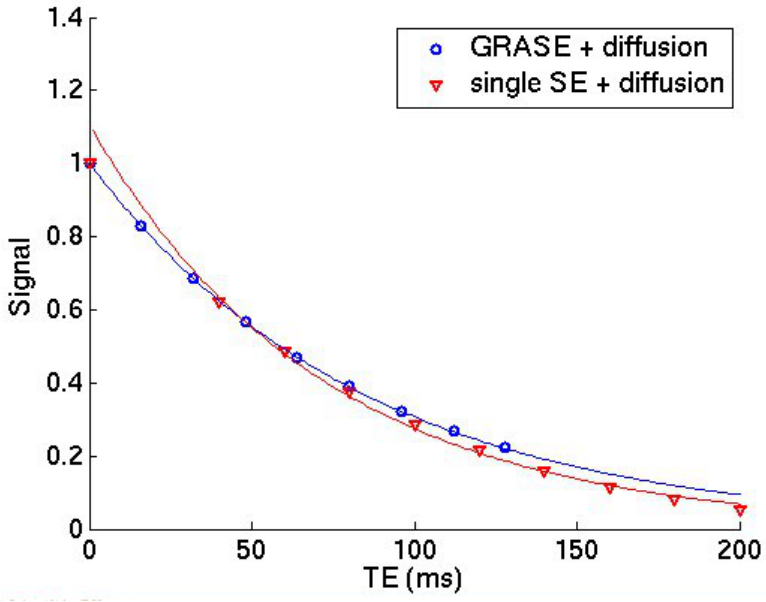

Figure 5.2.1 Simulated echo signal intensities when diffusion is taken into account. The echo signal intensities were calculated for a GRASE ($n_{\text{GRASE}} = 8$ refocusing pulses after one excitation, corresponding to 8 echoes) and a single spin echo sequence ($n_{\text{single SE}} = 1$ refocusing pulse after each excitation for 9 echoes). Eq. 3.2.1 with $T2 = 85$ ms, $TE_{1,\text{ GRASE}} = 16$ ms, $\Delta TE_{\text{GRASE}} = 16$ ms, $TE_{1,\text{ single SE}} = 40$ ms, $\Delta TE_{\text{single SE}} = 20$ ms was used for simulations. Typical values for the diffusion constant D and for the gradient strength G were assumed. Also shown are the mono-exponentially fitted signal curves (continuous lines) for the simulated GRASE and single SE echo intensities. Since diffusion is not accounted for in the fit, the results for the fitting parameter $T2$ depend on the sequence.

compared. In a single spin echo experiment with only one refocusing pulse, diffusion is expected to decrease the apparent $T2$ in vivo if a simple mono-exponential decay is assumed instead of the more realistic decay in Eq. 3.2.1. A GRASE sequence with 8 echoes created by 8 refocusing pulses is expected to produce longer apparent $T2$ values. This effect is presumably weaker in a phantom where the local environment of the spins is much more homogeneous and diffusion of single spins hardly alters the state of the spin system. These expectations were confirmed in phantom and in vivo comparisons of single SE and GRASE imaging, where the difference between $T2_{\text{ GRASE}}$ and $T2_{\text{ single SE}}$ was larger in vivo than in a phantom containing small bottles with different $T2$ values (see Table 4.2.1). The small difference in the phantom is probably related to remaining stimulated echo effects leading to a minor overestimation of $T2_{\text{ GRASE}}$.

Assuming typical values for the diffusion constant D of water protons in brain tissue and for the gradient strength G, it is possible to estimate the difference in fitted apparent $T2$ when a mono-exponential decay is

assumed for the evaluation of GRASE and single SE data. Such an estimation is shown in Fig. 5.2.1 for $T2 = 85.0$ ms, using the echo times that were selected to acquire the data in Table 4.2.1 and assuming a typical imaging gradient strength $G = 5$ mT/m and an apparent diffusion coefficient $D = 0.5 \cdot 10^{-9}$ m^2/s [116]. When the echo signal intensities in Fig. 5.2.1 are fitted without accounting for diffusion, GRASE data result in $T2 = 84.7$ ms (even echoes fit), while single SE data result in $T2 = 72.0$ ms. This is in good agreement with the observation for gray matter in Table 4.2.1 ($T2_{\mathrm{GRASE}} = 84.9$ ms, $T2_{\mathrm{SE}} = 73.5$ ms) and confirms that it is justified to neglect diffusion effects and assume a mono-exponential decay when evaluating GRASE data. Using the more realistic equation 3.2.1 would introduce additional problems like the need for a map of the gradient strength in the direction of diffusion and voxelwise determination of the diffusion constant.

Partial volume effects. Hydrogen nuclei in the brain exist in different water environments, e.g. in myelin bilayers, cytoplasm or CSF, all of them corresponding to different $T2$ values [117]. If more than one of these compartments are present in an image voxel, $T2$ decay will exhibit multi-exponential behavior. However, multiple fitting parameters decrease the robustness of the fit, especially if only few echoes are available, and the results might depend on the initial parameter estimates. Also, a very high SNR is necessary to distinguish components with similar $T2$: A clinically unfeasible SNR ~ 700 is required for distinguishing among different white matter components [118]. Usually, three $T2$ components can be identified in brain tissue: a short component of ~ 15 ms corresponds to compartmentalized water between myelin bilayers. The dominant component of ~ 80 ms represents intra- and extracellular tissue water, while CSF has a large $T2$ value > 1 sec [119–121].
Possible solutions for removing the CSF component from $T2$ maps could be to sample only part of the $T2$ decay, to use prior knowledge about the $T2$ values of different compartments (which however vary in different regions of the brain) in a multi-exponential fit and disregard the contribution of the long component, or to employ CSF-suppressing sequences (with a negative effect on SNR).

5.3 Quantification of the Cerebral Blood Volume

Since a dysfunctional blood brain barrier frequently occurs in brain tumor patients, three different quantification methods for the cerebral blood volume were tested for their capability of being modified to yield reli-

able CBV values also in brain regions where the blood brain barrier is disrupted. The VASO method with an extended model for applicability in leakage areas was compared to the DSC method in one patient group. DCE and DSC were compared in another patient group. Two known models were used for DCE evaluation. The Patlak model assumes low permeability of the blood brain barrier while the modified Tofts model does not requires this but introduces an additional fitting parameter. A contrast agent prebolus was used for the DSC measurement in the second patient group to suppress leakage effects.

All three methods are useful for CBV mapping of healthy appearing tissue. For application in contrast agent leakage areas, these areas need to be identified. The suggested thresholding method based on white matter histograms of MPRAGE data facilitates an automatic and individual procedure to identify contrast enhancing tissue. The assumption of conformity between contrast enhancing areas and leakage areas is reasonable for gliomas but that may not always be satisfied in other tumors or lesions. All CBV values in healthy appearing white matter (2.3% to 3.0%, from Table 4.4.1) and gray matter (3.3% to 5.4%, from Table 4.4.1) correspond to literature values which are 1.3% to 4% in white matter and 2.6% to 6% in gray matter [66, 74, 95, 100–102].

Both VASO and DCE produce noticeably different CBV values in leakage areas depending on whether or not extravasation is included in the calculations (see right columns in Figs. 4.3.1 and 4.3.3), confirming the hypothesis that effects resulting from a dysfunctional blood brain barrier must be taken into account if CBV is to be mapped quantitatively and accurately. However, due to the lack of a gold standard for in vivo CBV quantification in pathologic tissue and the very few reported literature values, the actual accuracy of the employed corrections is difficult to judge.

Leakage is not directly taken into account in the analysis of DSC data as performed in this study. However, $T1$ effects in extravascular space resulting from escaping contrast agent are diminished with the help of a prebolus. Possible $T2^*$ effects are not suppressed with this method. Since both effects lead to opposite signal changes, they might cancel out at least partly in the patient group averages. The true reliability of CBV_{DSC} is therefore difficult to determine. The population averages appear realistic, though. Models where leakage is included in the DSC evaluation have been proposed [95, 90, 122] but they are complex and difficult to fit to patient data of mixed quality.

Regarding VASO, the difference in CBV between healthy and contrast enhancing tissue appears very large. An increase in CBV is expected in

a patient population where more than half of the subjects suffers from high-grade gliomas but corrected CBV_{VASO} in CET is almost six times higher than in healthy tissue (although it is 30% lower than uncorrected CBV_{VASO}). CBV_{DSC} and CBV_{DCE} are only increased by a factor of 1.8 and 3.2 relative to healthy tissue. A reason for this might be that although the VASO leakage correction takes into account the existence of an extravascular compartment where the relaxation is influenced by contrast agent, it neglects water exchange between extra- and intracellular compartments. Evidently this assumption distorts the results.
It is also possible that the condition $T1_{\text{tissue, post}} \ll TI$ is not met in areas where contrast agent leakage through a partially damaged blood brain barrier is slight and the relaxation behavior of tissue is only weakly influenced.
Furthermore $T1$ was assumed to be uniformly 1300 ms across the whole brain which is certainly not satisfied in reality. 1300 ms is a frequently reported value for healthy brain tissue [123] but we found values up to 4 sec in solid high-grade glioma tissue. The correction term subtracted from uncorrected CBV in Eq. 2.4.5 is 0.29 for $T1 = 4000$ ms but 0.16 for $T1 = 1300$ ms. Adding a $T1$ mapping sequence to the VASO protocol would therefore considerably increase the accuracy of CBV_{VASO} but also the acquisition duration for a required resolution of 30 slices with $2 \times 2 \times 3$ mm^3.
Of less impact is the assumption of constant C_{par} and v_e values of 0.75 and 0.22, respectively. Values in tumor tissue might deviate from the assumed values but as they are not part of the exponential term they influence the result less than an incorrect $T1$.

Whole-brain CBV mapping has been proven possible within a clinical DCE patient examination protocol, with the drawback of a rather low spatial resolution of $3 \times 3 \times 8$ mm^3. SNR limitations and the need for a sufficiently fast sampling of the AIF put restrictions on the resolution of DCE. A possible solution was reported in Ref. [75], where two dynamic series were acquired, the first with a low spatial but high temporal resolution and the second one vice versa. The AIF was determined from the first, high temporal resolution scan and recalculated for the main bolus in the high spatial resolution acquisition. However, two bolus injections are required for this method, as well as a repetition of $T1$ mapping. The acquisition time is therefore too long for a routine clinical application. Both VASO and DSC yield higher resolution CBV maps than DCE but increased permeability is easier included in the DCE model.
The validity of the Patlak model has been proven up to a permeability

of $K^{trans} = 0.03$ min^{-1} in literature [74]. Average K^{trans} in patient group II was measured to be 0.131 ± 0.195 min^{-1} in CET, 0.041 ± 0.079 min^{-1} in GM and 0.013 ± 0.018 min^{-1} in WM. Replacing the Patlak model by a more realistic model in contrast enhancing tissue is therefore necessary.
Several possibilities exist to perform the $T1$ mapping required for DCE evaluation. A much favored method is to exploit the dependence of the signal on the flip angle for a spoiled FLASH sequence and to calculate $T1$ from acquisitions with two different, optimized flip angles. However, it was shown that application of this method is only advisable on 1.5T scanners. For higher field strengths, the flip angle cannot assumed to remain constant across a whole slice, and an additional $B1$ mapping is necessary for correction [124] which relativizes the gain in acquisition time. Therefore, sampling of the saturation recovery curve was performed for $T1$ mapping in this study.

The usual assumption of a linear relationship between contrast agent concentration and change in the respective relaxation rate employed in both DSC and DCE was found to be true for $R1$ changes at 3T for in vivo Vasovist concentrations. Vasovist is a Gadolinium-based blood pool contrast agent similar to Gd-DTPA. For changes of $R2^*$ on the other hand, a parabolic dependence was found [125]. The conversion of the signal time curve into a concentration time curve is therefore expected to be more accurate in DCE than in DSC.
Regarding time aspects, acquisition takes only a few minutes for all three CBV quantification methods with the protocol parameters as specified above. Still, application of contrast agent makes it necessary to perform CBV measurements at the end of the clinical protocol (which takes about $20 - 30$ min) when patients are frequently restless and start moving. If the data cannot be motion-corrected, the image quality can be severely affected by motion artifacts up to the point of rendering them useless. DSC data evaluation included the Stroketool motion correction procedure. Minor to medium shifts of single dynamics can be corrected well with this routine. Respective corrections of DCE data are more problematic. Rotation and reslicing of a 3D volume leads to an incorrect calculation of the delay between saturation and slice acquisition. The situation is even more precarious for VASO. The pre- and post-contrast volumes can be coregistered to each other but if the patient is moving during the 35 sec of either VASO acquisition, the volume is severely affected by artifacts without any possibility to correct for this. Accordingly, the quality of CBV_{VASO} maps was frequently rather poor in the presented patient study.

DSC is an established method for CBV measurements in the clinic.

Since the AIF needs to be determined very accurately for an absolute quantification of CBV, usually pathological tissue is compared to a healthy, contralateral VOI. Problems can arise in systemic diseases because then healthy white matter cannot be taken as a normalization reference for transforming the relative into absolute values. That was the motivation to test VASO and DCE for their potential to replace DSC in clinical tumor protocols where a short acquisition time is an absolute requirement, whole-brain mapping is needed to cover the sometimes very extended affected brain areas, and where the blood brain barrier might be permeable for contrast agent.
VASO turned out to be a suitable method for CBV mapping in subjects with an intact blood brain barrier, with the advantages of being fast and providing high spatial resolution but it is not useful for application in more agitated tumor patients. Additional $T1$ mapping with the resolution of VASO (which would considerably increase acquisition time) as well as further modifications of the VASO model to account for water exchange between extra- and intracellular compartments are required to provide adequate leakage correction for the VASO method. Even then the problem of patient motion and resulting poor-quality CBV maps remains unsolved.
The applicability of DCE is restricted by its low SNR and subsequent limited spatial resolution. The large voxel size needed to collect a sufficiently high signal leads to partial volume effects, especially in the sampling of the arterial input function. However, if mapping of only part of the brain is sufficient or if additional quantitative information on the vascular permeability is needed, DCE is a good choice.
DSC was chosen in both the tumor and the stroke hypoxia studies presented in this thesis, in the case of tumor patients because of its robustness and in the case of stroke patients (where even the number of slices had to be reduced for acceleration) to allow for faster scanning because of time limitations.

Regarding alternative methods for CBV quantification without contrast agent, preclinical approaches have been proposed based on modifications of VASO [126] or arterial spin labeling [127] where blood is used as a native tracer. However, apart from an intrinsically much lower SNR, they are all inflow techniques and are thus restricted to the arterial blood volume which certainly does not correspond to the deoxygenated blood volume actually needed for OEF quantification.

5.4 Quantification of the Oxygen Extraction Fraction

5.4.1 Summary of Findings in the Context of Literature Reports

The numerous assumptions of the underlying tissue model described in Section 2.1 are satisfied to varying extent in different parts of the brain. Also, a relative measurement of the total blood volume was performed whereas absolute values for the post-capillary venous volume are required in the model equations. These limitations as well as the need to complete the acquisition in a few minutes to make the protocol applicable for the clinic restrict the oxygen extraction fraction measurement with the presented method to a relative quantification.
rOEF values between 0.63 and 0.95 were found in healthy appearing tissue. Absolute OEF values of around 0.4 distributed homogeneously across the brain were reported in PET studies [54]. MRI studies using GESSE-based approaches described in Section 2.1 found values between 0.3 and 0.5 [53, 128, 45]. However, it should be stressed that those literature values are of limited reliability due to the coupling of OEF and dCBV in a simultaneous measurement of both parameters [58]. In 2011, an MRI method with independent parameter measurements yielded values for the oxygen saturation Y of 0.67 in gray matter and 0.57 in white matter [129]. Although strictly speaking the *venous* oxygen saturation is needed for a conversion to OEF (see Eq. 2.1.4) whereas the reported oxygen saturation represents a value averaged over the arterial and venous compartments, the oxygenation difference between gray and white matter reflects the observed difference in rOEF in the Results section.

The benefit of the presented method is its capability of highlighting pathological tissue in rOEF maps which might be hypoxic, while at the same time being a very gentle patient examination with a minimum of additional time and effort for the patient and without exposure to radiation. It is very advisable to additionally screen clinical patient images beside maps of rOEF, as confounding factors like field disturbances due to susceptibility effects or tumoral bleeding and necrosis result in artificially increased rOEF values. The reason for this is the invalidity of the model in such regions: If tissue parts are not perfused anymore, as in necrotic areas, the blood volume approaches 0. If the magnetic field is influenced by additional gradients, $R2'$ becomes large. Both effects increase the calculated rOEF value whereas the model assumes susceptibility perturbations

arising from intact post-capillary venous vessels in areas of augmented oxygen extraction as the sole cause for an increased rOEF value. Since clinical images are always acquired in routine patient examinations and since with this information a distinction between falsely hyperintense rOEF areas and supposedly true hypoxic spots is possible, rOEF can be considered as a novel, MR-based marker with the capability to identify hypoxic spots as well as to distinguish between different grades of hypoxia.

Recently, an alternative non-BOLD-based approach has been suggested in literature, termed QUantitative Imaging of eXtraction of Oxygen and TIssue Consumption (QUIXOTIC) [130]: The signal from the post-capillary venular blood component is isolated with velocity-sensitive pulses that selectively dephase spins above a cutoff velocity. Subtraction of control and tag images eliminates signal from the static tissue, CSF, arterial and capillary blood compartments. $T2$-weighted images are acquired at different effective echo times and the resulting $T2$ maps are converted to Y_v with a calibration curve based on values from in vitro bovine blood measurements. This technique allows in principle a voxel-by-voxel mapping of OEF, although with a limited resolution of $3.9 \times 3.9 \times 10$ mm^3. It has been performed on phantoms and healthy subjects but is still restricted to single slice acquisitions with a rather long acquisition time of 5 min 30 sec. Additionally, only gray matter has a suffiecient SNR to produce a measurable signal. It is therefore not yet suitable for whole-brain mapping in brain pathologies. A mean venous oxygenation level of $66.7\% \pm 3.9\%$ was measured in gray matter of four healthy volunteers with this method.

5.4.2 Critical Evaluation of Model Assumptions

Numerous factors currently prevent an accurate and absolute quantification of the oxygen extraction fraction. A recent numerical study tested the impact of several model assumptions in a systematic way [59]. To verify the assumption of the blood vessel network as straight, randomly oriented cylinders, the magnetic field distribution around such a cylinder network was compared to the field distribution of a more realistic microvascular mouse network obtained with intravital microscopy. The time evolution of the signal was computed for both field distributions. In vivo vessels are actually more tortuous than cylindrically shaped but the effect of cydrindrical and spherical field perturbers was found to be similar. This is an important finding for the applicability of the model in pathological tissue. The increased permeability of tumor vessels is probably a much

larger problem than their altered shapes.
Another aspect concerning vessels is their orientation. Accounting for a non-isotropic distribution of vessel directions in the derivation of the equation for Y could decrease the observed bias on $T2^*$ and OEF especially in structured white matter.
The influence of water diffusion on $T2^*$ was also examined in the numerical study. The tissue model assumes that diffusion can be neglected (static dephasing regime). A simulation showed that for very small vessels with a radius less than 3 μm, diffusion introduces a 25% error on the oxygen saturation Y. For a vessel radius greater than 6 μm, this error was reduced to 9%. Radii of capillaries are reported as $3.2 \pm 0.8\,\mu$m in the healthy human cerebral cortex, those of arterioles range from $5 - 60$ μm, and venule radii are 7.5 - 90 μm [131]. While a high brain oxygenation Y is underestimated, a low oxygenation is overestimated when diffusion is neglected.
Another simplification of the tissue model is the assumption of a negligible intravascular signal contribution. This was indeed found to be true, with a maximum error of 4% on $T2^*$ in simulations where the oxygenation level was varied from 0.2 to 0.8 [59].
Both the $T2$ and $T2^*$ measurements are subject to partial volume effects. Typically there is more than one $T2$ or $T2^*$ component present in a voxel. Apart from the challenge of incorporating multiple components in the rOEF model, a reliable determination of more than one component is already difficult in the mapping of transverse relaxation times. Usually equally good multi-exponential fits can be achieved for different combinations of fitting parameters. A possible solution would be to use prior knowledge of approximate relaxation times of the long and short $T2$ components in the form of fixed values in the fit to reduce the number of fitting parameters, and to disregard long $T2$ components in OEF calculations since oxygen is not metabolized in water compartments.
The oxygen extraction fraction is actually defined as the difference between arterial and venous oxygen saturation, normalized to arterial saturation. With an independent measurement of total CBV, only the oxygen saturation averaged over arterial and venous compartments can be determined. Consequently, the calculated oxygen extraction is underestimated. Currently, there exists no method to independently determine whether the deoxygenated blood volume fraction varies across the brain. This problem also stands in the way of an absolute quantification of OEF with MR.

5.4.3 Evaluation of Obtained Results

Healthy appearing tissue. Returning to the results of this work, rOEF maps of healthy-appearing tissue do not appear completely homogeneous across the brain like in PET studies but show increased values in areas with known iron deposition like the pallidum [36]. The equation for rOEF assumes a constant susceptibility difference between blood and tissue but the presence of iron results in microscopic susceptibility changes extending over less than one voxel which the susceptibility correction method cannot handle.
Another major confounding effect conferred from $T2^*$ maps to rOEF maps which is independent from the oxygenation status of tissue is the structural impact of white matter. Assuming the two extreme values for $T2^*$, 52.7 ms in the case of fibers parallel to the main field and 47.2 ms for perpendicular fibers (see Fig. 5.1.1), rOEF is 0.64 or 0.88, respectively (with $T2 = 76.5$ ms and rCBV$= 2.9\%$, taken from Table 4.4.1), which is a difference of 38%. A large amount of fibers perpendicular to the field in white matter and a corresponding orientation of microvessels along fiber tracts can explain the quite large difference between white and gray matter rOEF because in this case the model assumption of random vessel orientation is not satisfied in white matter. Such anatomical factors must be taken into account in a visual inspection of rOEF maps.

Brain tumor patients. If an MR-based method for the detection of hypoxia is to be of any use, it should be able to identify hypoxic spots within high-grade brain tumors whose existence was proven in previous in vitro and preclinical studies, also in the framework requirements of a clinical patient examination. Evidence for the feasibility of the method was obtained in the study on tumor patients: Whole-brain rOEF maps of diagnostic quality were acquired with acceptable acquisition times. Comparison to immunohistochemistry results was performed as described below. It was found that rOEF is correlated with tumor malignancy. Hypoxic niches within vital tissue (where rCBV is not decreased) were identified mainly in high-grade tumors [99]. This corresponds to pathophysiological findings: Although tumors mainly consist of vital, well-perfused tissue (supported by the fact of a generally lower rOEF in tumorous tissue compared to healthy appearing gray and white matter in Fig. 4.4.3), the tissue might still not be adequately supplied with oxygen everywhere in the tumor because of dysfunctional vessel structures. In contrast-enhancing tissue, where the blood brain barrier is severely disrupted, rCBV could be quantified incorrectly with DSC. Since the model of cylindrical vessels might

also be invalid there, rOEF values in CET are subject to large uncertainty.

Stroke and stenosis patients. First results of an ongoing study on stroke and stenosis patients demonstrate the capability of the presented method for rOEF mapping to distinguish between the ischemic core and surrounding tissue. rOEF is increased in both areas compared to healthy tissue meaning that rOEF is correlated with perfusion prolongation. This effect is more pronounced in surrounding tissue, suggesting potentially reversible metabolic function in areas with a distinct rOEF increase. rOEF in the ischemic core itself does not need to be increased; it can also be 0: An increase occurs if the blood supply to this area is interrupted by a vessel occlusion. Old blood is then depleted of oxygen which raises rOEF. In the other case, tissue might still be sufficiently supplied with oxygen but if it has already perished, no oxygen will be extracted from the blood. Further evaluations on the stroke study data will focus on the prognostic value of rOEF mapping compared to the most widely used DWI/PWI mismatch method [25–28] and the suitability of rOEF to mark the penumbra.

5.4.4 Validation by Other Modalities

The results from most of the tested biopsy samples confirmed the results from the MR method. Immunohistochemical methods permit observations on the hypoxic or normoxic state of the tissue sample with the three grades corresponding to no staining, weak and strong staining of the marker but quantitative statements about the oxygen extraction fraction are not possible. Also, samples can only be obtained in tumorous tissue of selected patients that need to undergo surgery.

Another possibility for validation is PET which additionally allows for an actual quantification of the oxygen extraction fraction. The best investigated radiotracer for PET hypoxia imaging is 18F-FMISO [132] which exclusively accumulates in vital, hypoxic cell structures. The major limitation of PET is its low SNR. Still, 18F-FMISO has been used to identify hypoxic areas in glioma patients with the result of confirming the correlation between a high uptake of 18F-FMISO and high tumor grade as well as a more negative patient outcome [133].

For the purpose of a systematic validation of the MR method, the presented protocol for rOEF mapping has been transferred to the mMR Biograph, a hybrid MR-PET scanner, where it is currently being applied on brain tumor patients simultaneously to an 18F-FMISO examination. Additionally all patients will be biopsied. Results are still pending.

6 Conclusion

A clinically feasible approach to map the oxygen extraction fraction in the brain with magnetic resonance imaging based on magnetic susceptibility differences of oxygenated and deoxygenated blood was explored in this work. Fast multi-slice imaging for $T2$ and $T2^*$ quantification and a routine DSC scan for CBV quantification were used for this purpose. The additional acquisition time for whole-brain mapping of $T2$ and $T2^*$ is 6.5 minutes.
While a major bias due to stimulated echo influences or diffusion effects could be excluded for GRASE $T2$ measurements by means of simulations and phantom studies, artifact corrections for background gradients and motion were found to be necessary in the post-processing of multi-gradient echo $T2^*$ data. Both $T2$ and $T2^*$ quantification yielded reproducible values within literature range in different groups of healthy volunteers, brain tumor and stroke patients.
Several approaches were tested for CBV quantification. Perfusion imaging with DSC turned out to be the most robust method for patient measurements. It is routinely included in clinical protocols of tumor or stroke examinations and does not take up any additional time.

Relative maps of the oxygen extraction fraction were calculated from $T2$, $T2^*$ and relative CBV. The examined method was found to facilitate whole-brain mapping of rOEF with diagnostic quality, suitable for the detection of hypoxic niches in brain tumors and capable of differentiating between heterogenous tissue types in tumorous and stroke affected tissue.

The method is constrained to relative quantification because of inaccuracies in the measurements of the required input parameters mainly due to partial volume effects and strong local background gradients and because of model simplifications and assumptions that might not be satisfied everywhere in the brain. An exemplary challenge is the directional white matter structure which probably violates the assumption of random blood vessel directions.

Since other effects, e.g. magnetic field perturbations or severe pathological tissue alterations, can also lead to apparently high rOEF, artificially increased values of the relative oxygen extraction fraction complicate a correct interpretation of the maps. However, such artifacts can be identified and excluded from further analysis by additional consideration of data from the standard clinical protocol that is routinely performed for patients. Artifact examples are necrotic tissue and bleeding spots that both appear bright in the rOEF map but can be identified as part of the non-enhancing tumor core in an MPRAGE image or as dark spots in a high resolution $T2^*$-weighted FFE image, respectively.

A practicable, standardized and, because it provides relative quantification, also comparable protocol to detect differences in the oxygen extraction fraction has been developed and tested in clinical studies. Preliminary validation using immunohistochemical methods showed promising results. A comprehensive validation with both histology and 18F-FMISO PET is currently starting. The next step is to expand the method by profound, suitable model modifications in order to enable true, absolute quantification in the clinical environment, which would highly benefit patient-individual diagnostics.

Appendix

A.1 The Physics of Magnetic Resonance

A.1.1 Nuclear Spin and Nuclear Magnetic Resonance

The physics of the interaction of a magnetic dipole with an external magnetic field, which is the basis of nuclear magnetic resonance (NMR), are described e.g. in Refs. [134], [67] or [135].
Nuclei with an odd number of nucleons (i.e. protons and neutrons) possess an intrinsic angular momentum called the nuclear spin $\boldsymbol{I}$, a corresponding half-integer spin quantum number I, and a magnetic moment $\boldsymbol{\mu}$ which is linked to the spin by the proportionality constant γ,

$$\boldsymbol{\mu} = \gamma \boldsymbol{I} \tag{A.1.1}$$

γ is called the gyromagnetic ratio and has a specific value for each nucleus. Its value for hydrogen nuclei, the protons, is $\gamma/(2\pi) = 42.577$ MHz/T. Protons have the greatest gyromagnetic ratio of all stable isotopes and are the most abundant half-integer spin particles in biological tissue. That is the reason why most magnetic resonance imaging is performed on ^{1}H nuclei of the water contained in the tissue.
The z component of the spin $\boldsymbol{I}$ in units of $\hbar$ is called the magnetic quantum number $m = -I, -I+1, \ldots, I$. Knowledge of I and m is sufficient to fully characterize a spin state.

A magnetic moment $\boldsymbol{\mu}$ interacts with a magnetic field $\boldsymbol{B}$ in a way described by the Hamiltonian H,

$$H = -\boldsymbol{\mu} \cdot \boldsymbol{B} = -\gamma \, \boldsymbol{I} \cdot \boldsymbol{B} \tag{A.1.2}$$

The Hamiltonian applied to a state $|I, m\rangle$ yields its energy level

$$H\,|I, m\rangle = E_\mathrm{m}\,|I, m\rangle \tag{A.1.3}$$

In the case of a $\boldsymbol{B}$ field in z direction, $E_\mathrm{m} = -\gamma\hbar m\,B_z$. Due to $(2\,I+1)$ possibilities for the spin to orient itself in the $\boldsymbol{B}$ field, $(2\,I+1)$ energy levels of the particle exist with a difference

$$\Delta E = \gamma\,\hbar\,B_z = \hbar\omega_0 \tag{A.1.4}$$

$\omega_0 = \gamma B_z$ is the specific resonance frequency or Larmor frequency of the particle. Radiofrequency (RF) fields with the resonance frequency ω_0 are used to induce transitions between energy states. The energy that a particle radiates off when it returns to a lower state is the basis of the NMR signal.

A.1.2 Macroscopic Magnetization

The occupation probabilities p_m of the energy levels E_m in thermal equilibrium are given by Boltzmann statistics,

$$p_\mathrm{m} = \frac{1}{Z}\cdot\exp\Big(-\frac{E_\mathrm{m}}{k_\mathrm{B}T}\Big);\quad Z = \sum_{m=-I}^{I}\exp\Big(-\frac{E_\mathrm{m}}{k_\mathrm{B}T}\Big) \tag{A.1.5}$$

with the canonical partition function Z, the Boltzmann constant $k_\mathrm{B} = 1.38\cdot10^{-23}$ J/K and the temperature T. Energy levels are therefore not equally occupied, resulting in a macroscopic net magnetization $\boldsymbol{M}$. $\boldsymbol{M}$ is defined as the sum of all expectation values of the magnetic moments per volume V in an external $\boldsymbol{B}$ field,

$$\boldsymbol{M} = \frac{\sum_\mathrm{i}\langle\boldsymbol{\mu}_\mathrm{i}\rangle}{V} \tag{A.1.6}$$

The existence of a macroscopic magnetization is required for the formation of the measured RF signal in NMR experiments.

Precession in a magnetic field. In the classical picture, a magnetic dipole moment $\boldsymbol{\mu}$ in a $\boldsymbol{B}$ field experiences a torque $\boldsymbol{N} = \boldsymbol{\mu}\times\boldsymbol{B}$, or in the case of multiple magnetic moments, $\boldsymbol{N} = \boldsymbol{M}\times\boldsymbol{B}$. Since the magnetization also possesses the properties of an angular momentum due to its relation to $\boldsymbol{\mu}$ and $\boldsymbol{I}$ (see Eq. A.1.1), the torque is proportional to the change of the angular momentum $\boldsymbol{N} = \dot{\boldsymbol{I}} = 1/\gamma\cdot\dot{\boldsymbol{M}}$. Therefore the following equation

for the magnetization as the sum over all magnetic moments holds:

$$\dot{\boldsymbol{M}}(t) = \gamma \boldsymbol{M}(t) \times \boldsymbol{B}(t) \tag{A.1.7}$$

In the case of a static field $\boldsymbol{B_0}$, Eq. A.1.7 describes a precessing motion of the magnetization around the direction of the $\boldsymbol{B}_0$ field. The temporal average of $\boldsymbol{M}$ points in the direction of the $\boldsymbol{B}_0$ field.

Radiofrequency pulses and excitation. The magnetization can be manipulated by additional electromagnetic fields with the resonance frequency. According to Eq. A.1.4, the resonance frequency of protons is in the MHz range of radio waves. The protons absorb the respective energy difference and are excited to higher energy levels. If a circularly polarized field $\boldsymbol{B}_1 = B_1(\cos\omega t, \sin\omega t, 0)$ is applied perpendicular to the $\boldsymbol{B}_0$ or z direction (Fig. A.1.1 a), Eq. A.1.7 yields

$$\dot{\boldsymbol{M}}(t) = \gamma \boldsymbol{M}(t) \times (B_1 \cos\omega t, B_1 \sin\omega t, B_0) \tag{A.1.8}$$

The $\boldsymbol{B}_1$ field is constant in a frame of reference rotating with the frequency ω around the $z = z'$ axis. The equation of motion in the rotating frame is

$$\dot{\boldsymbol{M}}'(t) = \gamma \boldsymbol{M}'(t) \times (B_1, 0, B_0 - \omega/\gamma) = \gamma \boldsymbol{M}'(t) \times \boldsymbol{B}_{\text{eff}} \tag{A.1.9}$$

The magnetization $\boldsymbol{M'}$ thus precesses around an effective field $\boldsymbol{B}_{\text{eff}}$ in the rotating frame (Fig. A.1.1 b). The z' component of $\boldsymbol{B}_{\text{eff}}$ vanishes if the $\boldsymbol{B}_1$ field has the resonance frequency $\omega_0 = \gamma B_0$, resulting in a precession of $\boldsymbol{M'}$ around the x' axis.

Flip angle and transverse magnetization. A radiofrequency field $\boldsymbol{B}_1$ with the Larmor frequency of protons tilts the resulting magnetization vector from precessing around the z' axis to precessing around the $\boldsymbol{B}_1$ field axis. The opening angle of the precession cone defines the flip angle α with the z' axis: A wider opening of the cone, i.e. a smaller α results in a smaller transverse magnetization. α can be calculated from the duration of the radiofrequency pulse t_{p} as [134]

$$\alpha = \gamma\, B_1\, t_{\text{p}} \tag{A.1.10}$$

The transverse component of the tilted magnetization induces a measurable voltage in a receiver antenna oriented perpendicular to the static magnetic field.

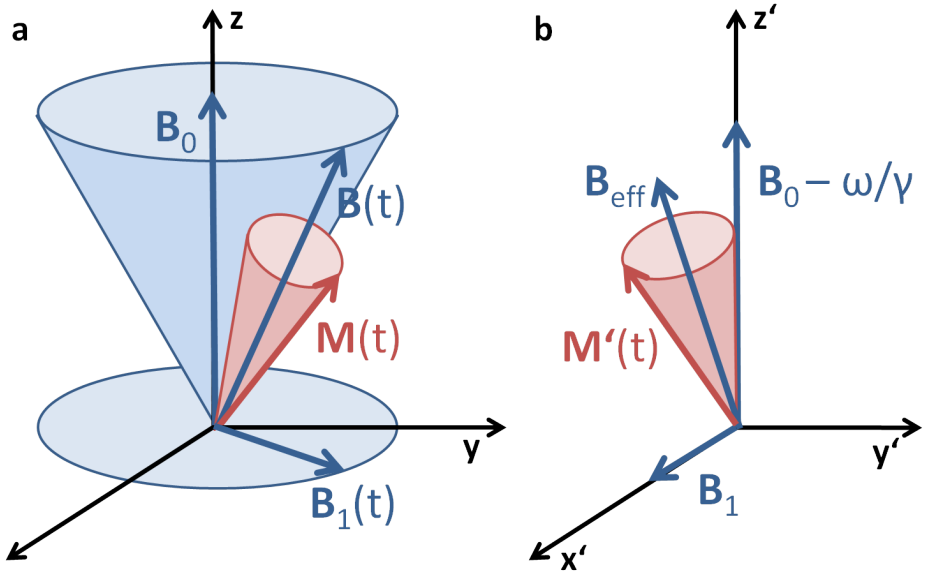

Figure A.1.1 a) Orientation of the magnetization and involved magnetic fields. $\boldsymbol{B}_0$ is the static field, $\boldsymbol{B}_1(t)$ is the circularly polarized radiofrequency field. The magnetization $\boldsymbol{M}(t)$ precesses around the resulting field $\boldsymbol{B}(t)$ which in turn precesses around $\boldsymbol{B}_0$. b) Vectors in the rotating frame. $\boldsymbol{B}_1$ is constant along the x' axis. $\boldsymbol{M'}(t)$ precesses around the effective field $\boldsymbol{B}_{\text{eff}}$. If $\boldsymbol{B}_1$ satisfies the resonance condition, $\boldsymbol{B}_{\text{eff}}$ becomes equal to $\boldsymbol{B}_1$ and the magnetization precesses around $\boldsymbol{B}_1$.

A.1.3 The Bloch Equations and Relaxation Processes

As soon as the radiofrequency pulse is turned off, the magnetization returns to thermal equilibrium by realigning itself with the static field. This process is called relaxation and is caused by interactions of the spins among each other (spin-spin relaxation) and with the surrounding lattice (spin-lattice relaxation). The respective equations of motion were found by Felix Bloch in 1946,

$$\begin{aligned}
\frac{\partial M_x(t)}{\partial t} &= \gamma\Big(\boldsymbol{M}(t) \times \boldsymbol{B}(t)\Big)_x - \frac{M_x(t)}{T2} \\
\frac{\partial M_y(t)}{\partial t} &= \gamma\Big(\boldsymbol{M}(t) \times \boldsymbol{B}(t)\Big)_y - \frac{M_y(t)}{T2} \\
\frac{\partial M_z(t)}{\partial t} &= \gamma\Big(\boldsymbol{M}(t) \times \boldsymbol{B}(t)\Big)_z - \frac{M_z(t) - M_0}{T1}
\end{aligned} \tag{A.1.11}$$

M_0 is the magnetization at equilibrium. The transverse relaxation time $T2$ describes the exponential decay of the transverse component of the magnetization due to loss in phase coherence of the precessing spins as the Brownian motion of atoms and molecules causes random, local variations of the magnetic field. The longitudinal relaxation time $T1$ describes the return of the magnetization to an orientation parallel to the static field by delivering energy of the radiofrequency pulse from the spins to the lattice as thermal energy. $T1$ and $T2$ are specific constants depending on the surrounding material. Differences in the relaxation times in biological tissues are the basis for the contrast in MR images.

Free longitudinal relaxation. After a temporary disturbance from equilibrium, the magnetization returns to its equilibrium state. The solution for the z component of the magnetization in the equation

$$\dot{M}_z(t) = \frac{1}{T1}(M_0 - M_z(t)) \tag{A.1.12}$$

is given by

$$M_z(t) = M_z(0)\exp\Big(-\frac{t}{T1}\Big) + M_0\Big(1 - \exp\Big(-\frac{t}{T1}\Big)\Big) \tag{A.1.13}$$

Often the magnetization is prepared to have a defined state at $t = 0$. If a 180° pulse is used, it is completely inverted and anti-parallel to the main

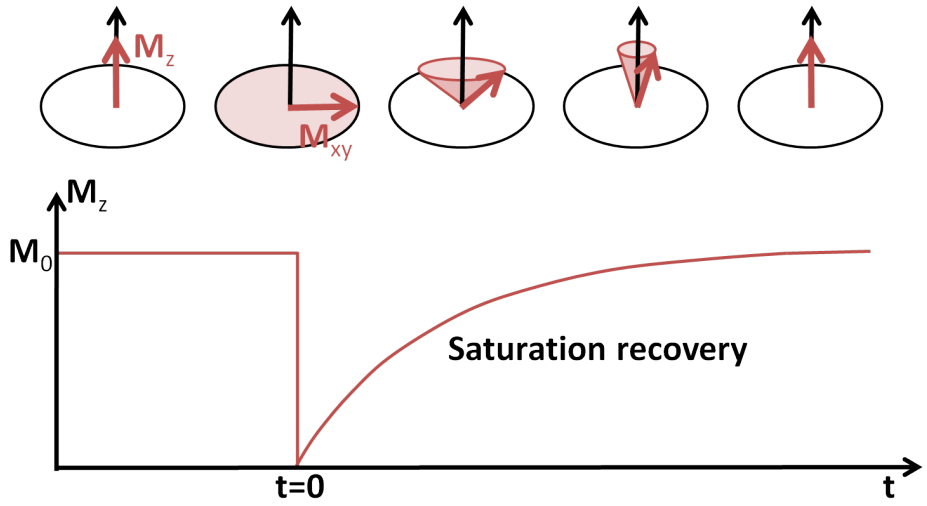

Figure A.1.2 Illustration of a saturation recovery experiment. The magnetization is rotated to the transverse plane and relaxes back to a purely longitudinal orientation.

field. Eq. A.1.13 then simplifies to

$$M_z(t) = M_0\left(1 - 2 \cdot \exp\left(-\frac{t}{T1}\right)\right) \tag{A.1.14}$$

This is called an inversion recovery experiment. Alternatively, the magnetization can be rotated to the transverse plane with a 90° pulse, where the longitudinal component is 0 (saturation recovery),

$$M_z(t) = M_0\left(1 - \exp\left(-\frac{t}{T1}\right)\right) \tag{A.1.15}$$

The development of the longitudinal magnetization for saturation recovery and the corresponding signal is shown in Fig. A.1.2.

Free transverse relaxation. Right after RF excitation the transverse part of the magnetization needs to satisfy the equation of motion

$$\dot{M}_{xy}(t) = -\frac{1}{T2}M_{xy}(t) \tag{A.1.16}$$

with the solution

$$M_{xy}(t) = M_{xy}(0)\exp\left(-\frac{t}{T2}\right) \tag{A.1.17}$$

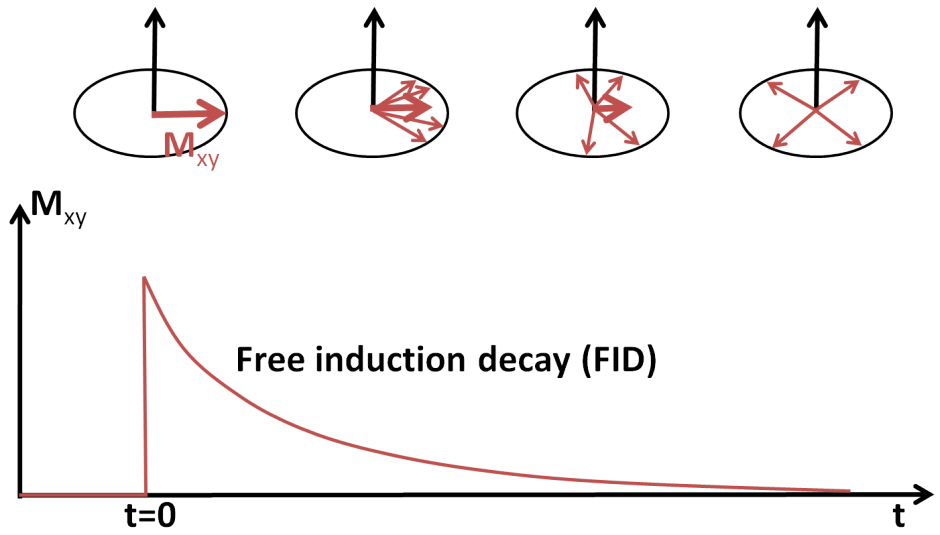

Figure A.1.3 As the spins are dephasing, the resulting transverse magnetization is decreasing. Thin arrows represent macroscopic magnetic moments consisting of an ensemble of nuclear magnetic moments precessing in phase.

The temporal development of the signal is called free induction decay (FID) and is illustrated in Fig. A.1.3. Right after being flipped by a radiofrequency pulse, the spins have the same phase because the induced transitions between energy levels are phase coherent to the transmitted field. Due to their mutual interactions they lose their phase coherence and start to fan out. As a result the transverse magnetization decays. The respective relaxation time constant $T2$ is a measure for the strength of interactions between the spins.

In reality the static main magnetic field $\boldsymbol{B}_0$ is never completely homogeneous. Technical inhomogeneities, susceptibility differences in biological tissues, contrast agents and the blood oxygenation level all lead to local variations in the field and thus in the resonance frequency and consequently speed up the dephasing of the spins. Therefore the free induction decay is actually governed by an effective transverse relaxation time $T2^*$ which is shorter than $T2$.

A.2 Magnetic Resonance Imaging

A.2.1 Magnetic Field Gradients and Spatial Encoding

As explained in Section A.1.2, the transverse component of the precessing magnetization produces the MR signal. However, this signal contains no

spatial information about the spins responsible for it. To introduce a spatial dependence, magnetic fields in the same direction as the static field but with varying strength in spatial directions

$$\boldsymbol{G}(\boldsymbol{r},t) = \Big(\frac{\partial B_z(\boldsymbol{r})}{\partial x}, \frac{\partial B_z(\boldsymbol{r})}{\partial y}, \frac{\partial B_z(\boldsymbol{r})}{\partial z}\Big) \tag{A.2.1}$$

are used. These gradients make the total magnetic field dependent on the position $\boldsymbol{r}$,

$$\boldsymbol{B}(\boldsymbol{r},t) = \boldsymbol{B}_0 + \Big(\boldsymbol{r}\cdot\boldsymbol{G}(\boldsymbol{r},t)\Big)\boldsymbol{e}_z \tag{A.2.2}$$

The spin density can thus be inferred from the also spatially dependent resonance frequency $\omega(\boldsymbol{r},t) = \gamma\boldsymbol{B}(\boldsymbol{r},t)$.

Slice selection. To restrict the signal to originate only from a slice of a defined thickness d in an extended object, a gradient is applied in the z direction (slice selection gradient). This varies the resonance frequency along z, so that a radiofrequency pulse with a bandwidth $\Delta\omega$ can excite spins only in the respective slice (Fig. A.2.1).

Phase encoding. Before the readout the spins in the selected slice are equipped with a constant phase depending on their y position. This is achieved by switching on a gradient in the y direction which speeds the precession up or slows it down (phase encoding gradient). After the gradient is switched off, all spins again precess with the resonance frequency but have gained an additional phase,

$$\varphi(y) = \gamma\int_0^t G_y(\tau)y\,\mathrm{d}\tau \tag{A.2.3}$$

Frequency encoding. An additional gradient in x direction (readout gradient) during the acquisition causes the spins in the selected slice to precess with different frequencies depending on their x coordinates. The portion of the signal with a frequency $\omega(\tilde{x})$ corresponds to the $\tilde{x}$ position in the slice. The principle of spatial encoding is illustrated in Fig. A.2.2.

Multi-slice and 3D acquisitions. A volume is imaged by either repeating the previously described encoding process for all slices separately (multi-slice) or by exciting a whole partition and performing an additional phase-encoding in the partition direction (3D).

A.2.2 Image Readout and Reconstruction

The contrast in MR images is created by the different time constants that characterize the relaxation and dephasing of the spins due to the varying

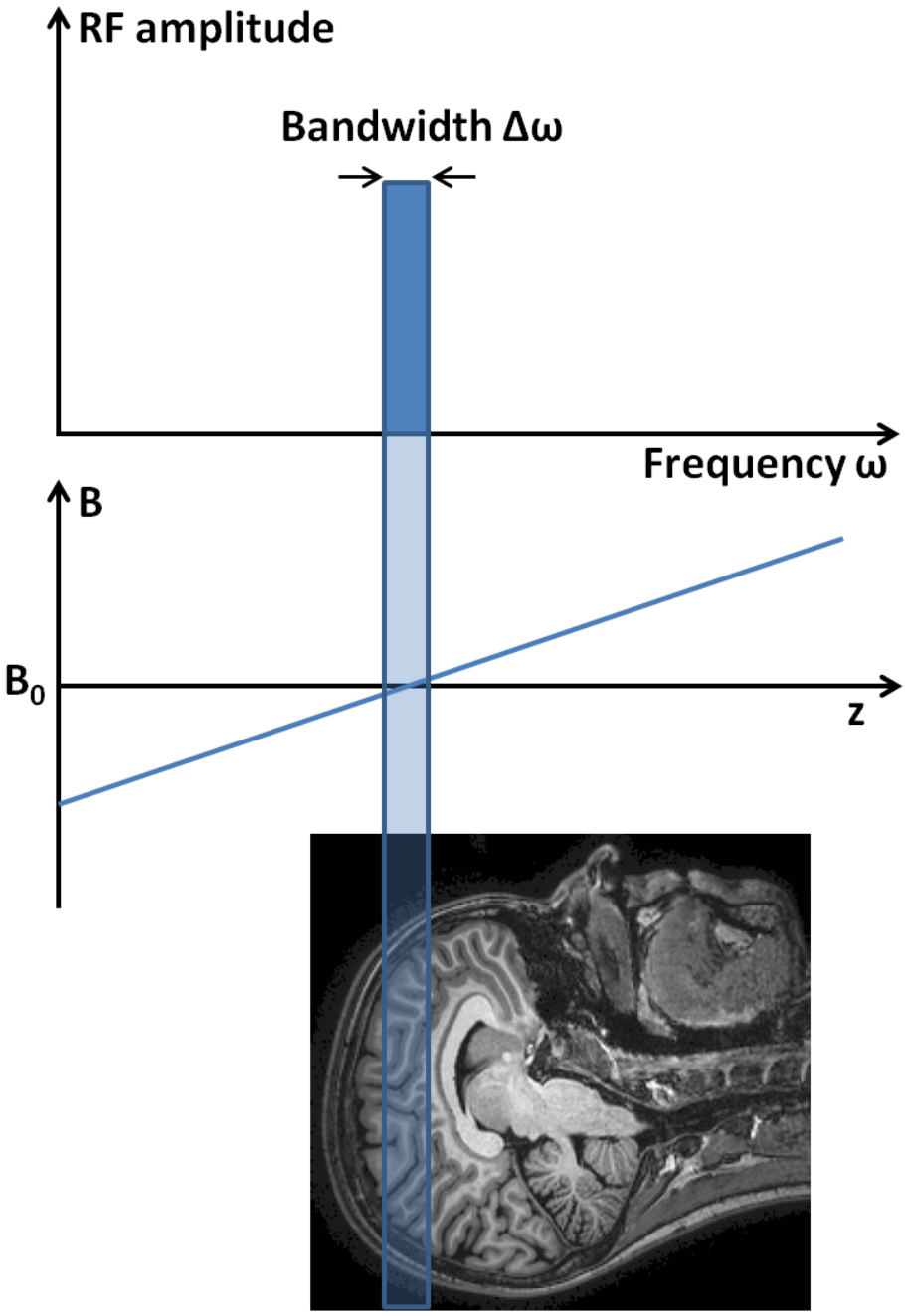

Figure A.2.1 A slice is selected by varying the magnetic field with the help of a gradient in z direction. Only spins in this slice have the resonance frequency $\omega_0 \pm 1/2\,\Delta\omega$.

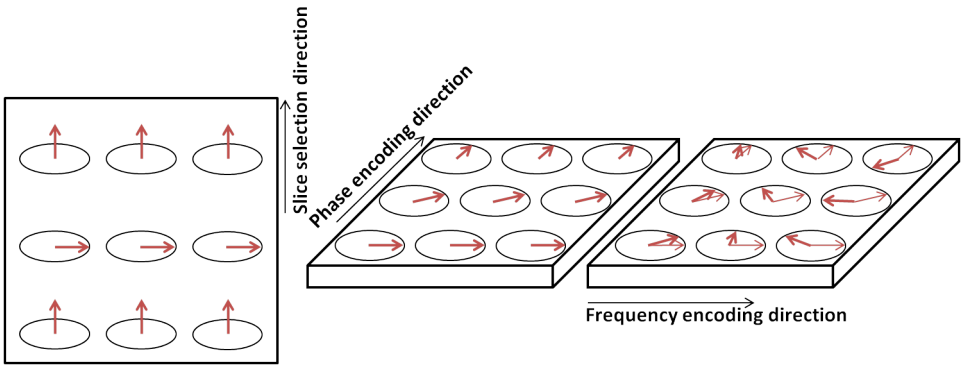

Figure A.2.2 Principle of spatial encoding in MRI. The frequency of the excitation pulse is matched to the resonance frequency of the spins in a particular slice by adding a slice selection gradient to the main magnetic field. Those spins are flipped to the transverse plane. Their precession frequencies are changed in two directions by the phase and frequency encoding gradients. Each frequency component of the signal therefore corresponds to a particular location.

interaction strength depending on the tissue environment. However, completely dephased spins produce no signal as the resulting magnetization is 0. Two mechanisms exist to bring the spins back in phase after letting them dephase for some time: Refocusing with the help of gradients resulting in the formation of gradient echoes, and refocusing by RF pulses which are used to form spin echoes. A detailed description of these processes is given in Sections 2.2 and 2.3.

Image Contrast

Different types of contrast are possible in MR measurements, $T1$-weighted, $T2$-weighted, proton density-weighted or mixed-weighted contrast, depending on the selected values for TE and TR. Since both $T1$ and $T2$ relaxation happen simultaneously, the magnetization develops as

$$\begin{aligned} M(TE,TR) =& M_z(0)\exp\left(-\frac{TR}{T1}\right)\exp\left(-\frac{TE}{T2}\right) \\ &+ M_0\left(1-\exp\left(-\frac{TR}{T1}\right)\right)\exp\left(-\frac{TE}{T2}\right) \end{aligned} \tag{A.2.4}$$

Depending on the values for TE and TR compared to $T2$ and $T1$, some terms in Eq. A.2.4 are close to 0 or close to 1 and the dependence on $T1$ or $T2$ vanishes. For example, if TE is a lot smaller than $T2$ and TR is comparable to $T1$, the dependence on $T2$ vanishes and the signal only depends on $T1$, making the images $T1$-weighted. Only the different $T1$

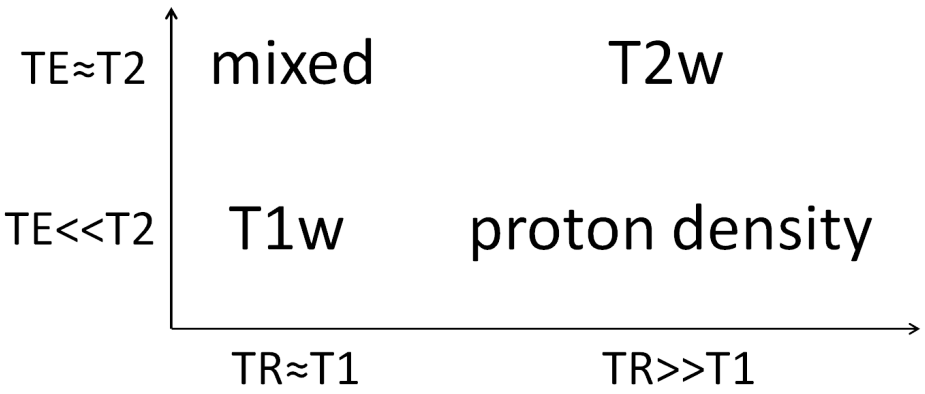

Figure A.2.3 Image contrast depending on the chosen values for TE and TR.

times of the tissue determine the image contrast. If on the other hand TE is a lot smaller than $T2$ but TR is a lot greater than $T1$, the signal is proportional to the magnetization in equilibrium, M_0. In this case the contrast is proton density-weighted (Fig. A.2.3).

k-space Formalism

Since the receiver coil is sensitive to the precession frequency of the magnetization, the collected signal also has a frequency representation. This concept is called k-space. The coordinates in k-space are

$$k_x(t) = \gamma \int_0^t G_x(\tau)\mathrm{d}\tau; \qquad k_y(t) = \gamma \int_0^t G_y(\tau)\mathrm{d}\tau \tag{A.2.5}$$

G_x and G_y are the magnetic field gradients for spatial encoding in the respective directions. The representation of the signal in k-space is the inverse Fourier transform of the transverse magnetization in the rotating frame

$$\begin{aligned} S(k_x,k_y) &= \int_{\text{slice}} \left|M_{xy}(x,y,t)\right| \, \mathrm{e}^{\mathrm{i}\varphi} \, \mathrm{d}x \, \mathrm{d}y \\ &= \int_{\text{slice}} \left|M_{xy}(x,y,t)\right| \, \mathrm{e}^{\mathrm{i}\left(\gamma \int_0^t G_x(\tau)x \, \mathrm{d}\tau + \gamma \int_0^t G_y(\tau)y \, \mathrm{d}\tau\right)} \mathrm{d}x \, \mathrm{d}y \\ &= \int_{\text{slice}} \left|M_{xy}(x,y,t)\right| \, \mathrm{e}^{\mathrm{i}\left(k_x(t)x + k_y(t)y\right)} \, \mathrm{d}x \, \mathrm{d}y \end{aligned} \tag{A.2.6}$$

The measured signal $S(k_x,k_y)$ contains the the magnitude and phase information of M_{xy} at the time t. Transferring this information into image

space is again performed via a Fourier transform,

$$M_{xy}(x,y) = \frac{1}{(2\pi)^2} \int \left|S(k_x,k_y)\right| \, \mathrm{e}^{-\mathrm{i}(k_x x + k_y y)} \, \mathrm{d}k_x \, \mathrm{d}k_y \tag{A.2.7}$$

$M_{xy}(x,y)$ is a complex number with magnitude and phase information that can both be reconstructed.
In the case of 3D acquisitions with an additional phase encoding direction the k-space formalism is extended to three dimensions.

List of Figures

List of Tables

List of Abbreviations

ASL	arterial spin labeling
BOLD	blood oxygenation level dependent
CBV	cerebral blood volume
CET	contrast enhancing tissue
CPMG	Carr-Purcell-Meiboom-Gill
CSF	cerebrospinal fluid
dCBV	deoxygenated cerebral blood volume
DCE	dynamic contrast enhanced
DSC	dynamic susceptibility contrast
DTI	diffusion tensor imaging
DWI	diffusion-weighted imaging
EES	extravascular extracellular space
EPG	extended phase graph
EPI	echo planar imaging
FA	fractional anisotropy
FFE	fast field echo
18F-FMISO	(18)F-fluoromisonidazole
FID	free induction decay
FLAIR	fluid-attenuated inversion recovery
FLASH	fast low angle shot
Gd-DTPA	gadolinium diethylene-triamine-pentacetate
GESSE	gradient echo sampling of a spin echo
GM	gray matter
GRAPPA	generalized autocalibrating, partially parallel acquisition
GRASE	gradient echo-spin echo
HGG	high-grade glioma
HIF1α	hypoxia-inducible factor 1α
IR	inversion recovery
ISF	interstitial fluid
MPRAGE	magnetization-prepared rapid acquisition of gradient echo
MR	magnetic resonance
MRI	magnetic resonance imaging

NMR	nuclear magnetic resonance
OEF	oxygen extraction fraction
PET	positron emission tomography
PWI	perfusion-weighted imaging
qBOLD	quantitative blood oxygenation level dependent
rCBV	relative cerebral blood volume
RF	radio frequency
rOEF	relative oxygen extraction fraction
ROI	region of interest
SE-EPI	spin echo echo planar imaging
SENSE	sensitivity encoding
SNR	signal to noise ratio
SR	saturation recovery
tCBV	total cerebral blood volume
TFE	turbo field echo
TTP	time to peak
TSE	turbo spin echo
QUIXOTIC	quantitative imaging of extraction of oxygen and tissue consumption
USPIO	ultrasmall superparamagnetic iron oxide
VASO	vascular space occupancy
vCBV	venous CBV
VOI	volume of interest
WM	white matter

References

[1] Derdeyn CP, Videen TO, Yundt KD, et al. Variability of cerebral blood volume and oxygen extraction: stages of cerebral haemodynamic impairment revisited. *Brain*, 125:595 – 607, 2002. PubMed: 11872616, doi: 10.1093/brain/awf047.

[2] Iadecola C. Neurovascular regulation in the normal brain and in Alzheimer's disease. *Nat Rev Neurosci*, 5:347 – 60, 2004. PubMed: 15100718, doi: 10.1038/nrn1387.

[3] Iadecola C. Rescuing troubled vessels in Alzheimer disease. *Nat Med*, 11:923 – 924, 2005. PubMed: 16145570, doi: 10.1038/nm0905-923.

[4] Vlassenko AG, Vaishnavi SN, Couture L, et al. Spatial correlation between brain aerobic glycolysis and amyloid-beta (Abeta) deposition. *Proc Natl Acad Sci USA*, 107:17 763 – 17 767, 2010. PubMed: 20837517, doi: 10.1073/pnas.1010461107.

[5] Powers WJ, Videen TO, Markham J, et al. Selective defect of in vivo glycolysis in early Huntington's disease striatum. *Proc Natl Acad Sci USA*, 104:2945 – 49, 2007. PubMed: 17299049, doi: 10.1073/pnas.0609833104.

[6] Beal MF. Mitochondrial dysfunction in neurodegenerative diseases. *Biochim Biophys Acta*, 1366:211 – 23, 1998. PubMed: 9714810.

[7] Tatum JL, Kelloff GJ, Gillies RJ, et al. Hypoxia: importance in tumor biology, noninvasice measurement by imaging, and value of its measurement in the management of cancer therapy. *Int J Radiat Biol*, 82:699 – 757, 2006. PubMed: 17118889, doi: 10.1080/09553000601002324.

[8] Davda S and Bezabeh T. Advances in methods for assessing tumor hypoxia in vivo: implications for treatment planning. *Can-*

cer Metastasis Rev, 25:469 – 80, 2006. PubMed: 17029029, doi: 10.1007/s10555-006-9009-z.

[9] Steinke B. Maligne Gliome. Leitlinien: Empfehlungen der DGHO für die Diagnostik und Therapie hämatologischer und onkologischer Erkrankungen: Deutsche Gesellschaft für Hämatologie und Onkologie. 2009.

[10] Scherer HJ. The forms of growth in gliomas and their practical significance. *Brain*, 63:1 – 35, 1940. doi: 10.1093/brain/63.1.1.

[11] Beier D, Hau P, Proescholdt M, et al. CD133(+) and CD133(-) glioblastoma-derived cancer stem cells show differential growth characteristics and molecular profiles. *Cancer Res*, 67:4010 – 15, 2007. PubMed: 17483311, doi: 10.1158/0008-5472.CAN-06-4180.

[12] Heddleston JM, Li Z, McLendon RE, et al. The hypoxic microenvironment maintains glioblastoma stem cells and promotes reprogramming towards a cancer stem cell phenotype. *Cell Cycle*, 8:3274 – 82, 2009. PubMed: 19770585, doi: 10.4161/cc.8.20.9701.

[13] Rieger J, Bähr O, Müller K, et al. Bevacizumab-induced diffusion restricted lesions in malignant glioma patients. *J Neurooncol*, 99:49 – 56, 2010. PubMed: 20035366, doi: 10.1007/s11060-009-0098-8.

[14] Sathomsumetee S, Cao Y, Marcello JE, et al. Tumor angiogenic and hypoxic profiles predict radiographic response and survival in malignant astrocytoma patients treated with bevacizumab and irinotecan. *J Clin Oncol*, 26:271 – 78, 2008. PubMed: 18182667, doi: 10.1200/JCO.2007.13.3652.

[15] Bergers G and Hanahan D. Modes of resistance to anti-angiogenic therapy. *Nat Rev Cancer*, 8:592 – 603, 2008. PubMed: 18650835, doi: 10.1038/nrc2442.

[16] Eckerich C, Zapf S, Fillbrandt R, et al. Hypoxia can induce c-Met expression in glioma cells and enhance SF/HGF-induced cell migration. *Int J Cancer*, 121:276 – 83, 2007. PubMed: 17372907, doi: 10.1002/ijc.22679.

[17] Gray LH, Conger AD, Ebert M, et al. The concentration of oxygen dissolved in tissues at the time of irradiation as a factor in radiotherapy. *Br J Radiol*, 26:638 – 48, 1953. PubMed: 13106296.

[18] Brown JM and Wilson WR. Exploiting tumour hypoxia in cancer treatment. *Nat Rev Cancer*, 4:437 – 47, 2004. PubMed: 15170446, doi: 10.1038/nrc1367.

[19] Wilson WR and Hay MP. Targeting hypoxia in cancer therapy. *Nat Rev Cancer*, 11:393 – 410, 2011. PubMed: 21606941, doi: 10.1038/nrc3064.

[20] Jensen RL. Brain tumor hypoxia: tumorigenesis, angiogenesis, imaging, pseudoprogression, and as a therapeutic target. *J Neurooncol*, 92:317 – 35, 2009. PubMed: 19357959, doi: 10.1007/s11060-009-9827-2.

[21] Yamauchi H, Fukuyama H, Nagahama Y, et al. Evidence of misery perfusion and risk for recurrent stroke in major cerebral arterial occlusive diseases from PET. *J Neurol Neurosurg Psychiatry*, 61:18 – 25, 1996. PubMed: 8676151.

[22] Grubb RL Jr, Derdeyn CP, Fritsch SM, et al. Importance of hemodynamic factors in the prognosis of symptomatic carotid occlusion. *Magn Reson Med*, 29:139 – 44, 1993. PubMed: 8419736.

[23] Baron JC. Mapping the ischaemic penumbra with PET: implications for acute stroke treatment. *Cerebrovasc Dis*, 9:193 – 201, 1999. PubMed: 10393405, doi: 10.1159/000015955.

[24] Astrup J, Siesjo BK, and Symon L. Thresholds in cerebral ischemia - the ischemic penumbra. *Stroke*, 12:723 – 25, 1981. PubMed: 6272455, doi: 10.1161/01.STR.12.6.723.

[25] Guadagno JV, Warburton EA, Aigbirhio FI, et al. Does the acute diffusion-weighted imaging lesion represent penumbra as well as core? A combined quantitative PET/MRI voxel-based study. *J Cereb Blood Flow Metab*, 11:1249 – 54, 2004. PubMed: 15545920, doi: 10.1097/01.WCB.0000141557.32867.6B.

[26] Sobesky J, Weber OZ, Lehnhardt FG, et al. Does the mismatch match the penumbra? Magnetic resonance imaging and positron emission tomography in early ischemic stroke. *Stroke*, 36:980 – 85, 2005. PubMed: 15790950, doi: 10.1161/01.STR.0000160751.79241.a3.

[27] Abate MG, Trivedi M, Fryer TD, et al. Early derangements in oxygen and glucose metabolism following head in-

jury: The ischemic penumbra and pathophysiological heterogeneity. *Neurocrit Care*, 9:319 – 25, 2008. PubMed: 18563636, doi: 10.1007/s12028-008-9119-2.

[28] Heiss WD. Identifying thresholds for penumbra and irreversible tissue damage. *Stroke*, 35:2671 – 74, 2004. PubMed: 15459433, doi: 10.1161/01.STR.0000143329.81997.8a.

[29] Baron JC, Bousser MG, Rey A, et al. Reversal of focal "misery-perfusion syndrome" by extra-intracranial arterial bypass in hemodynamic cerebral ischemia. A case study with 15O positron emission tomography. *Stroke*, 12:454 – 59, 1981. PubMed: 6976022, doi: 10.1161/01.STR.12.4.454.

[30] Markus R, Reutens DC, Kazui S, et al. Hypoxic tissue in ischaemic stroke: persistence and clinical consequences of spontaneous survival. *Brain*, 127:1427 – 36, 2004. PubMed: 15130953, doi: 10.1093/brain/awh162.

[31] Raichle ME and Mintun MA. Brain work and brain imaging. *Annu Rev Neurosci*, 29:449 – 76, 2006. PubMed: 16776593, doi: 10.1146/annurev.neuro.29.051605.112819.

[32] Leenders KL, Perani D, Lammertsma AA, et al. Cerebral blood flow, blood volume and oxygen utilization: normal values and effect of age. *Brain*, 113:27 – 47, 1990. PubMed: 2302536, doi: 10.1093/brain/113.1.27.

[33] Bar EE, Lin A, Mahairaki V, et al. Hypoxia increases the expression of stem-cell markers and promotes clonogenicity in glioblastoma neurospheres. *Am J Pathol*, 177:1491 – 1502, 2010. PubMed: 20671264, doi: 10.2353/ajpath.2010.091021.

[34] Schenck JF. Magnetic resonance imaging of brain iron. *J Neurol Sci*, 207:99 – 102, 2003. PubMed: 12614939, doi: 10.1016/S0022-510X(02)00431-8.

[35] Schenck JF and Zimmerman EA. High-field magnetic resonance imaging of brain iron: birth of a biomarker? *NMR Biomed*, 17:433 – 45, 2004. PubMed: 15523705, doi: 10.1002/nbm.922.

[36] Haacke EM, CHeng NY, House MJ, et al. Imaging iron stores in the brain using magnetic resonance imaging. *Magn Reson Imaging*, 23:1 – 25, 2005. PubMed: 15733784, doi: 10.1016/j.mri.2004.10.001.

[37] Tofts P (Editor). *Quantitative MRI of the Brain*. John Wiley & Sons Ltd, 1st edition, 2004.

[38] Pauling L and Coryell C. The magnetic properties and structure of hemoglobin, oxyhemoglobin and carbonmonoxyhemoglobin. *Proc Natl Acad Sci USA*, 22:210 – 16, 1936. PubMed: 16577697.

[39] Spees WM, Yablonskiy DA, Oswood MC, et al. Water proton MR properties of human blood at 1.5 Tesla: magnetic susceptibility, T(1), T(2), T*(2), and non-Lorentzian signal behavior. *Magn Reson Med*, 45:533 – 42, 2001. PubMed: 11283978, doi: 10.1002/mrm.1072.

[40] Jain V, Abdulmalik O, Propert KJ, et al. Investigating the magnetic susceptibility properties of fresh human blood for noninvasive oxygen saturation quantification. *Magn Reson Med*, 68:863 – 67, 2012. PubMed: 22162033, doi: 10.1002/mrm.23282.

[41] Ogawa S, Lee T, Kay A, et al. Brain magnetic resonance imaging with contrast dependent on blood oxygenation. *Proc Natl Acad Sci USA*, 87:969 – 72, 1990. PubMed: 2124706.

[42] Ogawa S, Tank D, Menon R, et al. Intrinsic signal changes accompanying sensory stimulation: functional brain mapping with magnetic resonance imaging. *Proc Natl Acad Sci USA*, 89:5951 – 55, 1992. PubMed: 1631079.

[43] Frahm J, Merboldt KD, and Hanicke W. Functional MRI of human brain activation at high spatial resolution. *Magn Reson Med*, 29:139 – 44, 1993. PubMed: 8419736.

[44] Boxerman JL, Hamberg LM, Rosen BR, et al. MR contrast due to intravascular magnetic susceptibility perturbations. *Magn Reson Med*, 34:555 – 66, 1995. PubMed: 8524024, doi: 10.1002/mrm.1910340412.

[45] He X and Yablonskiy DA. Quantitative BOLD: mapping of human cerebral deoxygenated blood volume and oxygen extraction fraction: default state. *Magn Reson Med*, 57:115 – 26, 2007. PubMed: 17191227, doi: 10.1002/mrm.21108.

[46] Yablonskiy DA, Sukstanskii AL, and He X. Blood oxygenation level-dependent (BOLD)-based techniques for the quantification of brain hemodynamic and metabolic properties - theoretical models and experimental approaches. *NMR Biomed*, Epub ahead of print, 2012. PubMed: 22927123, doi: 10.1002/nbm.2839.

[47] Oja JM, Gillen JS, Kauppinen RA, et al. Determination of oxygen extraction ratios by magnetic resonance imaging. *J Cereb Blood Flow Metab*, 19:1289 – 95, 1999. PubMed: 10598932, doi: 10.1097/00004647-199912000-00001.

[48] Christen T, Bolar DS, and Zaharchuk G. Imaging brain oxygenation with MRI using blood oxygenation approaches: methods, validation and clinical applications. *AJNR Am J Neuroradiol*, Epub ahead of print, 2012. PubMed: 22859287, doi: 10.3174/ajnr.A3070.

[49] Yablonskiy DA and Haacke EM. Theory of NMR signal behavior in magnetically inhomogeneous tissues: the static dephasing regime. *Magn Reson Med*, 32:749 – 63, 1994. PubMed: 7869897.

[50] Christen T, Lemasson B, Pannetier N, et al. Evaluation of a quantitative blood oxygenation level-dependent (qBOLD) approach to map local blood oxygen saturation. *NMR Biomed*, 24:393 – 403, 2011. PubMed: 20960585, doi: 10.1002/nbm.1603.

[51] Yablonskiy DA. Quantitation of intrinsic magnetic susceptibility-related effects in a tissue matrix. Phantom study. *Magn Reson Med*, 39:417 – 28, 1998. PubMed: 9498598.

[52] He X, Zhu M, and Yablonskiy DA. Validation of oxygen extraction fraction measurement by qBOLD technique. *Magn Reson Med*, 60:882 – 88, 2008. PubMed: 18816808, doi: 10.1002/mrm.21719.

[53] An H and Lin W. Quantitative measurements of cerebral blood oxygen saturation using magnetic resonance imaging. *J Cereb Blood Flow Metab*, 20:1225 – 36, 2000. PubMed: 10950383, doi: 10.1097/00004647-200008000-00008.

[54] Raichle ME, MacLeod AM, Snyder AZ, et al. A default mode of brain function. *Proc Natl Acad Sci USA*, 98:676 – 82, 2001. PubMed: 11209064, doi: 10.1073/pnas.98.2.676.

[55] Carpenter DA, Grubb RL Jr, Tempel LW, et al. Cerebral oxygen metabolism after aneurysmal subarachnoid hemorrhage. *J Cereb Blood Flow Metab*, 11:837 – 44, 1991. PubMed: 1874816, doi: 10.1038/jcbfm.1991.143.

[56] Yamauchi H, Fukuyama H, Nagahama Y, et al. Significance of increased oxygen extraction fraction in five-year prognosis of major cerebral arterial occlusive diseases. *J Nucl Med*, 40:1992 – 98, 1999. PubMed: 10616876.

[57] Diringer MN, Yundt K, Videen TO, et al. No reduction in cerebral metabolism as a result of early moderate hyperventilation following severe traumatic brain injury. *J Neurosurg*, 92:7 – 13, 2000. PubMed: 10616076.

[58] Sedlacik J and Reichenbach JR. Validation of quantitative estimation of tissue oxygen extraction fraction and deoxygenated blood volume fraction in phantom and in vivo experiments by using MRI. *Magn Reson Med*, 63:910 – 21, 2010. PubMed: 20373392, doi: 10.1002/mrm.22274.

[59] Christen T, Zaharchuk G, Pannetier N, et al. Quantitative MR estimates of blood oxygenation based on T2*: a numerical study of the impact of model assumptions. *Magn Reson Med*, 67:1458 – 68, 2011. PubMed: 22183768, doi: 10.1002/mrm.23094.

[60] Christen T, Lemasson B, Pannetier N, et al. Is T2* enough to assess oxygenation? Quantitative blood oxygen level-dependent analysis in brain tumor. *Radiology*, 262:495 – 502, 2012. PubMed: 22156990, doi: 10.1148/radiol.11110518.

[61] Hahn EL. Spin Echoes. *Phys Rev*, 80:580 – 94, 1950. , doi: 10.1103/PhysRev.80.580.

[62] Carr HY and Purcell EM. Effects of diffusion on free precession in nuclear magnetic resonance experiments. *Phys Rev*, 94:630 – 38, 1954. doi: 10.1103/PhysRev.94.630.

[63] Meiboom S and Gill D. Modified spin-echo method for measuring nuclear relaxation times. *Rev Sci Instrum*, 29:688 – 91, 1958. , doi: 10.1063/1.1716296.

[64] Zaharchuk G. Theoretical basis of hemodynamic MR imaging techniques to measure cerebral blood volume, cerebral blood flow, and permeability. *AJNR Am J Neuroradiol*, 28:1850 – 58, 2007. PubMed: 17998415, doi: 10.3174/ajnr.A0831.

[65] McGehee BE, Pollock JM, and Maldjian JA. Brain perfusion imaging: How does it work and what should I use? *J Magn Reson Imaging*, 36: 1257 – 72, 2012. PubMed: 23165731, doi: 10.1002/jmri.23645.

[66] Lu H, Law M, Johnson G, et al. Novel approach to the measurement of absolute cerebral blood volume using vascular-space-occupancy magnetic resonance imaging. *Magn Reson Med*, 54:1403 – 11, 2005. PubMed: 16254955, doi: 10.1002/mrm.20705.

[67] Buxton RB. *Introduction To Functional Magnetic Resonance Imaging*. Cambridge University Press, 1st edition, 2002.

[68] Ostergaard L. Cerebral perfusion imaging by bolus tracking. *Top Magn Reson Imaging*, 15:3 – 9, 2004. PubMed: 15057169.

[69] Ostergaard L, Weisskoff RM, Chesler DA, et al. High resolution measurement of cerebral blood flow using intravascular tracer bolus passages. Part I: Mathematical approach and statistical analysis. *Magn Reson Med*, 36:715 – 25, 1996. PubMed: 8916022, doi: 10.1002/mrm.1910360510.

[70] van Osch MJ, van der Grond J, and Bakker CJ. Partial volume effects on arterial input functions: shape and amplitude distortions and their correction. *J Magn Reson Imaging*, 22:704 – 9, 2005. PubMed: 1626157, doi: 10.1002/jmri.20455.

[71] Ellinger R, Kremser C, Schocke MF, et al. The impact of peak saturation of the arterial input function on quantitative evaluation of dynamic susceptibility ccntrast-enhanced MR studies. *J Comput Assist Tomogr*, 24:942 – 48, 2000. PubMed: 11105716.

[72] Tofts PS. Modeling tracer kinetics in dynamic Gd-DTPA MR imaging. *J Magn Reson Imaging*, 7:91 – 101, 1997. PubMed: 9039598.

[73] Patlak CS and Blasberg RG. Graphical evaluation of blood-to-brain transfer constants from multiple-time uptake data. Generalizations. *J Cereb Blood Flow Metab*, 5:584 – 90, 1985. PubMed: 4055928, doi: 10.1038/jcbfm.1985.87.

[74] Larsson HB, Courivaud F, Rostrup E, et al. Measurement of brain perfusion, blood volume, and blood-brain barrier permeability, using dynamic contrast-enhanced T(1)-weighted MRI at 3 Tesla. *Magn Reson Med*, 62:1270 – 81, 2009. PubMed: 19780145, doi: 10.1002/mrm.22136.

[75] Li KL, Buonaccorsi H, Thompson G, et al. An improved coverage and spatial resolution - using dual injection dynamic contrast-enhanced (ICE-DICE) MRI: a novel dynamic contrast-enhanced technique for cerebral tumors. *Magn Reson Med*, 68:452 – 62, 2012. PubMed: 22791559, doi: 1002/mrm.23252.

[76] Tofts PS, Brix G, Buckley DL, et al. Estimating kinetic parameters from dynamic contrast-enhanced T(1)-weighted MRI of a diffusable

tracer: standardized quantities and symbols. *J Magn Reson Imaging*, 10:223 – 32, 1999. PubMed: 10508281.

[77] Baudrexel S, Volz S, Preibisch C, et al. Rapid single-scan T2*-mapping using exponential excitation pulses and image-based correction for linear background gradients. *Magn Reson Med*, 62:263 – 68, 2009. PubMed: 19353655, doi: 10.1002/mrm.21971.

[78] Preibisch C, Volz S, Anti S, et al. Exponential excitation pulses for improved water content mapping in the presence of background gradients. *Magn Reson Med*, 60:908 – 16, 2008. PubMed: 18816811, doi: 10.1002/mrm.21730.

[79] Hirsch NM and Preibisch C. T2* mapping with background gradient correction using different excitation pulse shapes. *AJNR Am J Neuroradiol*, Epub ahead of print, 2012. PubMed: 22837312, doi: 10.3174/ajnr.A3021.

[80] Hirsch NM and Preibisch C. T2* measurement in the presence of susceptibility gradients. *Magn Reson Mater Phy*, 24(Issue 1 Supp): 609, 2011. doi: 10.1007/s10334-011-0268-5.

[81] Magerkurth J, Volz S, Wagner M, et al. Quantitative T2*-mapping based on multi-slice multiple gradient echo FLASH imaging: Retrospective correction for subject motion effects. *Magn Reson Med*, 66: 989 – 97, 2011. PubMed: 21381108, doi: 10.1002/mrm.22878.

[82] Ericsson A, Weis J, Hemmingsson A, et al. Measurements of magnetic field variations in the human brain using a 3D-FT multiple gradient echo technique. *Magn Reson Med*, 33:171 – 77, 1995. PubMed: 7707906, doi: 10.1002/mrm.1910330205.

[83] Gelman N, Gorell JM, Barker PB, et al. MR imaging of human brain at 3.0 T: preliminary report on transverse relaxation rates relation to estimated iron content. *Radiology*, 210:759 – 67, 1999. PubMed: 10207479,.

[84] Kumar R, Delshad S, Macey PM, et al. Development of T2-relaxation values in regional brain sites during adolescence. *Magn Reson Imaging*, 29:185 – 93, 2011. PubMed: 20933351, doi: 10.1016/j.mri.2010.08.006.

[85] Hennig J. Echoes - how to generate, recognize, use or avoid them in MR-imaging sequences. Part I: Fundamental and not so fundamen-

tal properties of spin echoes. *Concepts Magn Reson*, 3:125 – 43, 1991. doi: 10.1002/cmr.1820030302.

[86] Hennig J, Weigel M, and Scheffler K. Calculation of flip angles for echo trains with predefined amplitudes with the extended phase graph (EPG)-algorithm: principles and applications to hyperecho and TRAPS sequences. *Magn Reson Med*, 51:68 – 80, 2004. PubMed: 14705047, doi: 10.1002/mrm.10658.

[87] Knopp EA, Cha S, Johnson G, et al. Glial neoplasms: dynamic contrast-enhanced T2*-weighted MR imaging. *Radiology*, 211:791 – 98, 1999. PubMed: 10352608.

[88] Herscovitch P and Raichle ME. What is the correct value for the brain-blood partition coefficient for water? *J Cereb Blood Flow Metab*, 5:65 – 69, 1985. PubMed: 3871783, doi: 10.1038/jcbfm.1985.9.

[89] Zhu XP, Li KL, Kamaly-Asl ID, et al. Quantification of endothelial permeability, leakage space, and blood volume in brain tumors using combined T1 and T2* contrast-enhanced dynamic MR imaging. *J Magn Reson Imaging*, 11:575 – 85, 2000. PubMed: 10862055.

[90] Uematsu H, Maeda M, Sadato N, et al. Blood volume of gliomas determined by double-echo dynamic perfusion-weighted MR imaging: a preliminary study. *AJNR Am J Neuroradiol*, 22:1915 – 19, 2001. PubMed: 11733325.

[91] Donahue KM, Krouwer HG, Rand SD, et al. Utility of simultaneously acquired gradient-echo and spin-echo cerebral blood volume and morphology maps in brain tumor patients. *Magn Reson Med*, 43:845 – 53, 2000. PubMed: 10861879, doi: 10.1002/1522-2594(200006)43:6<845::AID-MRM10>3.0.CO;2-J.

[92] Weisskoff RM, Boxerman JL, Sorensen AG, et al. Simultaneous blood volume and permeability mapping using a single Gd-based contrast injection. *Proceedings of the Second Meeting of the Society of Magnetic Resonance, San Francisco, California*, 279, August 6-12, 1994.

[93] Law M, Yang S, Babb JS, et al. Comparison of cerebral blood volume and vascular permeability from dynamic susceptibility contrast-enhanced perfusion MR imaging with glioma grade. *AJNR Am J Neuroradiol*, 25:746 – 55, 2004. PubMed: 15140713.

[94] Boxerman JL, Prah DE, Paulson ES, et al. The role of preload and leakage correction in gadolinium-Based cerebral blood volume estimation determined by comparison with MION as a criterion standard. *AJNR Am J Neuroradiol*, 33:1081 – 87, 2012. PubMed: 22322605, doi: 10.3174/ajnr.A2934.

[95] Bjornerud A, Sorensen AG, Mouridsen K, et al. T1- and T2*-dominant extravasation correction in DSC-MRI: Part I - Theoretical considerations and implications for assessment of tumor hemodynamic properties. *J Cereb Blood Flow Metab*, 33:1081 – 87, 2012. PubMed: 21505483, doi: 10.1038/jcbfm.2011.52.

[96] Liu CY, Varadarajan P, Pohost GM, et al. Relaxivity in different tissue models at 3T. *Proc ISMRM Thirteenth Scientific Sessions, Miami, Florida*, 254, 2005.

[97] Silvennoinen MJ, Clingman CS, Golay X, et al. Comparison of the dependence of blood R2 and R2* on oxygen saturation at 1.5 and 4.7 Tesla. *Magn Reson Med*, 49:47 – 60, 2003. PubMed: 12509819, doi: 10.1002/mrm.10355.

[98] An H and Lin W. Cerebral venous and aterial blood volumes can be estimated separately in humans using magnetic resonance imaging. *Magn Reson Med*, 48:583 – 88, 2002. PubMed: 12353273, doi: 10.1002/mrm.10257.

[99] Toth V, Preibisch C, Hirsch NM, et al. MR-based hypoxia measures in human glioma: preliminary results. *J Neurooncol*, submitted, 2013.

[100] Bjornerud A and Emblem KE. A fully automated method for quantitative cerebral hemodynamic analysis using DSC-MRI. *J Cereb Blood Flow Metab*, 30:1066 – 78, 2010. PubMed: 20087370, doi: 10.1038/jcbfm.2010.4.

[101] Zhang Y, Wang J, Wang X, et al. Feasibility study of exploring a T(1)-weighted dynamic contrast-enhanced MR approach for brain perfusion imaging. *J Magn Reson Imaging*, 35:1322 – 31, 2012. PubMed: 22314848, doi: 10.1002/jmri.23570.

[102] Sourbron S, Ingrisch M, Siefert A, et al. Quantification of cerebral blood flow, cerebral blood volume, and blood-brain-barrier leakage with DCE-MRI. *Magn Reson Med*, 62:205 – 17, 2009. PubMed: 19449435, doi: 10.1002/mrm.22005.

[103] Hirsch NM, Bauer M, Kooijman H, et al. CBV quantification with DSC and VASO in areas of a disrupted blood-brain barrier. *Magn Reson Mater Phy*, 25(Issue 1 Supp):116, 2012. doi: 10.1007/s10334-012-0321-z.

[104] Preibisch C, Hirsch NM, Toth V, et al. Influence of CBV on MR based measures of hypoxia in healthy human brain and tumorous tissue. *Magn Reson Mater Phy*, 25(Issue 1 Supp):77, 2012. doi: 10.1007/s10334-012-0321-z.

[105] Hirsch NM, Preibisch C, Toth V, et al. Semi-quantitative characterization of hypoxic areas in vivo. *Magn Reson Mater Phy*, 24(Issue 1 Supp):168, 2011. doi: 10.1007/s10334-011-0266-7.

[106] Hirsch NM, Preibisch C, Toth V, et al. Characterization of hypoxic areas in the human brain. *Proc ISMRM*, 20:3180, 2012.

[107] Oros-Peusquens AM, Laurila M, Shah NJ, et al. Magnetic field dependence of the distribution of NMR relaxation times in the living human brain. *Magn Reson Mater Phy*, 21:131 – 47, 2008. PubMed: 18338191, doi: 10.1007/s10334-008-0107-5.

[108] Weiskopf N, Hutton C, Josephs O, et al. Optimized EPI for fMRI studies of the orbitofrontal cortex: compensation of susceptibility-induced gradients in the readout direction. *Magn Reson Mater Phy*, 20:39 – 49, 2007. PubMed: 17268781, doi: 10.1007/s10334-006-0067-6.

[109] Lange I, Hirsch NM, Shao J, et al. Effect of white matter fiber orientation and fractional anisotropy on T2* in human brain. *Magn Reson Mater Phy*, 25(Issue 1 Supp):88, 2012. doi: 10.1007/s10334-012-0321-z.

[110] Li TQ, van Gelderen P, Merkle H, et al. Extensive heterogeneity in white matter intensity in high-resolution T2*-weighted MRI of the human brain at 7.0 T. *NeuroImage*, 32:1032 – 40, 2006. PubMed: 16854600, doi: 10.1016/j.neuroimage.2006.05.053.

[111] Bender B and Klose U. The in vivo influence of white matter fiber orientation towards B(0) on T2* in the human brain. *NMR Biomed*, 23:1071 – 76, 2010. PubMed: 20665897, doi: 10.1002/nbm.1534.

[112] Denk C, Hernandez Torres E, MacKay A, et al. The influence of white matter fibre orientation on MR signal phase and de-

cay. *NMR Biomed*, 24:246 – 52, 2011. PubMed: 21404336, doi: 10.1002/nbm.1581.

[113] Duyn JH, van Gelderen P, Li TQ, et al. High-field MRI of brain cortical substructure based on signal phase. *Proc Natl Acad Sci USA*, 104:11796 – 801, 2007. PubMed: 17586684, doi: 10.1073/pnas.0610821104.

[114] Zhong K, Leupold J, von Elverfeldt D, et al. The molecular basis for gray and white matter contrast in phase imaging. *NeuroImage*, 40:1561 – 66, 2008. PubMed: 18353683, doi: 10.1016/j.neuroimage.2008.01.061.

[115] Chappell KE, Robson MD, Stonebridge-Foster A, et al. Magic angle effects in MR neurography. *AJNR Am J Neuroradiol*, 25:431 – 40, 2004. PubMed: 15037469.

[116] McRobbie DW, Moore EA, Graves MJ, et al. *MRI - From Picture to Proton*. Cambridge University Press, 2nd edition, 2006.

[117] Whittall KP, MacKay AL, Graeb DA, et al. In vivo measurement of T2 distributions and water contents in normal human brain. *Magn Reson Med*, 37:34 – 43, 1997. PubMed: 8978630, doi: 10.1002/mrm.1910370107.

[118] Graham SJ, Stanchev PL, and Bronskill MJ. Criteria for analysis of multicomponent tissue T2 relaxation data. *Magn Reson Med*, 35:370 – 78, 1996. PubMed: 8699949, doi: 10.1002/mrm.1910350315.

[119] Menon RS and Allen PS. Application of continuous relaxation time distributions to the fitting of data from model systems and excised tissue. *Magn Reson Med*, 20:214 – 27, 1991. PubMed: 1775048, doi: 10.1002/mrm.1910200205.

[120] Stewart WA, MacKay AL, Whittall KP, et al. Spin-spin relaxation in experimental allergic encephalomyelitis: analysis of CPMG data using a non-linear least-squares method and liinear inverse theory. *Magn Reson Med*, 29:767 – 75, 1993. PubMed: 8350719, doi: 10.1002/mrm.1910290608.

[121] MacKay AL, Whittall KP, Adler J, et al. In vivo visualization of myelin water in brain by magnetic resonance. *Magn Reson Med*, 31:673 – 77, 1994. PubMed: 8057820, doi: 10.1002/mrm.1910310614.

[122] Rosen BR, Belliveau JW, Vevea JM, et al. Perfusion imaging with NMR contrast agents. *Magn Reson Med*, 14:249 – 65, 1990. PubMed: 2345506.

[123] Stanisz GJ, Odrobina EE, Pun J, et al. T1, T2 relaxation and magnetization transfer in tissue at 3T. *Magn Reson Med*, 54:507 – 12, 2005. PubMed: 16086319, doi: 10.1002/mrm.20605.

[124] Preibisch C and Deichmann R. T1 mapping using spoiled FLASH-EPI hybrid sequences and varying flip angles. *Magn Reson Med*, 62: 240 – 46, 2009. PubMed: 19319894, doi: 10.1002/mrm.21969.

[125] Blockley NP, Jiang L, Gardener AG, et al. Field strength dependence of R1 and R2* relaxivities of human whole blood to ProHance, Vasovist, and deoxyhemoglobin. *Magn Reson Med*, 60:1313 – 20, 2008. PubMed: 19030165, doi: 10.1002/mrm.21792.

[126] Hua J, Qin Q, Pekar JJ, et al. Measurement of absolute arterial cerebral blood volume in human brain without using a contrast agent. *NMR Biomed*, 24:1313 – 25, 2011. PubMed: 21608057, doi: 10.1002/nbm.1693.

[127] Petersen ET, Lim T, and Golay X. Model-free arterial spin labeling quantification approach for perfusion MRI. *Magn Reson Med*, 55:219 – 32, 2006. PubMed: 16416430, doi: 10.1002/mrm.20784.

[128] An H and Lin W. Impact of intravascular signal on quantitative measures of cerebral oxygen extraction and blood volume under normo- and hypercapnic conditions using an asymmetric spin echo approach. *Magn Reson Med*, 50:708 – 16, 2003. PubMed: 14523956, doi: 10.1002/mrm.10576.

[129] Christen T, Schmiedeskamp H, Straka M, et al. Measuring brain oxygenation in humans using a multiparametric quantitative blood oxygenation level dependent MRI approach. *Magn Reson Med*, 68: 905 – 11, 2011. PubMed: 22162074, doi: 10.1002/mrm.23283.

[130] Bolar DS, Rosen BR, Sorensen AG, et al. Quantitative Imaging of eXtraction of Oxygen and TIssue Consumption (QUIXOTIC) using venular-targeted velocity-selective spin labeling. *Magn Reson Med*, 66:1550 – 62, 2011. PubMed: 21674615, doi: 10.1002/mrm.22946.

[131] Lauwers F, Cassot F, Lauwers-Cances V, et al. Morphometry of the human cerebral cortex microcirculation: general characteristics

and space-related profiles. *NeuroImage*, 39:936 – 48, 2008. PubMed: 17997329, doi: 10.1016/j.neuroimage.2007.09.024.

[132] Lee ST and Scott AM. Hypoxia positron emission tomography imaging with 18F-fluoromisonidazole. *Semin Nucl Med*, 37:451 – 61, 2007. PubMed: 17920352, doi: 10.1053/j.semnuclmed.2007.07.001.

[133] Cher LM, Murone C, Lawrentschuk N, et al. Correlation of hypoxic cell fraction and angiogenesis with glucose metabolic rate in gliomas using 18F-fluoromisonidazole, 18F-FDG PET, and immunohistochemical studies. *J Nucl Med*, 47:410 – 18, 2006. PubMed: 16513609.

[134] Haacke EM, Brown RW, Thompson MR, et al. *Magnetic Resonance Imaging: Physical Principles and Sequence Design*. John Wiley & Sons Ltd, 1st edition, 1999.

[135] Liboff RL. *Introductory Quantum Mechanics*. Addison Wesley, 4th edition, 2002.

Software References

[136] The MathWorks, Inc. MATLAB R2009b - The Language of Technical Computing. http://www.mathworks.de/products/matlab/, Natick, MA, USA, 2009.

[137] Wellcome Trust Centre for Neuroimaging. SPM8 - Statistical Parametric Mapping. http://www.fil.ion.ucl.ac.uk/spm/software/spm8/, London, United Kingdom, 2008.

[138] Digital Image Solutions. stroketool 2.8. http://www.digitalimagesolutions.de/, Frechen, Germany, 2011.

[139] Max-Planck-Institute for Neurological Research and Faculty of Medicine of the University of Cologne. VINCI 3.8 - Volume Imaging in Neurological Research, Co-Registration and ROIs included. http://www.nf.mpg.de/vinci/AboutVinci.html, Cologne, Germany, 2011.

[140] BRAINLAB. iPlan Cranial 3.0. http://www.brainlab.com/product/item/cranial-planning-software, Feldkirchen, Germany, 2013.

[141] BRAINLAB. VarioGuide. http://www.brainlab.com/product/item/cranial-navigation-application, Feldkirchen, Germany, 2013.

Acknowledgments

There are several people I would like to thank for supporting me over the last two and a half years: The first one is Professor Dr. Axel Haase, for supervising and evaluating this work, and for helpful and valuable discussions. I also want to thank Professor Dr. Claus Zimmer, for making the Department of Neuroradiology such a pleasant location for pursuing my research, and for giving me the possibility to attend quite a few very interesting international conferences. I am also grateful to both of them for their support in my scholarship applications.

A warm thank you to Dr. Christine Preibisch, for teaching me so much about magnetic resonance imaging, for patiently answering my numerous questions, and for the in every respect great collaboration during the past years.

Thanks to Professor Dr. Ralf Deichmann from the Brain Imaging Center in Frankfurt, for providing code templates for the $T2^*$ corrections which I could put to good use in our data evaluation batches, and to Dr. Hendrik Kooijman from Philips Healthcare, for helping me with the Achieva scanner simulator. Thanks to Dr. Carl Ganter and Dr. Isabel Dregely for their help with the Siemens IDEA simulating platform, when I was totally stuck.

I also want to thank Vivien Tóth for acquiring the patients and for her contributions to the data evaluations of the tumor patients. Thanks to Monika Ankenbrank for her contribution to the evaluation of the stroke patients data, and to Isabel Lange for doing the calculations with $T2^*$ and white matter structure. Thanks to the medical technical assistants Josette Höhn, Siri Schmidt and Maria Becker, for their readiness to competently perform all patients measurements, and not to forget, to Dr. Annette Förschler, for her unhesitating and very qualified help in all kinds of issues.

Finally I would like to thank the Deutsche Telekom Stiftung, the Universität Bayern e.V. and the Graduate School of Information Science in Health for providing personal and financial support and thus enabling me to fully concentrate on my project.

Thank you all very much!